TECHNISCHE UNIVERSITÄT MÜNCHEN

Walter Schottky Institut

Zentralinstitut für physikalische Grundlagen der Halbleiterelektronik

Nanoparticle Structures for Plasmonic Applications

Vera Zon

Vollständiger Abdruck der von der Fakultät für Physik der Technischen Universität München zur Erlangung des akademischen Grades eines

Doktors der Naturwissenschaften (Dr. rer. nat.)

genehmigten Dissertation.

Vorsitzender: Univ.-Prof. Dr. J. Leo van Hemmen

Prüfer der Dissertation: 1. Univ.-Prof. Dr. Gerhard Abstreiter

2. Univ.-Prof. Dr. Friedrich C. Simmel

Abstract

In this thesis I will introduce our new approaches to create predetermined metallic nanostructures for future studies of plasmonic interactions between single-particles. Colloids of noble metals possess unique optical properties that can be used for sensing, opto-electronics, surface-enhanced Raman scattering, fluorescence, and IR absorbance spectroscopy. These optical properties are governed by localized surface plasmon resonances, which can be studied by building structures with tailored optical properties (optical circuits) from individual inorganic particles. In this thesis we have chosen to examine two metals that are highly interesting due to their chemical and physical properties. Here, because of its chemical stability, we use gold nanoparticles as a model system to examine new ways to achieve specific functionality. However, since gold possesses poor physical properties for plasmonic applications, we investigate new ways to create silver nanoparticle systems, which is the best-performing choice among metals for optical frequencies. Working to further this topic, we find a new way to grow silver nanoparticles in the presence of DNA under physiological conditions in a one-pot reaction by means of a photo-induced reaction where the DNA is left intact. Furthermore, by applying new protocols for controlled formation of nanoparticle dimers, DNA-streptavidin conjugates, and DNA functionalized nanoparticles we show that purified fractions of DNA-functionalized nanoparticle dimers and monomers can, by exploiting Watson-Crick base pairing of DNA, be used to create larger nanostructures. Such assemblies would be very interesting to use while investigating plasmon-transport and plasmon-enhanced phenomena in solution ensembles and at a single particle level.

Contents

1

Introduction

In this chapter I will introduce our new approaches to create predetermined metallic nanostructures for future studies of plasmonic interactions between single-particles. Here, Section 1.1 provides a literature review, summarizing the relevant scientific findings up to the original questions that this work is based on. This is followed, in Section 1.2, by the scope, where a short overview of how these questions are addressed is presented together with the corresponding publications to which I made a significant contribution. Furthermore, a short summary will be given directing the reader to where in this thesis each topic is discussed in more detail and in Chapter 7 these questions are repeated followed by a summary of our findings, conclusions and outlook.

1.1 Literature Review

Colloids of noble metals possess unique properties in diverse areas such as catalysis, sensing, (opto-) electronics, surface-enhanced Raman scattering, fluorescence, IR absorbance spectroscopy, and biomedical applications.[1–4] The optical properties of metal nanoparticles are governed by localized surface plasmon resonances, which result from the interaction of a particles conduction electrons with incident light.[5,6] In order to construct complex architectures with tailored optical properties (optical circuits) from individual inorganic particles,[7] two assembly approaches hold particular promise: lithographic predesign[8–12] and deterministic arrangement on the nano-scale by biomolecular interactions.[13–22] There are several reasons why the biomolecular approach is widely used:[19,23]

1. Their diversity provides a wide choice of size and functionality.

2. Well-developed methods to synthesize and modify them enable their application in combination with different inorganic materials.

3. Their inherent repair and catalytic mechanisms can provide structures with a specific functionality and even allow them to be tuned after construction.

Here, two routes can be considered for the preparation of particle-bioconjugates as building blocks for biomolecule-templated nanostructures: either conjugation of the pre-formed colloids with biomolecules through suitable functionalization chemistry[23–29] or direct growth of metal particles, wires or mashes on native or predesigned DNA strands.[30–48] An advantage of the first approach is the established surface chemistry and purification procedures,[49,50] while the second has its advantage in that controlled growth or mediation by DNA scaffolds is very selective and usually does not require cumbersome separation procedures.

While there are numerous methods to nucleate and grow silver particles directly on DNA molecules, which include the modification of DNA with aldehyde moieties[48] (Tollens

reaction),[34,51] introduction of strong reducing agents,[33] and illumination with UV light,[52] these methods irreversibly damage the DNA strands. Furthermore, other known chemistry like the photo-induced reduction of silver ions to promote particle nucleation from silver salts, which use hard UV irradiation in presence of organic solvents,[53–56] deaerated aqueous media in presence of sodium dodecyl sulfate,[57] or an organic dye and tri-ethanolamine as an electron donor,[58] also lead to the degradation or insolubility of DNA during the reaction. Here, a potentially nondestructive method is based on the detection of dye-labeled DNA[59] through spectrally sensitized photography,[60] which involves the photo-induced reduction of silver ions by optically excited dye molecules.[58,61] However, *if silver nanoparticles can be grown in presence of DNA under physiological conditions in a one-pot reaction by means of a photo-induced reaction where the DNA is left intact, has not been investigated.*

In addition to templated growth of nanoparticles, DNA is a popular candidate for deterministic assembly of inorganic nanoparticles through its unique inherent self-organization properties (also known as Watson-Crick base-pairing).[27] There are various established techniques to modify DNA with thiol-linkers,[62] so that the strand can be immobilized onto metallic nanoparticles though chemisorption of the thiol-group,[24,25,63,64] which was originally developed for planar metal surfaces and then adapted for nano-technological applications.[50] However, existing protocols require a high ratio of thiol-modified DNA molecules to nanoparticles due to the reduced binding strength between mono- or di-sulfhydryl groups and the particle surface.[24,25,63] However, except for planar gold surfaces,[65] DNA modified with four sulfhydryl groups, such as di-thiol-phosphor-amidite (DTPA), has not been used to functionalize nanoparticles. So, *whether a higher number of thiol-groups in a linker molecule would be advantageous when functionalizing nanoparticles with DNA, is not known.*

For applications such as fluorescence resonance energy transfer, plasmon coupling and assembly of nano-electronic devices,[66,67] it is advantageous to use particles with a predefined number of attached DNA strands where, due to plasmon coupling efficiency, each strand length is comparable to the diameter of the particle.[5] Here, the reproducibility of a structures design is directly dependent on the purity of a desired conjugate and even

though advances have been made in synthesis,[50,68] successful separation and isolation continues to be a challenge. For example, a commonly used separation technique, like agarose gel electrophoresis, is proven difficult due to the necessity to adjust for particle size, the use of DNA strands that are too long for efficient plasmon coupling, and elution problems from the gel matrix.[49,63,69–71] However, the use of anion-exchange high pressure liquid chromatography has been put forward, which has the potential to overcome these problems.[72] Nevertheless, the authors confirmed that their work was 'proof of concept' and for this method to give high enough yield and reproducibility to be a useful, additional work is required. Thus, *if anion-exchange high pressure liquid chromatography can be a viable alternative and improvement for existing techniques to reproducibly obtain high yields of nanoparticles with a predefined number of short DNA strands attached, has yet to be demonstrated.*

Even though DNA is an excellent scaffold and linker to organize nanoparticles on the nano-scale,[13,14,73] combining it with other biomolecules, such as proteins or peptides, can be particularly beneficial due to the reversible self-recognizing nature of their geometrically defined binding.[22,23,74–78] Streptavidin, a homotetrameric protein with dihedral D2 symmetry, is widely used as a central building block as it forms multiple angularly defined attachment sites to biotin, has an extraordinarily strong affinity constant (exceeding 10^{14} M^{-1}) and high thermal and chemical stability.[79–85] Here, nanoparticles functionalized with thiol-modified DNA strands used in combination with streptavidin bound to specific numbers of the complementary biotin-functionalized DNA strands,[86] or alternatively by means of nanoparticles functionalized with thiol-biotin mixed with streptavidin bound to biotin-functionalized DNA in combination with a similar mixture containing the complementary DNA strand,[74,75] have been used to form nano-scale architectures for potential electronic purposes.[87,88] However, *using nanoparticles functionalized with thiol-biotin-streptavidin bound to specific numbers biotin-functionalized DNA strands has not been reported. Furthermore, the conformation that bound streptavidin with and without DNA has to a nanoparticle is not understood.*

Multiple-site binding proteins such as avidin and streptavidin are promising particle linkers since they act as a strong aggregating agent for biotin-functionalized inorganic nanoparticles[89–100] and have additionally been used to study plasmonic effects.[101,102] Here, focus has been placed on the kinetics of uncontrolled formation of predominantly large unstable particle aggregates,[89–91] where a model of the aggregation process has been developed which accounts for the influence of stoichiometry as well as role of the ligand geometry.[103,104] Investigations have also been made into separation, purification and characterization of molecularly bridged nanoparticles[105–107] which include unsuccessful attempts at size exclusion chromatography.[107,108] So, *whether it is possible to obtain a high enough control over the interlinking process of biotin-functionalized particles and streptavidin, to obtain high yields of small particle complexes and additionally enrich them under physiological conditions through size exclusion chromatography, has not been reported.* While these studies focus on aggregating biotin functionalized particles with low concentrations of streptavidin, *there are no comments on if high concentrations can hinder aggregation through saturation of the binding sites.* Furthermore, *there have been no attempts to organize particles on the nano-scale by combining DNA functionalized streptavidin-induced nanoparticle-dimers into complex structures.*

1.2 Scope of This Work

In this thesis we have chosen to examine two metals that are highly interesting due to their chemical and physical properties. Here, because of its chemical stability, we use gold nanoparticles as a model system to examine new ways to achieve specific functionality. However, since gold possesses poor physical properties for plasmonic applications, we investigate new ways to create silver nanoparticle systems, which is the best-performing choice among metals for optical frequencies.

There exist many established routes to obtain gold particles conjugated with DNA molecules. From these numerous reports we chose the well-studied functionalization of gold nanoparticles with thiol-modified DNA molecules as a model system to learn the necessary chemistry and methods involved in synthesizing and separating different types of conjugates. While the functionalization protocols were successfully reproduced, we investigate using a new thiol-based linker molecule DTPA to provide higher stability through the four (instead of one or two) thiol groups used for chemisorption onto particle surfaces, and a new protocol adaptation to increase colloidal stability by using mPEG-thiol instead of BSPP as a final capping agent.[109]

There are a number of reported protocols to separate inorganic nanoparticles by the number of attached DNA strands, including anion-exchange high pressure liquid chromatography. However, the separation procedures result in low yield and in the latter case in poor reproducibility due to the damage caused by the nanoparticles to the analytical column. We note that the authors confirmed the problems associated with high pressure liquid chromatography separation. Here, based on the previously discussed functionalization protocol of the 20 nm gold nanoparticles with DNA-DTPA, we create a new protocol to gain reproducible high yield separation of nanoparticles by the number of DNA strands attached to their surfaces with anion-exchange high pressure liquid chromatography.[109]

An alternative way of achieving DNA terminated nanoparticles, which is potentially better for defined structures, is to use a central building block with multiple angularly defined

attachment sites. Since it is well documented, we used the protein streptavidin, which binds reversibly to four biotin molecules. Here, we take a novel approach and isolate the four different conjugates of DNA_{1-4}-biotin-streptavidin with high pressure liquid chromatography to create DNA-nanoparticle conjugates. To this end, we prepared biotin functionalized nanoparticles by using the new high pressure liquid chromatography compatible thiol-chemistry to attach biotin-PEG-disufides to the nanoparticle surfaces. To conjugate biotin-nanoparticles with DNA-biotin-streptavidin the two protocols were combined in a more direct, but in itself novel, way by mixing the four equally distributed DNA-biotin-streptavidin complexes together with the biotin-nanoparticles, instead of the more controlled variant of introducing the purified fractions that will be discussed in a later chapter. In this intermediate step, we examine if the new biotin-nanoparticle and streptavidin-DNA protocols work and more importantly, that they work well together before proceeding with more advanced structures. Moreover, we make an original investigation into the conformation of bound streptavidin and streptavidin-DNA to gold nanoparticle surfaces.[110–114]

Using the new biotin-functionalized gold nanoparticles, we investigate a controlled assembly approach with streptavidin as the interlinking agent. Here, we make a new analysis on the aggregation process, in dependence on streptavidin concentration and ionic strength of the solution, to obtain small stable biotin active or streptavidin saturated particle complexes. We also provide an insight into the kinetics of the process, influence of ζ-potential on the aggregation and size analysis of the obtained complexes, derived with dynamic light scattering and transmission electron microscopy techniques. Additionally, we present new results from size exclusion chromatography that was used to enrich fractions containing species made up from a specific number of interlinked particles. Furthermore, in combining the previously describes topics we investigate a new way to obtain high order structures by combining DNA functionalized streptavidin-induced nanoparticle-dimers into larger nano-structures that are ready to be used for further studies of plasmonic phenomena.[110–114]

Lastly, we used our collected know-how to develop a new protocol for photo-induced nucleation and growth of silver nanoparticles in aqueous solution in the presence of DNA oligomers. Here, we develop a novel one-pot reaction protocol based on silver nitrate and tri-sodium citrate in biologically friendly conditions allowing the nucleation and growth of silver nanoparticles in direct proximity to DNA molecules without damaging them. Since these conditions are not beneficial for nucleation, an organic dye (Cy5) was used as a photosensitizer to initiate the nanoparticle growth upon illumination with 647 nm light. Moreover, we investigate the catalytic effect of silver ions on the photo-bleaching of the Cy5 dye that is attached to the DNA strand. We also characterize the grown silver particles in terms of size and their association with the DNA molecules and discuss the potential for direct organization into predesigned two- or three-dimensional structures for further applications in plasmonic studies.[115–117]

Overview

The results of the investigation into:

- Whether a higher number of thiol-groups in a linker molecule would be advantageous when functionalizing nanoparticles with DNA, is shown in Chapter 4.

- If anion-exchange high pressure liquid chromatography can be a viable alternative and improvement for existing techniques to reproducibly obtain high yields of nanoparticles with a predefined number of short DNA strands attached, is demonstrated in Chapter 4.

- Using nanoparticles, functionalized with thiol-biotin with streptavidin bound to specific numbers biotin-functionalized DNA strands, is discussed in Chapter 4.

- The conformation that bound streptavidin with and without DNA has to nanoparticle surfaces, is presented in Chapter 4.

- Whether it is possible to obtain a high enough control over the interlinking process of biotin-functionalized particles and streptavidin, to obtain high yields of small particle complexes and additionally enrich them under physiological conditions through size exclusion chromatography, is investigated in Chapter 5.

- If high concentrations can hinder aggregation through saturation of the binding sites is presented in Chapter 5.

- The nano-scale organization of particles by combining DNA functionalized streptavidin-induced nanoparticle-dimers into complex structures, is studied in Chapter 5.

- If silver nanoparticles can be grown in presence of DNA under physiological conditions in a one-pot reaction by means of a photo-induced reaction where the DNA is left intact, is investigated Chapter 6.

2

Material and Methods

This chapter provides insight into the working principles of the different experimental techniques and the specifications of the materials that have been used for this thesis.

2.1 Methods

In this section UV – visible spectrophotometry, dynamic light scattering, transmission electron microscopy, and high pressure liquid chromatography are discussed.

Ultraviolet – Visible Spectrophotometry

Ultraviolet – visible spectrophotometry is an analytical and biochemical technique that was employed to determine the presence and concentration of analytes and to characterize them. The set-up consisted of:

- A commercial spectrophotometer (Cary 50, Varian, Inc.)

- 10 mm quartz cuvette, 110-QS, Hellma, or 10 mm UV-transparent plastic cuvette, Brand GmbH & Co. KG, respectively)

In this system a Xenon Flash Lamp is used as a light source, which reduces degradation of photosensitive samples as the lamp only flashes when acquiring a data point. The beam is then diffracted on a grating which is configured to obtain a spectral resolution of 0.5 nm through a wavelength range of 190–1100 nm at a maximum scan rate of 400 nm per second. The diffracted light is then passed through a beam-splitter, where the intensity, I_0, of the split off light is measured with a reference detector. The other portion is transmitted through the sample and its intensity, I, measured with a second detector giving the transmittance I/I_0. Here, if the sample molecules contain π- or non-bonding electrons, they can be excited across the energy gap between the highest occupied molecular orbital (HOMO) to the lowest unoccupied molecular orbital (LUMO). So, if the energy between HOMO and LUMO is approximately equal the photon energy photoelectric excitation causes less light to be transmitted through the sample. However, in this thesis we study mostly ensembles of metal colloids where the high amount of light scattering makes it more intuitive to use the samples extinction,[5,6] which is defined as the difference between the incident and transmitted light intensities normalized to the intensity of the incident light or $1 - I/I_0$.

Photon Correlation Spectroscopy

Photon correlation spectroscopy, also known as dynamic light scattering, is an analytical technique that was employed to determine the size of colloidal species. The set-up consisted of:

- A commercial photon correlation spectrometer (Zetasizer Nano ZEN3600, Malvern Instruments)

- 10 mm quartz cuvette, 110-QS, Hellma, or 10 mm UV-transparent plastic cuvette, Brand GmbH & Co. KG, respectively)

- Disposable capillary cell for ζ-potential measurements (DTS1061, Malvern)

In this system attenuated laser light, scattered from a sample at 173°, is measured over time. Here, when monochromatic, coherent light hits particles that are smaller than the wavelength, time-dependent fluctuation in the intensity produced by Rayleigh scattering, is observed due to that the particles Brownian motion causes either constructive or destructive interference of the scattered light by the surrounding particles. The rate, at which these intensity fluctuations occur, will depend on the time scale of movement of the scattering species and therein the size of the particles. As stationary particles would give a constant signal, the instrument measures the deviations from that line over the time taken to reach a preset deviation value. Where the sampling speed is typically between nano- and micro-seconds, and the amplitude of the oscillation can be tuned by attenuating the incoming laser light. Since the shape of this correlation function, where a single or multiple exponential fit will represent a mono- or poly-dispersed colloid respectively,[118] this measurement needs to be performed several times to form a satisfactory dataset. The hydrodynamic diameter d_h can be found through the correlation function, G, in dependence on the correlator time delay, τ, and can be written as

$$G(\tau) = A\left[1 + Be^{-\frac{kT}{3\pi\eta d_h}\left[\frac{4\pi n}{\lambda}\sin\left(\frac{\theta}{2}\right)\right]^2 \tau}\right],$$

where A is the baseline, B is the intercept, k is the Boltzmann constant, T is the absolute temperature, η is the viscosity, n the refractive index of the dispersant, λ is the wavelength of the laser and θ is the scattering angle. Here, the exponent without correlator time delay is the Doppler shift, which reaches maximum in back-scattering. The obtained size distribution is a plot of the relative intensity of light scattered by particles in various size classes and is therefore known as an intensity size distribution. If the plot shows a substantial tail, or more than one peak, then Mie theory can make use of the input parameter of the samples refractive index to convert the intensity distribution to a volume distribution. This will then give a more realistic view of the importance of a tail or second peak as larger particles will influence the distribution by intensity six orders of magnitude more than the distribution by number.

The technique can also be used to determine ζ-potential of colloidal particles, which is used to characterize stability of the suspension against aggregation. Here, an electric potential is applied to the solution and laser Doppler electrophoresis is employed to determine the electrophoretic mobility of the colloidal particles, which is directly proportional to their ζ-potential through the Henry equation. The mobility is defined through the frequency shift of the scattered light in comparison to the incident. Analysis of the frequency and corresponding phase shift either by applying Fourier transform or phase analysis light scattering provides the value of ζ-potential for the studied colloidal species.

Transmission Electron Microscopy

Transmission electron microscopy is an imaging technique that that can resolve objects down to atomic fringes,[119] and was employed to examine single nanoparticles. The set-up consisted of:

- A commercial transmission electron microscope (JEOL 100 CX or CM100, Philips)

- Carbon-coated 300-mesh copper grid (Plano), which were made hydrophilic prior to deposition by a 10 second exposure to oxygen plasma (Technics Plasma 100-E, operated at 50 W with an oxygen pressure of 1.4 mbar)

In this system electrons are generated by thermionic emission of a tungsten filament, accelerated to 100 keV by an electric potential, formed into a beam by using a Wehnelt cylinder, and focused by electrostatic and electromagnetic lenses, which usually consist of condenser lenses for the primary beam, objective lenses to focus the beam on the specimen and projector lenses to image the transmitted electrons on a fluorescent screen. Here, the interaction of the beam with the sample will scatter the electrons while they are being transmitted through it and this defines the image obtained on the fluorescent screen. The atomic number of the scattering species determines the contrast of the picture, for example, the greater the number the stronger the electron scattering, the better the image contrast. Therefore, metallic particles can be better visualized in comparison to organic compounds. Furthermore, by bringing the back focal plane onto the screen, the scattering pattern from the sample can be collected, which contains information about its crystallographic structure.

High Pressure Liquid Chromatography

High pressure liquid chromatography is an analytical and biochemical technique that was employed to separate, purify and analyze compounds of interest.[120,121] The set-up consisted of:

- A commercial high pressure liquid chromatography system (Agilent 1200 series, Agilent Technologies)

- An in-line degasser (Agilent 1200 series, Agilent Technologies)

- A manual injector (Agilent 1200 series, Agilent Technologies)

- A multi-wavelength UV-Vis detector (Agilent 1200 series, Agilent Technologies)

- A manual fraction collector (Agilent 1200 series, Agilent Technologies)

- A size exclusion analytical column (Tosoh TSK-GEL G5000PWxl, Tosoh Biosciences)

- Anion-exchange analytical column with a stationary phase of superficially porous particles (DNAPac Pa-100, Dionex)

- Anion-exchange analytical column with a stationary phase of porous particles (YMC-BioPro QA, YMC Europe)

In this system, up to four solvents are passed through a vacuum degasser and a high-speed proportioning valve provides gradient generation by low pressure mixing before entering the dual plunger pump assembly. The pump generates the flow of the mobile phase that passes the injector assembly where the sample is introduced and is pressurized against the analytical column where separation takes place. A UV-vis detector is placed at the exit of the column that identifies, qualitatively and quantitatively, the separated species so that different fractions of the analyte can be separately collected.[122] Here, the separation principle is based on the interaction of the sample with the packaging material of the column, where the high pressure allows for increasing the specific interaction and involves mostly physical and not (bio-) chemical interactions. In this work two types of columns were used, size exclusion and anion-exchange:

- Size exclusion chromatography is designed for separation of macromolecules through mechanical interaction with the stationary phase of the column, which is typically filled with porous particles. Here, larger species pass around the porous particles and elute sooner, while smaller species are retained for longer inside, increasing their retention time.

- Ion exchange chromatography is based on the electrostatic interaction of species with a charged stationary phase. Here, the fractions bind with the stationary phase and the mobile phase composition needs to be changed to elute them. In this work,

an increasing gradient of NaCl was used to decrease the ion interaction giving longer retention times to species with more charge.

Additional Equipment

Additional equipment includes:

- A sample stirring unit able to keep a constant temperature (Thermomixer Comfort)

- Two centrifuges (MiniSpin Plus and a 5702 R, Eppendorf)

- pH meter (Metrohm 827 pH lab meter, Metrohm)

2.2 Materials

Chemicals

Silver nitrate, sodium nitrate, tri-sodium citrate, monosodium phosphate, disodium phosphate, sodium hydroxide, water (W4502), ACS grade water, bis(p-sulfonatophenyl)phenylphosphine dehydrate di-potassium salt (BSPP), (O-(2-Mercaptoethyl)-O′-methyl-hexa(ethylene glycol) (mPEG thiol) (**Figure 1a**), streptavidin were purchased from Sigma Aldrich. Aqueous solutions of 20 nm silver and gold nanoparticles were obtained from British Biocell International, UK. Polyoxyethylene (20) sorbitan monolaurate (Tween 20), hydrochloric acid, sodium chloride and tris(hydroxymethyl)-aminomethane were purchased from Roth GmbH, Germany. Biotin-octa(ethylene glycol) disulfide (S-PEG-biotin) (**Figure 1b**) was obtained from PolyPure, Norway, ACS grade water was used to disperse S-PEG-biotin. Lyophilized streptavidin was purchased from Rockland, USA. DNA non-self-complementary oligonucleotides were purchased from IBA GmbH, Germany and their list and corresponding annotations through the document are summarized in the following (**Figure 1c-d**):

- Cy5-DNA48 is Cy5 (NHS linked) (5')ATC AGC GTT CGA TGC TTC CGA CTA ATC AGC CAT ATC AGC TTA CGA CTA(3') with its complementary non-modified strand

- DNA-DTPA is $2 \times$ DTPA(di-thiol-phosphor-amidite) (5')ATC AGC GTT CGA TGC TTC CGA CTA ATC AGC CAT ATC AGC TTA CGA CTA(3')

- DNA-biotin is biotin (5')TAG TCG GAA GCA TCG AAG GCT GAT(3')

- DNA-biotin is biotin (5')ATC AGC GTT CGA TGC TTC CGA CTA ATC AGC CAT ATC AGC TTA CGA CTA(3')

- DNA-biotin is biotin (5')TT TTT TTT TTT TTT TTT TTT TTT TTT TTT TTT TTT TTT TTT TTT TTT TTT TAG TCG GAA GCA TCG AAG GCT GAT(5)

- DNA-biotin is biotin (5')TT TTT TTT TTT TTT TTT TTT TTT TTT TTT TTT TTT TTT TTT TTT TTT TTT ATC AGC CTT CGA TGC TTC GGA CTA(3')

All buffer solutions were prepared in Millipore water, pH value was adjusted to the desired with either hydrochloric acid or sodium hydroxide while monitored with a Metrohm 827 pH lab meter and afterwards filtered with 200 nm syringe or enzymatic filter.
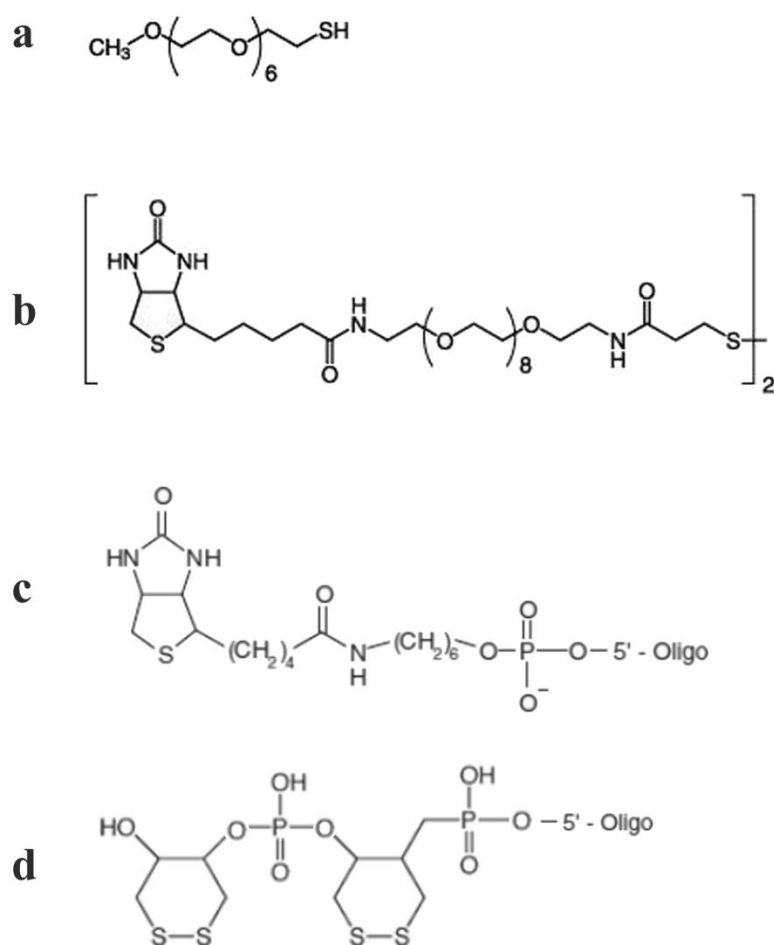

Figure 1 | Chemical Structures | (a) (O-(2-Mercaptoethyl)-O′-methyl-hexa(ethylene glycol) (mPEG thiol), (b) Biotin-octa(ethylene glycol) disulfide (S-PEG-biotin), (c) Biotin coupled to 5' DNA end, and (d) di-thiol-phosphor-amidite (DTPA) coupled to 5' DNA end.

3

Fundamentals

In this chapter, we give a background introduction to many of the concepts used in this thesis, which includes an overview of the optical and colloidal properties of the metallic nanoparticles.

3.1   Optical Properties of Metal Particles

Plasmonics is a branch of physics that has developed extensively in recent years. The field appeared as laser and surface physics crossed paths. It is considered to be one of the fastest developing areas for nanotechnology, opto-electronics, new types of microscopies and sensing. There are two major subfields of plasmonics: (1) surface plasmon polaritons which are essentially surface electromagnetic waves that are supported on a conductive surface and (2) localized surface plasmons which exist on metal nanoparticles and voids. While the first area has a large potential for discovery and testing of physical phenomena, the second has more practical applications and utilizes knowledge from colloidal chemistry, while providing a chance to test new applications and examine the optical properties of metallic nanoparticles organized in complex structures in presence of biomolecules. In this section, an overview of the optical properties of metal nanoparticles is summarized.

Optical Properties of Metals

Optical properties of metal nanoparticles are governed by their geometrical and material characteristics. Here, dielectric permittivity will largely determine the behavior of a particles interaction with light, which can be described with the Drude model, where metal electrons are considered as a free-electron gas. We note, that this model is not always fully valid when considering higher photon energies because of its inability to incorporate inter-band transitions. These transitions influence the optical properties of metals significantly when the frequency of incoming light approaches that of the metals plasma frequency, ω_p, which is when it also becomes transparent.

Localized Surface Plasmons

Surface electromagnetic waves that exist on flat metal surfaces are known as surface plasmon polaritons.[123] These waves exponentially decay in both directions away from the interface and while they propagate along it, conversion into photons takes place at its irregularities. In addition to the propagating surface plasmon polaritons on the metal-

dielectric interface, the plasmonic excitations that are bound to specific geometries are known as localized surface plasmons. These excitations are similar to the regular volume plasmons, which are oscillations of the electron gas next to a positive ionic backbone. The oscillation frequency can be determined by solving the Laplace equation (electrostatic approximation) with the appropriate boundary conditions at the spherical particle's surface. Here, the wavelength of the incoming light is considered to be significantly larger than the characteristic size of the interacting spherical particle and therefore the electric field inside a particle can be considered as homogeneous.[124] Namely, the solution for the frequencies can be written as

$$\omega_\ell = \omega_p \sqrt{\frac{\ell}{2\ell + 1}}, \qquad \ell = 1, 2, 3, \dots \tag{1}$$

For small spherical particles, the dominant role is played by the dipolar excitation with $\ell = 1$, as the size of a spherical particle increases the higher order excitations start contributing significantly to the localized surface plasmon frequency. In the limit $\ell \to \infty$ for a very large sphere the localized surface plasmon frequency defined in Eq. (1) approaches the surface plasmon frequency that is at the metal dielectric interface $\omega_{SP} = \omega_p/\sqrt{2}$. It should be noted that the localized surface plasmon frequencies are determined through the metal plasma frequency and therefore the excitations can only exist in the range where the dielectric function of the material is negative. Furthermore, the localized surface plasmons are non-propagating geometrically bound and confined to the curved surface, which can be a metallic nanoparticle or a roughness on a smooth surface, and therefore result in strong electromagnetic field enhancement. Finally, the excitations are characterized by discrete frequencies and are strongly dependent on the shape and size of the object that they are confined to. Moreover, they can be resonantly excited by incident light of appropriate frequency irrespectively of its wave-vector in contrast to the propagating surface plasmon polaritons.[124]

Although solution of the Laplace equation provides a nice overview and explanation of the fundamental physical properties that are attributed to the metal nanoparticles, the exact solution of Maxwell's equations for a homogeneous spherical particle of arbitrary size and dielectric permittivity has been obtained in terms of the Mie theory.[125] The scattering and absorption cross-sections obtained for the spherical metallic nanoparticles of different sizes in terms of the theory brilliantly correlate with the experimentally recorded data. Moreover, the Mie theory has found further development for a multiple core shell spherical particle that is well supported by the experimental data.[5] While the Mie theory itself describes the interaction of a single spherical particle with the incoming light, the developed generalized Mie theory is capable of predicting optical properties from the spherical particles organized in clusters.[5,126–128] The latter is an exact solution of the Maxwell equations with the appropriate boundary conditions.[126] Furthermore, there also exists another approach of how to describe the interaction of light with clusters built from metal nanoparticles, which employs ideas from molecular physics and considers the interaction of plasmonic excitations as a hybridization process.[129,130] Both approaches that describe nanoparticle clusters predict that; due to the plasmon interaction of the neighboring nano-spheres, if the aggregates that exist in ensemble are identical, lead to the splitting of the original plasmon peak: one of the peaks will be significantly shifted to lower energies in comparison to the original localized surface plasmon peak. However, it is important to emphasize that if an ensemble of nanoparticle clusters is inhomogeneous, the complex topologies of the clusters always smear out characteristic spectral features, while increasing the total extinction in the red region relative to the single particle peak, which makes it problematic to assign recorded optical characteristics to a specific type of a cluster.[5]

3.2 Colloidal Properties of Metal Nanoparticles

There are many ways to reliably produce metallic nanoparticles and therein investigate the unique optical properties described in Section 3.1. A well-established route it through surface and colloidal chemistry, which can be employed to produce metallic particles of different sizes and shapes from different components that include pure metals, alloys and layered structures. However, methods to create a stable mono-dispersed colloidal solution are not that straightforward and can be influenced by many parameters. In the present section a brief overview of the nucleation, growth and stabilization processes applied to colloidal solutions will be given.

Nucleation and Growth

There exist various ways to promote nucleation and growth of nanoparticles, that include supersaturated or photo-induced formation of crystallization centers. A colloids poly-dispersity will be determined by how uniform nucleation happens and growth starts throughout the solution. For instance, while heating a solution into supersaturation it is highly unfavorable for a nucleation site to appear due to the high surface energy of crystallization centers. However, if a foreign center contaminates the solution, the energy barrier can be locally by-passed and the untimely triggering of the nucleation process will cause a large poly-dispersity.[131] Since it is desirable to obtain mono-dispersed colloidal solutions, nucleation conditions need to be defined, controlled and limited to a relatively short period of time. This can be achieved by either elevating the temperature of, or adding a strong reducing agent to the reaction solution, and leads to a short burst of homogeneous nucleation, which is quickly followed by supersaturated-relief where very few nuclei can be formed. Therefore, the formed nuclei grow slowly and uniformly governed by the diffusion-controlled process that promotes formation of mono-dispersed colloidal solutions.[131] We note that, mono-dispersed solutions can also be obtained by omitting the nucleation step and using seeds to directly continue with the growth phase. Following nucleation, the growth phase starts and depends upon the following parameters:

- Amount of available material

- Viscosity of the solution that controls diffusion of the reactants

- Susceptibility of the material to organize in a crystallographic lattice

- Impurities adsorption that limits the growth

- Inter-particle interaction that can lead to aggregation.

Thus, by increasing the amount of the source material after nucleation, the growth rate as well as colloidal size can be influenced.

Apart from using supersaturated solutions under specific nucleation-promoting conditions, photo-induced nucleation reactions can be used. In this case the nucleation phase is strictly controlled to the period of time the reaction solution is illuminated with an appropriate wavelength. Here, the photon energy is chosen either to ionize or to oxidize certain reactants in the solution and through this provide free electrons to reduce metal salts in dependence on their electronegativity. However, after the initial metal seed is formed, further interaction with the light source can occur due to the localized surface plasmon excitations described in Section 3.1. Where, irradiated metallic particles experience oscillations of electron density which, given the presence of free ions of metal salts in solution, act as a catalyst promoting the reduction of the ions at very specific sites of the nanoparticle also allowing their shape to be varied by modulating the frequency of the light source.[132–139]

After the colloidal solution is created, it reaches a state of dynamic equilibrium where a process known as Ostwald ripening occurs. Here, in the state of dynamic equilibrium dissolution and deposition processes take place continuously in order to maintain saturation solubility conditions. Therefore, in a poly-dispersed solution it is energetically favorable for smaller particles to dissolve over long aging periods in favor of larger particle growth due to their lower surface energy. The degree of Ostwald ripening is dependent on the solubility of the substance that forms the colloids but can, to a high degree, be overcome by introducing stabilizing and surfactant agents to the grown colloids.[131]

Surfactants and Inter-Particles Interactions

Surfactants are commonly bound to the surface of nanoparticles as capping agents, and can be classified by the charge carried by the binding part of the molecule:

- Anionic
- Cationic
- Non-ionic
- Ampholytic

Since a colloid is only considered to be kinetically stable when neither coalescence nor aggregation processes can take place and the inherent nature of metal particle dispersions are lyophobic, where given enough time they will separate from the solution, surfactants are commonly used to form stable dispersions. There are two ways of how to adsorb surfactants to a nanoparticle surfaces, namely, chemisorption and physical adsorption: [140]

- Chemisorption is very close to the formation of chemical bonds between the adsorbent and adsorbate, where electron exchange between the two takes place, making it a chemical reaction which is not always reversible.

- Physisorption is a process that involves relatively weak van der Waals forces between the adsorbent and adsorbate, which originate from the dipolar interaction of the species, and usually can be reversed.

The chemisorbed molecules can only form a monolayer, while the physically adsorbed molecules can be organized into multiple layers. The formation of the adsorbed surfactant layer is not an instantaneous process and is controlled by the thermodynamics of the solution. Furthermore, adsorption of a surfactant to the nanoparticle surface is favorable since its surface energy can be lowered, whose high value is the origin of the colloidal thermodynamic instability and can be further overcome by promoting electrostatic and steric repulsive forces. After the capping layer is formed on the nanoparticles surface, their stability can be described and examined.

Electric Double Layer at the Particles Surface

When nanoparticles are brought into a polar solution, they acquire ions to their surface that leads to an electric double layer formation. So, if surfactant ions are present they determine the surface charge of the colloidal particles, however, adsorption of dipolar molecules does not contribute to a net surface charge, but their presence can make a significant contribution to the nature of the electric double layer. The theory of electric double layer deals with the distribution of ions and electric potential in the vicinity of the particles. The electric double layer can be considered as consisting of two regions as it is depicted in **Figure 2**: an inner region (Stern layer) that includes adsorbed ions and a diffuse region, where ions are distributed in accordance to the influence of electrostatic forces and random thermal motion. The boundary of the diffusive layer is associated with the so-called slipping plane, which defines the border of the surrounding medium shell that is associated with the particles and is identified as hydrodynamic diameter,[131] which is used in description of the electrostatic colloidal stability of the particles and quantified as the ζ-potential.

The simplest quantitative treatment of the diffuse part of the double layer was developed by Gouy and Chapman, where the surface was assumed to be flat, ions to be point charges with the Boltzmann distribution, and immersed into a single symmetrical electrolyte. The results of the theoretical description show that the potential decreases exponentially in the diffuse part of the electric double layer and the layer behaves as a parallel capacitor. It should be noted that an exact solution using the Gouy-Chapman theory only exists for a flat surface in a Debye-Hückel approximation, where the electrostatic energy is considered to be significantly smaller in comparison to the thermal energy, and has therefore limited use when applied to colloidal solutions.[131]
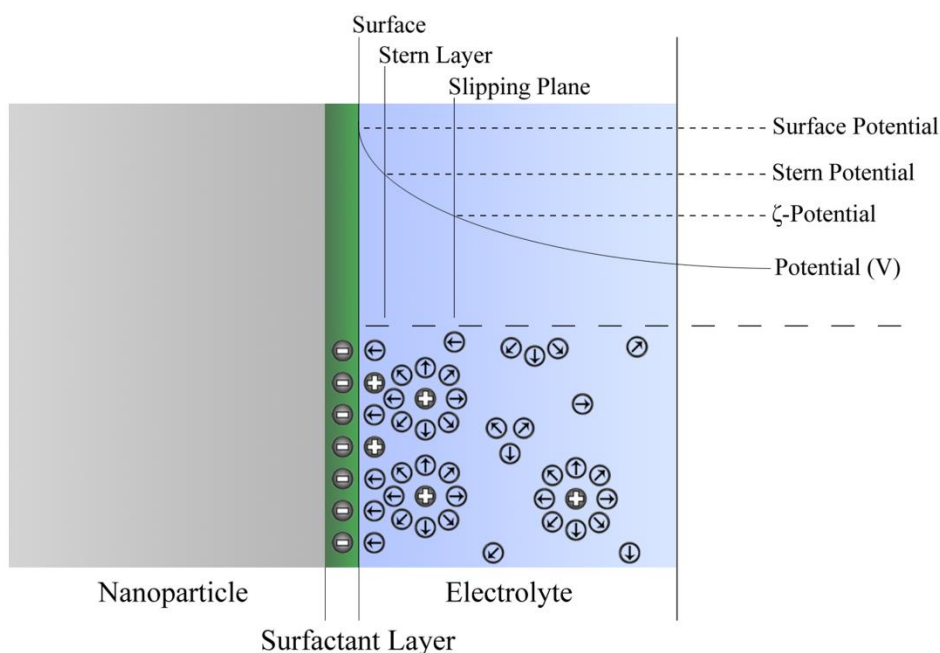
Figure 2 | Illustration of Potential Distribution | Schematic representation for the distribution of ions around a colloidal particle with an adsorbed anionic surfactant. The inner layer is called the Stern layer and consists of cations and permanent or induced dipoles. The outer diffusive layer contains both types of ions and dipoles. The slipping plane is a border of the diffusive layer and defines the hydrodynamic diameter of a particle.

Colloidal Stability

There exist two routes to achieve colloidal stabilization through using the properties of surfactants. If the surfactant species are ionic, then electrostatic stabilization can be considered and the principles developed for the electric double layer are implied. The origin of electrostatic stabilization lies in the electrostatic repulsive forces between the interacting particles through the charges accumulated in the electric double layers. The process is described in terms of the Derjaguin, Landau, Verwey and Overbeek theory where the total potential energy of the interaction between two particles is considered as a sum of all attractive van der Waals forces and repulsive forces originating from the electric double layer. The theory is developed in terms of the mean field approximation, which is when the particle is considered to be in a mean field created by its surrounding medium including

the other particles. One of the valuable results of the theory is its ability to predict the aggregation concentration when particles are no longer stable in solution as single species, by defining the potential barrier height that appears due to the repulsive forces between interacting species. Therefore, if the kinetic energy of a particle is large enough it can collide with another particle forming an aggregate. So, to promote long-term colloidal stability, polyvalent surfactants and low ionic strengths should be used.[131,140]

Polymer-induced steric stabilization is a second route to keep colloidal particles well-dispersed in solution and prevent their aggregation. The steric stabilization can be achieved by adsorption of a polymeric layer onto the surface of a particle where it can partially or completely shield the electric double layer and therefore prevent action of attractive van der Waals forces. Moreover, the inherent polymer behavior and its association with the solvent needs to be taken into consideration, since particularly under extreme concentration conditions, accounting for the affinity properties of the polymers, their use can result in bridging flocculation. Furthermore, by implementing polyelectrolytes that can be specifically adsorbed to the particles surface, a combination of both electrostatic and steric stabilization can be achieved by significantly increasing colloidal dispersive stability.[140]

4

Functionalization of Gold Nanoparticles

In this chapter we start our investigation by studying whether a higher number of thiol-groups in a linker molecule would be advantageous when functionalizing nanoparticles with DNA. To examine the obtained gold nanoparticles conjugated with DNA in terms of stability and reproducibility we also investigate if anion-exchange high pressure liquid chromatography can be a viable alternative and improvement for existing techniques to reproducibly obtain high yields of nanoparticles with a predefined number of short DNA strands attached. Furthermore, we develop on a protocol to functionalize gold nanoparticles with S-PEG-biotin and demonstrate its use with streptavidin bound to specific numbers biotin-functionalized DNA strands. Finishing with new results on the conformation that bound streptavidin with and without DNA has to nanoparticle surfaces.

4.1 DNA-Nanoparticle Conjugation and Purification with New DTPA Linkers

There is extensive literature on how to create DNA-nanoparticle conjugates. Initially we have evaluated three methods,[24,25,63] but chose to adapt a conjugation protocol for thiolated DNA[25,72] by using $2 \times$ DTPA linkers. This new method should produce highly stable DNA-nanoparticle conjugates formed by coupling four sulfur bonds between DNA and gold nanoparticles and will be discussed in the next section.

Preparation of DNA-Nanoparticle Conjugates with $2 \times$ DTPA

The commercially obtained nanoparticles used in this work were stored with a citrate capping agent. Here, citrate does not provide sufficient negative charge for the required colloidal electrostatic stability and ligand exchange to BSPP is necessary to increase the negative surface charge. This was achieved by mixing 10 ml of 20 nm citrate-coated nanoparticles with 6 mg of BSPP followed by overnight incubation at room temperature. To remove the citrate and remaining BSPP, an optimization of the original protocol was used where the particles were cleaned by centrifugation at 14000 g for 15 minutes, the supernatant removed and the pellet (ca. 20 µl) resuspended to 80 µl in 1.87 mM BSPP buffer, giving a final particle concentration of approximately 145 nM.

To gain high concentrations of nanoparticles with single or few DNA stands attached, an additional ligand exchange was performed with the goal of replacing BSPP with DNA-DTPA. Here the concentration ratios [nanoparticles] : [BSPP] : [DNA-DTPA] needed to be rebalanced to compensate for exchanging the original DNA-thiol to DNA-DTPA. Through anion-exchange high pressure liquid chromatographic separation (discussed later) we found adding 10 µl of 93.5 mM BSPP buffer, 10 µl of 20 mM phosphate buffered saline (PBS) at pH 7.4 and 15 µl of 100 µM 48-mer DNA-DTPA worked well. We note that the 25 mM NaCl, added as the saline component of the PBS buffer, is also an important factor as it allows for the DNA to overcome the nanoparticles electrostatic repulsion and bind.

The sample was then incubated at room temperature for three days in order to enable conjugation.

To separate the particles by charge exhibited from the bound DNA and to more permanently cap the particles; mPEG-thiol was chosen as it will replace BSPP but will not remove DNA-DTPA. Here, the reaction solution was diluted to 2 nM in 25 mM Tris buffer at pH 8.0 with 10 mM mPEG-thiol. After two hours of incubation at room temperature, PEGylation was complete and the solution was cleaned from reaction precursors by centrifugation for 30 min at 14000 g, followed by removing the supernatant to approximately 20 µl of precipitate and re-suspension of the pellet the initial volume with 40 mM NaCl with 25 mM Tris buffer at pH 8.0.

Purification of DNA-Nanoparticle Conjugates with AE-HPLC

To balance the protocol, purify the sample and isolate particles based on how many DNA strands are attached, we used high pressure liquid chromatography. For this we needed to isolate by charge, so we used a Dionex DNAPac Pa-100 anion-exchange column. One of the obtained chromatograms can be seen in **Figure 3**, where the sample was diluted to 50 nM with deionized water and 100 µl was injected at a flow rate of 1.2 ml/min corresponding to approximately 70 bars, with an increasing NaCl gradient. It features two distinct peaks, the first of which has its maximum at 8.1 minutes and the second representing a convolution of peaks between 18.8 and 20.3 minutes for unconjugated and conjugated nanoparticles, respectivly. Here, only 14% of the eluted particles are conjugated, suggesting that a higher DNA to nanoaprticle ratio should be used during sample preparation. However, since only 1 % of the particles are eluted, indecating that the column is being irriversable damaged, this could be a false assumption. It was obvious that we needed to develop new chromatographic methods to separate our system, which includes a new type of column as will be discussed in the next section.
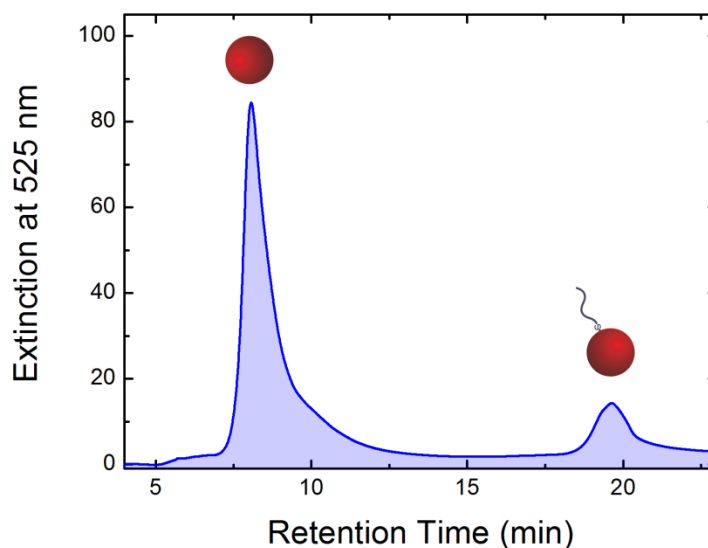
Figure 3 | Initial Chromatogram of Thiol-Linked DNA-Particle Conjugates | Chromatogram recorded at 525 nm features two distinct peaks the first is at 8.1 minutes and the second represents a convolution of peaks between 18.8 and 20.3 minutes for unconjugated and conjugated nanoparticles, respectivly. Here, only 14% of the eluted particles are conjugated with DNA and only 1 % of the injected particles are eluted, indecating that the column is being irriversable damaged.

4.2 New Purification Protocol for DNA-Nanoparticle Conjugates

To develop a new high pressure liquid chromatography separation method, a new column was required that would be more compatible with nanoparticle separation. The Dionex DNAPac Pa-100 anion-exchange column separates species by passing them around 13 μm, nonporous, polymeric resin with bound 100 nm positively charged quaternary amine-functionalized latex particles on their surface, as illustrated in **Figure 4a**. Since this column was designed to separate DNA, the steric hindrance and nanoparticle-to-nanoparticle interaction between the conjugates and the stationary phase is most likely too high to overcome. As a replacement we chose an YMC-BioPro QA anion-exchange column, which is packed with 5 μm, hydrophilic polymer beads with 100 nm pores containing

$CH_2N^+(CH_3)_3$, as illustrated in **Figure 4b**. These porous packing material is used in size exclusion columns, which are well known to have good recovery rates and give high yields, but most importantly, similar charge interaction without the steric hindrance and nanoparticle-to-nanoparticle interaction of the previous column.
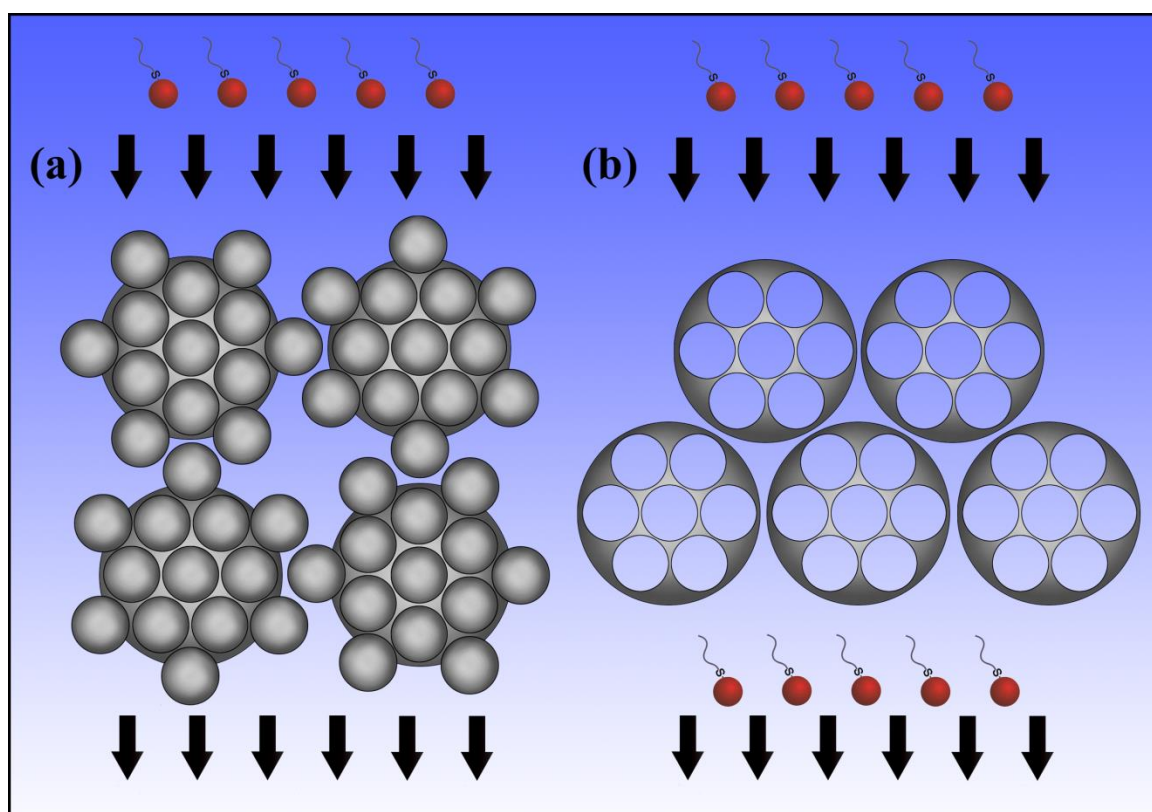

Figure 4 | Comparison between Different Column Packing Materials | (a) Illustrates an anion-exchange column which separates species by passing them around 13 μm, nonporous, polymeric resin with bound 100 nm positively charged quaternary amine-functionalized latex particles on their surface. (b) Illustrates an anion-exchange column, which is packed with 5 μm, hydrophilic polymer beads with 100 nm pores containing $CH_2N^+(CH_3)_3$.

To purify the DNA-particle conjugates with the new column, 100 μl of the sample was injected with a flow rate of 0.5 ml/min, corresponding to a pressure of about 27 bars, with an increasing NaCl gradient. The resulting chromatogram for 260 nm (red line) is depicted in

Figure 5 and exhibits four peaks, for unconjugated nanoparticles, BSPP, mono/poly-conjugated nanoparticles and DNA at 9, 13.7, 14.8, and 20.8 min, respectively. Here, the presence of BSPP and DNA peaks, show that the residual was not removed in the purification step. Furthermore, the first peak in chromatogram for 525 nm (blue line) is very broad for unconjugated nanoparticles. This, together with the presence of BSPP, implies that the ligand exchange with mPEG-thiol was not very successful, resulting in a wide range of different BSPP densities on the nanoparticle surfaces.
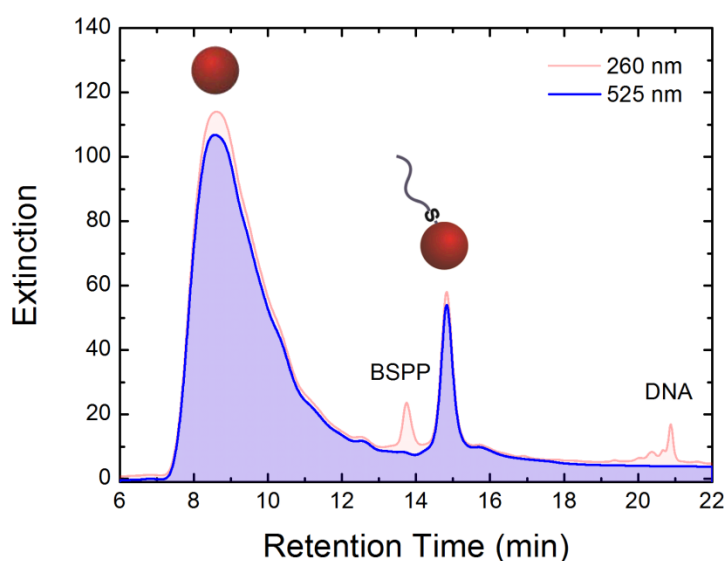
Figure 5 | Chromatogram of Thiol-Linked DNA-Particle with New Column | Chromatograms for 525 nm (blue curve) and 260 nm (red curve). Peak at about 9 min corresponds to unconjugated particles. Mono-conjugates elute at about 14.8 min followed by a small shoulder of poly-conjugates. For 260 nm, additional peaks at 13.7 min and 20.8 min are observable corresponding to unreacted BSPP and DNA, respectively.

However, the mono-conjugates peak, which is followed by a small shoulder that can be attributed to poly-conjugates, has a much larger area and the nanoparticle recovery is now increased up to 90 %. Nevertheless, approximately 86 % of the nanoparticles are unconjugated, and only 10 % and 4% are mono-conjugates and poly-conjugates, respectively, despite long conjugation times and a large excess of 130 DNA strands to a nanoparticle. So, while it is apparent that our new isolation protocol, using the YMC

column, solves the previous problems, focus must now be placed back on balancing the DNA-nanoparticle conjugation protocol as will be discussed in the next section.

4.3 New Protocol for DNA-Nanoparticle Conjugation with DTPA Linkers

The previously described protocol uses BSPP and its presence during purification causes many unwanted effects. While it is possible to remove any measurable sign of it, this can only be done by adding additional ligand exchange and cleaning steps. Here, since it has been suggested for thiolated DNA,[24] we develop a new protocol without using BSPP.

Preparation of DNA-Nanoparticle Conjugates

The first step of this protocol was to prepare the nanoparticle solution for the addition of DNA. Here, 1 ml of 1 nM commercially obtained citrate-coated 20 nm gold particles was concentrated to a 20 µl solution by centrifugation for 15 minutes at 14000 g and subsequently diluted with 60 µl of 20 mM PBS buffer at pH 7.4.

To gain high concentrations of nanoparticles with single or few DNA stands attached, ligand exchange was performed with the goal of replacing citrate with DNA-DTPA. Here the concentration ratios [nanoparticle]:[citrate]:[DNA-DTPA] needed to be rebalanced to compensate for exchanging DNA-DTPA with citrate instead of BSPP. Through the new anion-exchange high pressure liquid chromatographic separation we found adding 20 µl of 200 nM 48-mer 2 × DTPA-modified DNA worked well and improved the DNA to nanoparticle ratio from 130:1 to only 4:1. The sample was then incubated at room temperature for up to three days in order to enable conjugation.

To separate the particles by charge exhibited from the bound DNA and to more permanently cap the particles; mPEG-thiol was chosen as it will replace citrate but will not remove DNA-DTPA. So, the particles were diluted to 1 nM with 25 mM Tris buffer at pH 8.0 and 10 mM mPEG-thiol to a final concentration of 10 mM. After two hours of incubation at room temperature, PEGylation was complete and the solution was cleaned from reaction precursors by centrifugation for 30 min at 14000 g, followed by removing

the supernatant to approximately 20 µl of precipitate and the pellet resuspended to the initial volume with 40 mM NaCl with 25 mM Tris buffer at pH 8.0.

Purification of DNA-Nanoparticle Conjugates with AE-HPLC

To separate the different types of conjugates and balance the new protocol, the new anion-exchange high pressure liquid chromatographic protocol was used. Here, 100 µl of the conjugates were injected into the YMC-BioPro QA column at a flow rate of 0.5 ml/min with an increasing gradient of NaCl. The results can be seen for 260 nm and 525 nm in **Figure 6**, where the three peaks represent unconjugated, mono- and di-conjugated nanoparticles at 7.1, 15.0 and 16.0 min, respectively. Here, excluding BSPP from the protocol proves itself because there is now a sharp peak for the unconjugated particles, conjugation procedure seems to be adequate as there is now no DNA peak at 21 min for 260 nm, and there is now a clear peak for the di-conjugates with its shoulder representing further poly-conjugates.

We note that the attachment of DNA–DTPA to the nanoparticles still happens very slowly. After one day, the unconjugated peak dominates the sample and only 11% and 4% are mono- and poly-conjugates, respectively. After two days, the unconjugated peak considerably decreases and the sample contains 24% mono- and 28% poly-conjugates. After three days, the fraction containing conjugates is up to 68% and suggests that an even lower [DNA]:[nanoparticle] concentration ratio could be used.

The isolated conjugates can be used for a variety of interesting experiments. For instance, by preparing mono-conjugates with complementary strands, the formation of dimers with tunable inter-particle spacing would be possible. Di-conjugates could be used for the formation of chain structures. Such assemblies would be very interesting for, for example, energy transfer studies. Furthermore, the conjugates could be used as building blocks for a deterministic assembly of nanoparticles into higher order structures. Some of these topics will be discussed in the following chapter.
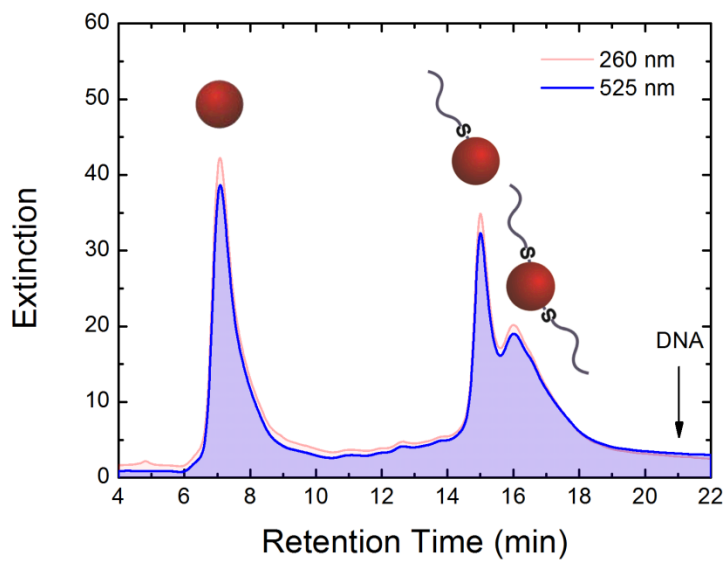
Figure 6 | Chromatogram of Thiol-Linked DNA-Particle Conjugates without BSPP | Chromatograms for 525 nm (blue line) and 260 nm (red line), after two days of DNA-DTPA functionalization. With longer conjugation times, the unconjugated peak gets smaller whereas the mono-conjugates and poly-conjugates fraction increases.

4.4 Functionalization and Purification Protocol of DNA-Streptavidin Conjugates

Our method of achieving DNA-functionalized gold nanoparticle structures requires a precise control over the number of DNA strands that are attached to streptavidin. Since streptavidin has four binding sites for biotin, making unoccupied or occupied by one, two, three or four DNA-biotin strands possible products, a functionalization protocol is required that will produce a solution with an even distribution of all four conjugates. This is followed by a purification step to isolate each type.

Functionalization Protocol of Streptavidin with DNA Strands

To create a solution of all four evenly distributed DNA-streptavidin conjugates, a solution of 5 µM of streptavidin in 10 mM Tris buffer, containing 100 mM NaCl, at pH 7.4 is prepared. 24-mer biotin-modified DNA was added to this solution and incubated for one hour on a shaker at room temperature. The required concentration ratio [streptavidin]:[DNA-biotin] will be discussed below. We note that, the high salt concentration ensures that an attachment of the negatively charged DNA strands to the negatively charged streptavidin molecules is possible.

Purification Protocol of DNA-Streptavidin Conjugates

In order to isolate the DNA-streptavidin conjugates; high pressure liquid chromatography was used[74] and an overview of the results will be given for the 1:1 concentration ratio of streptavidin and DNA-biotin. Here, 5 µM of streptavidin was mixed with 5 µM of DNA-biotin to a final volume of 100 µl and separated in the YMC column at a flow rate of 0.5 ml/min, corresponding to a pressure of 27 bars, with a mobile phase of 25 mM Tris and 40 mM NaCl at pH 7.4 for the first 3 minutes and then the NaCl concentration was linearly increased to 900 mM in 20 minutes.
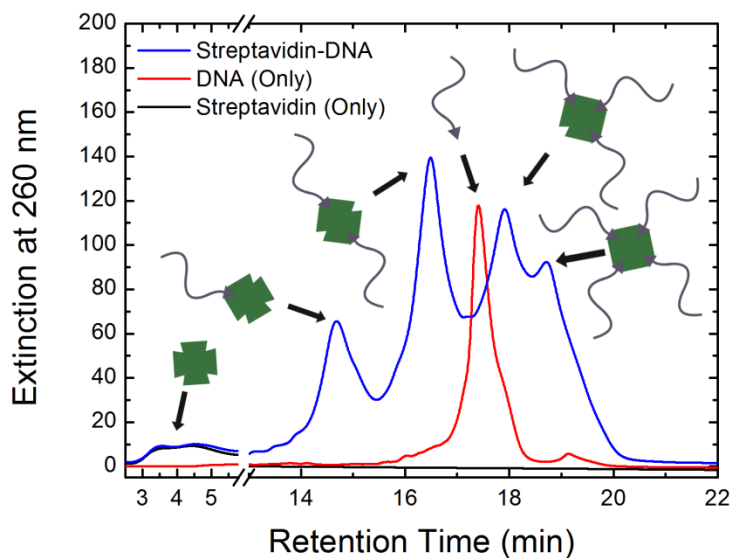
Figure 7 | Separation of DNA-Streptavidin Conjugates | Chromatograms for pure streptavidin (black line), pure DNA (red line) and for 1:1 DNA-streptavidin conjugates (blue line). Elution is monitored via the extinction at 260 nm. The inset shows the NaCl gradient applied for this measurement.

The results can be seen in **Figure 7** where six extinction peaks, for the conjugates and two reference samples, are recorded at 260 nm showing unconjugated streptavidin, DNA_{1-2}-streptavidin, DNA, and DNA_{3-4}-streptavidin conjugates at 3 to 5, 14.7, 16.5, 17.4, 17.9 and 18.7 minutes, respectively. Here the conjugates are well separated and the fractions can even be collected with a salt gradient instead of using large calibrated steps. We note that, the relatively long retention time of DNA-biotin is due to that biotin, no longer shielded by streptavidin, is free to add to the molecules interaction with the column, together with spatial changes of the streptavidin subunits upon binding with biotin,[79] which may decrease the interaction of the larger complex as a result of DNA base screening.

Control measurements were made with extinction spectroscopy, primarily to find the concentration of the separated fractions, and the results are plotted in **Figure 8a**. Here, an increasing number of occupied streptavidin binding sites leads to a shift of the extinction peak maximum to lower wavelengths starting from 282 nm for unoccupied streptavidin, down to 260 nm for streptavidin with four bound DNA strands, due to the influence that

the DNA peak's magnitude at 260 nm has on its convolution of the streptavidin peak at 280 nm.
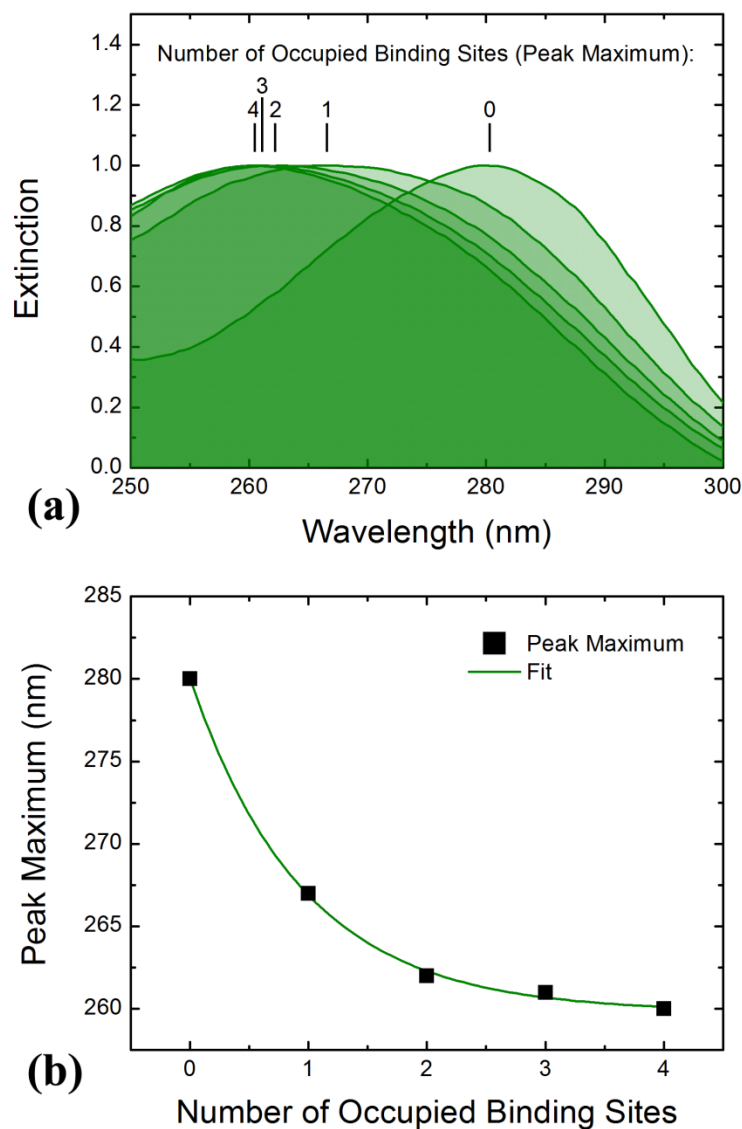

Figure 8 | Extinction of Purified DNA-Streptavidin Conjugates | (a) Extinction spectra of DNA-streptavidin conjugates purified fractions. (b) The peak maxima of the extinction spectra in dependence on the number of occupied streptavidin binding sites.

The concentration of the DNA-streptavidin conjugates was obtained by comparing the peak area of the data in **Figure 8a**, before it was normalized to peak height, to calibration measurements (not shown) and was found to be approximately 70 nM for the mono-

conjugated streptavidin and approximately 160 nM for di-conjugates. The exponential decay of peak maximum wavelengths as a function of occupied binding sites, seen in **Figure 8b**, confirms the purity of the fractions collected from **Figure 7**.

Analysis of Different DNA to Streptavidin Ratios

To balance the protocol for a solution where all four DNA-biotin conjugated with streptavidin species are evenly distributed, the influence on [streptavidin]:[DNA-biotin] concentration ratio was analyzed. To this end, DNA-biotin was added to the 5 µM streptavidin solution in a ratio range of [1]:[0.1 − 8.0]. As illustrated in **Figure 9a,** for an approximate [1]:[2] ratio, the resultant chromatograms where deconvoluted and the peak maxima estimated for the six peaks (streptavidin peak not shown) and the values used to build the histogram in **Figure 9b**. Here, the full range is visible, and as can be seen the ratio range [1]:[0.1 − 1.0] gives good results and is marked in blue. However, much of the streptavidin, which does not absorb light as effectively as DNA, remains in solution decreasing for an increasing ratio, and as expected the amount of conjugates has an inversely proportional behavior. Here, all four conjugates increase almost equally in concentration, demonstrating that the distribution is not just determined by binding stoichiometry, but also by the influence of charge of DNA and presence of biotin in the individual binding pockets. When the ratio is increased to values between [1]:[1.0 − 2.0] the amount of free streptavidin goes rapidly to zero, and disappears completely for [1]:[2.0] as well as the mono-conjugate peak reaching its maxima. This range, marked in green, represents the optimum concentration for DNA- streptavidin conjugate formation. This, because in the ratio range [1]:[2.0 − 4.0] the amount of mono- and di-conjugates rapidly disappears from solution. Furthermore, the system breaks down for the range [1]:[4.0 − 8.0], where at lower concentrations mostly tri- and tetra-conjugates are present, while at the highest concentration only tetra-conjugates with vast amounts of free DNA-biotin exist in solution.
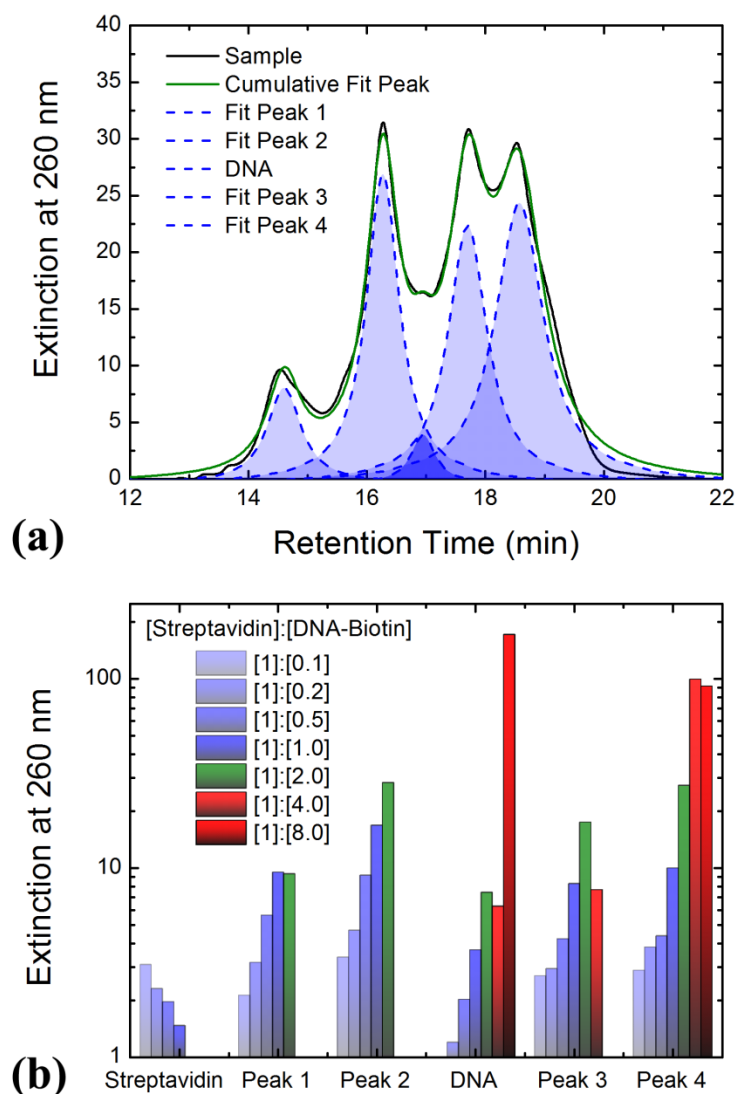
Figure 9 | Comparison of Streptavidin to DNA-Biotin Concentration Ratio | (a) A chromatogram of the [streptavidin]:[DNA-biotin] concentration ratio [1]:[2] (black line), the cumulative (green line) from the different deconvoluted peaks 1 to 5 (blue) that represent mono-, di-conjugates, DNA-biotin, tri- and tetra-conjugates, respectively. (b) A histogram showing a selection of deconvoluted peak maxima from the ratio series illustrating the unoptimized but working parameters in blue, the suggested optimum range in green and the unsuitable parameters in red.

It should be noted that at a concentration ratio of [1]:[10] between streptavidin and 152-mer DNA-biotin (in contrast to 48-mer used in this work) only between one and two

binding sites are occupied, which is reported to be due to the much larger negative charge of long DNA strands which suppresses the amount that can bind.[141]

4.5 Functionalization Protocol of Gold Nanoparticles with Biotin

Now that we have a way of obtaining streptavidin functionalized with one or more DNA strands, a way of procuring biotin functionalized gold nanoparticles is needed to create different structures around streptavidin.

Functionalization Protocol of Nanoparticles with Biotin

The commercially obtained 20 nm citrate-capped gold nanoparticles were used in this work. So, to gain high concentrations of nanoparticles, functionalized with small amounts of biotin, ligand exchange was performed between citrate and disulfide-PEG-biotin (S-PEG-biotin). Here, the nano-molar concentration ratio [1]:[300] of citrate-capped nanoparticles and S-PEG-biotin was found to work when the components were mixed together and allowed to react for 12 hours on a shaker at 25°C at 500 rpm. We note that, while the S-PEG-biotin concentration can be varied, concentrations in the micro-molar range led to irreversible aggregation at the purification step due to osmotic phenomena.[140] The reaction was terminated by adding high concentrations of mPEG-thiol to the solution to quickly replace the remaining citrate on the particle surface. This was achieved by placing 0.3 mM mPEG-thiol into the solution and letting it react for 2 hours on a shaker at 25°C at 500 rpm.[72] This passivation prevents non-specific adsorption of proteins or DNA to the particles metal surface,[142] significantly increases steric stability[140] required for the subsequent purification, and finally decreases absolute ζ-potential value of the colloids, at this pH and concentration range, which decreases the repulsion between the negatively charged nanoparticles and streptavidin,[143] allowing them to bind.

In the final step, the sample was purified from reaction precursors by 5 subsequent centrifugations at 14000 g for 15 minutes, where the supernatant was replaced by 1.8 mg/ml Tween 20 in 10 mM NaH_2PO_4 at pH 7.0[90] and in the final dispersion, 25 mM Tris buffer at pH 8.0 was used to adjust the particle concentration to 1 nM.

Characterization of the Biotin-Functionalized Nanoparticles

To make sure that only a small amount of S-PEG-biotin is bound to the surface and that streptavidin can bind to the biotin, we have investigated the ζ-potential of the solution during the conjugation and purification steps. The results of which can be seen in **Figure 10a** and show a histogram of the ζ-potential during the conjugation steps (green columns) for particles capped by citrate, S-PEG-biotin and S-PEG-biotin/mPEG-thiol in water, followed by after one and five purification steps of the S-PEG-biotin/mPEG-thiol capped nanoparticles in Tris-buffer at pH 8.0, in comparison to the ζ-potential a five times purified mPEG-thiol capped nanoparticles in Tris-buffer at pH 8.0 (blue box). Here, the mPEG-thiol passivation and thorough purification of the nanoparticle-biotin conjugates significantly decreases the ζ-potential to -14.3 mV which is just above that of PEG capped nanoparticles at -13.7 mV. These values show that only a small amount of S-PEG-biotin is present on the surface and that streptavidin will efficiently react with the conjugates.

The functionalization steps have been additionally proven by extinction spectroscopy, where the localized surface plasmon resonance peak position of the metallic nanoparticles can be used to detect chemisorption as it is extremely sensitive to change in the particles local environment. Here, a well-pronounced shift of the plasmon peak shows the chemisorption of S-PEG-biotin and mPEG-thiol molecules to the nanoparticle surfaces, as shown in **Figure 10b.**
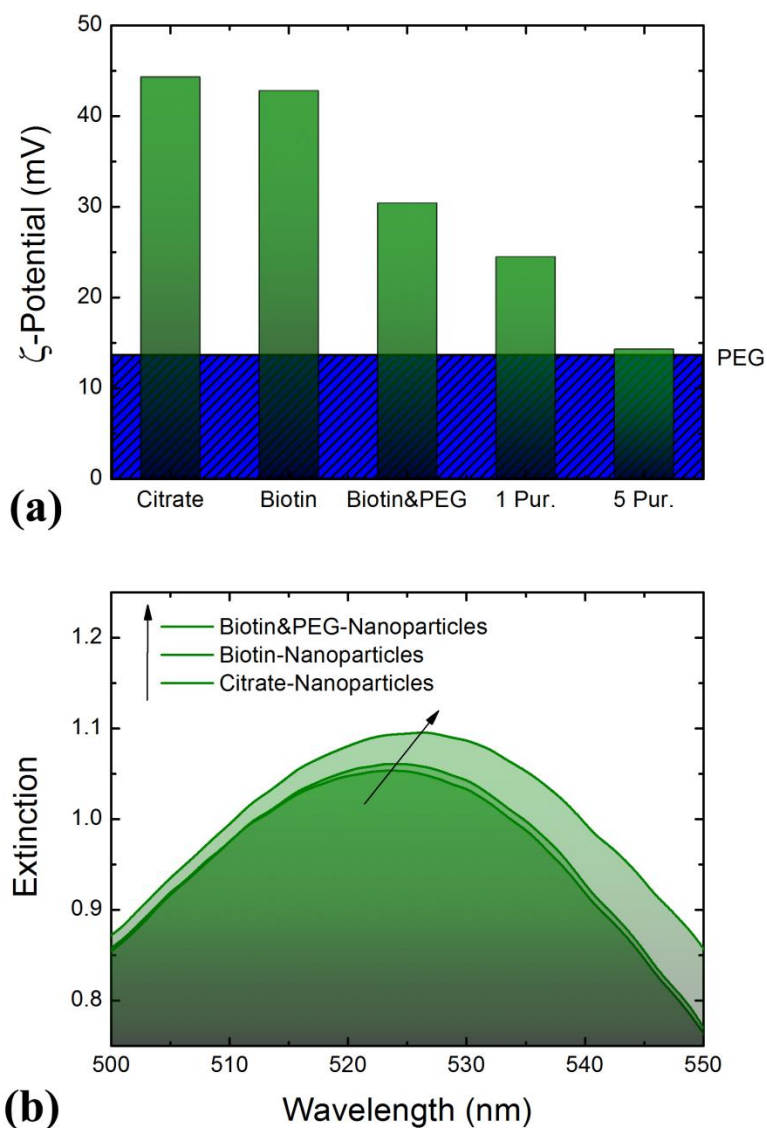
Figure 10 | Characterization of the Biotin-Functionalized Nanoparticles | (a) The ζ-potential absolute value during the conjugation steps for particles capped by citrate, S-PEG-biotin and S-PEG-biotin/mPEG-thiol in water, followed by after one and five purification steps of S-PEG-biotin/mPEG-thiol in Tris-buffer, in comparison to the ζ-potential for five times purified mPEG-thiol capped nanoparticles in Tris-buffer at pH 8.0 (blue box). (b) The plasmon peak shift for nanoparticles capped with citrate, S-PEG-biotin, and S-PEG-biotin/mPEG-thiol.

4.6 Preparation and Isolation of Novel DNA-Streptavidin-Nanoparticle Conjugates

The combination of the two protocols, described in Sections 4.4 and 4.5, allows for an additional novel way to create DNA-nanoparticle conjugates and simultaneously demonstrates the versatility of streptavidin. Moreover, it is a direct way to prove that the conjugation of biotin-nanoparticles and streptavidin-DNA protocols worked and more importantly, that they will work together before proceeding with more advanced structures. To conjugate nanoparticle-biotin with streptavidin-biotin-DNA a more direct, but in itself novel, path will be shown by mixing the four equally distributed streptavidin-biotin-DNA complexes and free streptavidin together with nanoparticle-biotin, instead of the more controlled variant of introducing the purified fractions that will be discussed in a later chapter. Afterwards, the conjugates can be characterized and individually isolated with anion exchange high pressure liquid chromatography according to the number of DNA strands attached to the nanoparticles.

Preparation of the Conjugates

The first step to form streptavidin bound DNA-nanoparticle conjugates, was to prepare a solution of 5 µM streptavidin in 10 mM Tris buffer at pH 7.4, containing 100 mM NaCl. Then, using the [streptavidin]:[biotin-DNA] concentration ratio discussed in Section 4.4, the 48-mer DNA-biotin was added to the solution and incubated for one hour at room temperature. The purified biotin-nanoparticles, prepared with the protocol introduced in section 4.5, were diluted to 1 nM in water and the DNA-streptavidin conjugates added to form a final concentration of 3 nM streptavidin and incubated for three days at room temperature. We note that, the formed conjugates, containing particles with different numbers of DNA strands attached to them, did not aggregate during incubation, which was confirmed by dynamic light scattering measurements (not shown here).

Purification of DNA-Streptavidin-Nanoparticle Conjugates

To separate the different types of conjugates, the new anion-exchange high pressure liquid chromatographic protocol was used and the recorded chromatograms are presented in **Figure 11a**, for 260 nm (red) and 525 nm (blue). Since the change in the nanoparticle inter-band transitions at 260 nm and local surface plasmon resonance at 525 nm will be somewhat equal, together with that streptavidin and DNA will only show up at 260 nm, subtracting the 260 nm from 525 nm extinction will give a good estimation of the free biotin-DNA and streptavidin in solution, and is plotted in **Figure 11b**. We note that, the chromatogram shows separation for a completely unoptimized [1]:[0.25] streptavidin-to-DNA concentration ratio, because it gives an impressive overview of all relevant peaks in one dataset. In the following interpretation of the chromatogram is presented.

In the first five minutes there is no separation of the 260 nm line from the 525 nm, meaning that all of the large amounts of left over streptavidin from the unoptimized concentration ratio are now bound to nanoparticles. Indeed, the next peak at 6.5 min is fairly small and corresponds to unconjugated biotin-nanoparticles, which supports the high usage of streptavidin, shows that the [nanoparticle]:[streptavidin] concentration ratio has been well-balanced, demonstrates the successful implementation of the mPEG-thiol passivation of the biotin-nanoparticles through their high reactivity, and most importantly proves that the protocols work nicely together for later use with larger structures.

Supporting information for these statements is given from the peaks between 8.1 and 10.4 minutes, which show the usage of the free streptavidin through the four convoluted peaks corresponding to streptavidin-nanoparticle conjugates. That these peaks are the streptavidin-nanoparticles is demonstrated by their equidistance and the larger gap from the unconjugated particles. Interestingly, this separation implies that the protocol allows for a maximum of four streptavidin to one nanoparticle and the distribution suggests that charge repulsion plays a large role. This would increase the binding symmetry of streptavidin around the particle and considering that the protein has a diameter of 5 nm, in comparison to the nanoparticles 20 nm diameter, and also supports four fold binding symmetry.
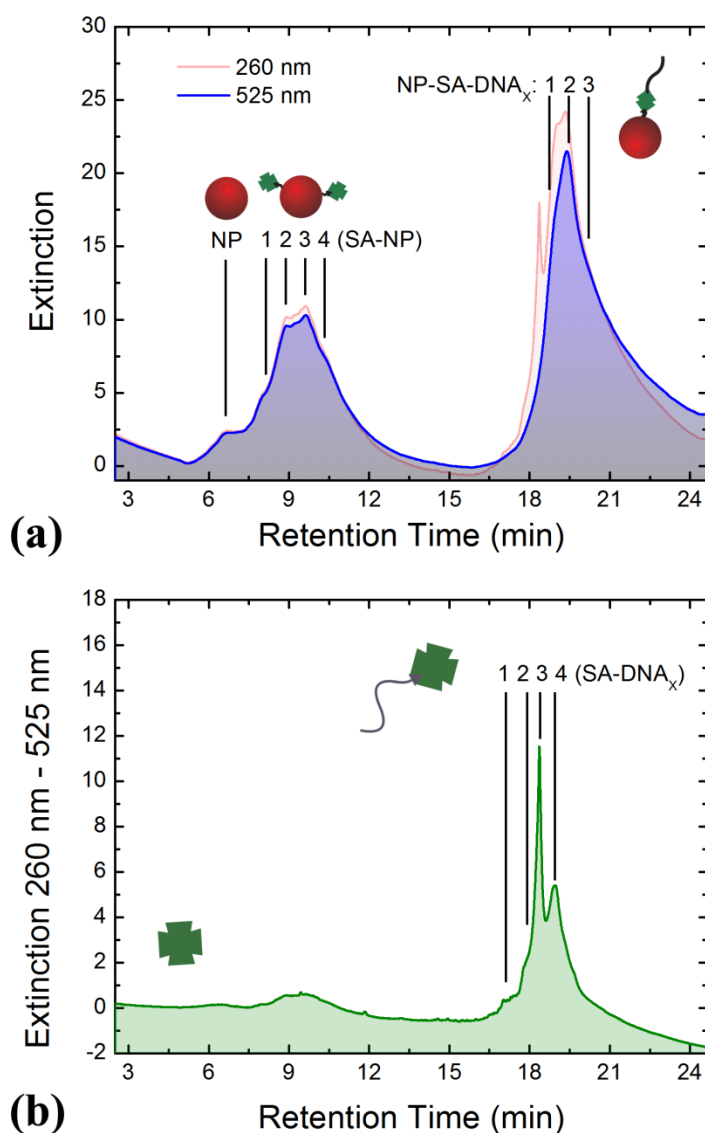
Figure 11 | Chromatogram of Different Conjugates | (a) Chromatograms at 260 nm (red) and 525 nm (blue). (b) Chromatogram for nanoparticle-free streptavidin and DNA-biotin as subtraction of chromatographic signals at 260 nm and 525 nm.

For the probably eight peaks situated between 17.1 and 20.2 minutes, the subtracted data in **Figure 11b** will be discussed first. These data have a striking similarity to the chromatogram in **Figure 9** and also corresponds to the elution of the different DNA-streptavidin conjugates, most likely also hiding the biotin-DNA peak. Here it can be seen that only small amounts of free streptavidin holding one and two DNA stands in solution

remain. The peak height of streptavidin holding four DNA stands, which cannot react, implies that also most of the streptavidin holding three DNA stands are unreacted. This, together with the two, possible three peaks in **Figure 11a**, which are dominated by the second, indicates that the charge repulsion is too high to allow more than three DNA strands to a particle with a maximum of two DNA strands to one streptavidin. The large amount of particles functionalized with a combination of 1 to 4 streptavidin proteins holding 1 to 2 DNA, totaling in not more than three, also explains the wide peak.

This protocol offers the advantage of a more direct approach, avoiding cumbersome purification steps, and produces a chromatogram revealing peaks that are clearly separated, which is even more pronounced with the optimized streptavidin to DNA-biotin ratio, so the fractions can be independently isolated and collected.

5

Assembly of Nanoparticle Structures

In the present chapter we investigate how to obtain a high enough control over the interlinking process of biotin-functionalized particles and streptavidin, to achieve high yields of small particle complexes and additionally enrich them under physiological conditions through size exclusion chromatography. While these studies focus on aggregating biotin functionalized particles with low concentrations of streptavidin, we also investigate if high concentrations can also be used to achieve high yields of small particle complexes by hindering aggregation through saturation of the binding sites. Furthermore, by applying the developed protocol for controlled formation of the nanoparticles dimers and studied method to separate DNA-streptavidin conjugates by the number of DNA strands we create DNA-functionalized dimers and by exploiting Watson-Crick base pairing of DNA, examine a new way to build nanostructures.

5.1 A New Study on Streptavidin-Induced Particle Interlinking

After gold nanoparticles have been functionalized with biotin, the streptavidin-induced aggregation process can be studied. Here, we investigated the aggregation process, at low ionic strengths, in dependence on the streptavidin concentration.

Functionalization Protocol for Streptavidin-Induced Particle Interlinking

In accordance with the protocol discussed in Section 4.5, biotin functionalization of citrate capped nanoparticles was performed with ligand exchange between citrate and S-PEG-biotin at a nano-molar concentration ratio of [1]:[300], the reaction terminated by adding 0.3 mM of mPEG-thiol to the solution, and purified by centrifugation to a final concentration of 1 nM in 25 mM Tris buffer at pH 8.0. Here, the protocol needed to be balanced to find the optimum concentration ratio between [nanoparticle]:[streptavidin], which will be discussed below.

Analysis of Different Nanoparticle to Streptavidin Ratios

To find the optimum concentration ratio [nanoparticles]:[streptavidin], a concentration series was made for the nano-molar range [1]:[0.1 − 50]. The difference in extinction was so large it can be visually quantified, as demonstrated in **Figure 12a**, where photographs of the colloids for increasing protein concentration can be seen from left to right. Here, the color changes from ruby red to purple, due to localized surface plasmon resonance peak shifts form aggregation coupling effects, and goes transparent due to precipitation.[11,90]

The dependence of streptavidin concentration on the aggregation process is also shown in **Figure 12b**, for scattering intensity (green) and extinction at 600 nm (blue), one hour after streptavidin addition. We note that, the change from measuring the local surface plasmon resonance at 525 nm, which is more responsive to nanoparticles, is due to that 600 nm is

the well-known "semi-empirical flocculation parameter" and more susceptible to aggregates,[90,104] as plasmon coupling broadens the localized surface plasmon resonance peak to lower energies with increasing aggregate size.[5,75,90]
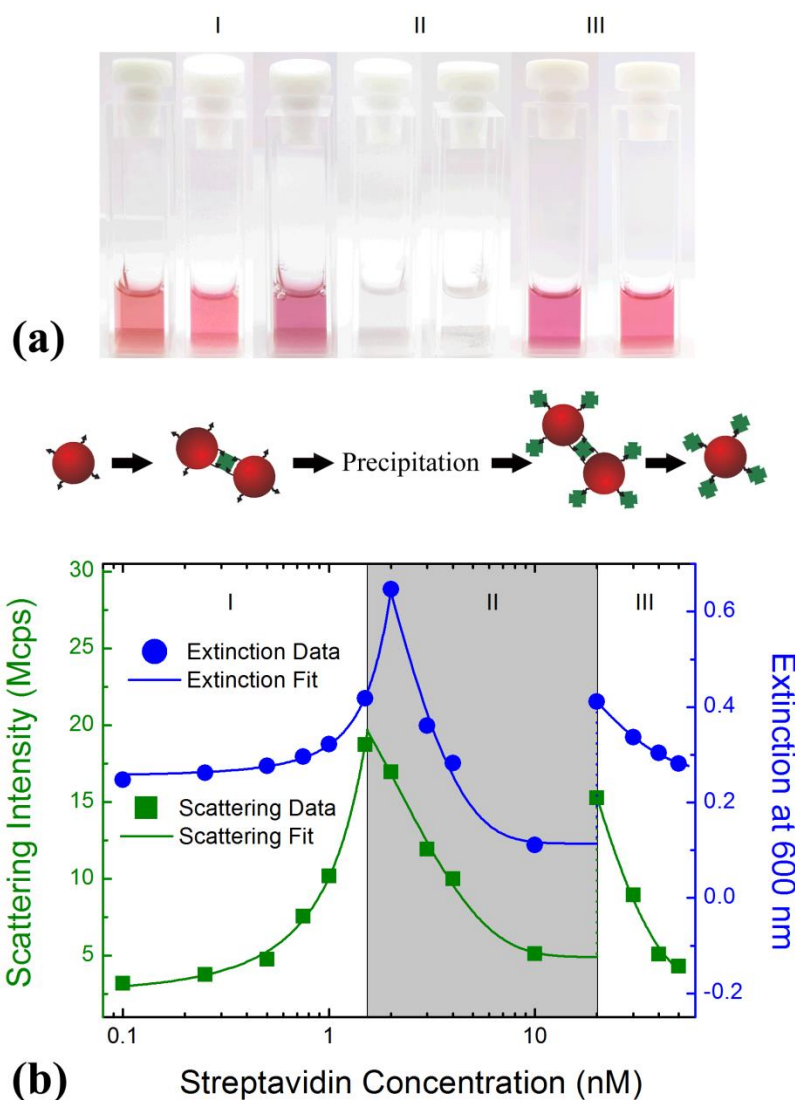

Figure 12 | Streptavidin Concentration Dependent Aggregation | After 60 min of aggregation time of 20 nm biotin-functionalized gold nanoparticles (a) shows photographs from left to right and (b) shows the scattering intensity (green) and extinction at 600 nm (blue), for increasing streptavidin concentrations. Here, region (I) corresponds to the aggregation regime of unsaturated nanoparticles, region (II) – precipitation, and region (III) − aggregation of saturated nanoparticles.

The presented plot has two peaks dividing it into the three aggregation regimes that are discussed below.

In region (I), aggregation of unsaturated nanoparticles occurs for concentrations smaller than 2 nM. Here, the number and size of unsaturated nanoparticle aggregates, which are stable in solution, increases for higher concentrations. Starting at low streptavidin concentrations, the aggregation is limited due to the lack of streptavidin for the particles to interact with, but gradually grows until it reaches the first maximum not far from the [1]:[1] concentration ratio. We note that, the initial extinction values should be close to zero, but are convoluted with the 525 nm local surface plasmon resonance peak shoulder from free nanoparticles. Here, the scattering intensity gives a better estimate as it is highly sensitive to larger scattering object diameters ($I \sim d^6$).

In region (II), precipitation occurs between 2 and 11 nM. Here, larger amounts of the total number of particles precipitate form solution for increasing concentrations due to the formed agglomerates size starts to exceed that which can be supported as a stable colloid. The threshold between regions (I) and (II) is blurred, but a better prediction is expected from the scattering intensity, as its high sensitivity to large particles is a better estimate in contrast to the 600 nm extinction that gives a good approximation of the intermediate sized colloid concentration. Towards the end of region (II), nearly complete precipitation of the aggregates ensues and the solution becomes clear. Here, extinction becomes more accurate as large precipitates severely influence the scattering intensity.

In region (III), aggregation of saturated nanoparticles occurs at 11 to 50 nM. The high streptavidin concentration is now capable of blocking the formation of unstably large aggregates due to the limited amount of remaining unoccupied binding sites. Here, the aggregation size will decrease for increasing concentrations until the individual particles are completely pacified. Region (III) is also difficult to quantify, since it is most likely very dependent on reaction and diffusion limited kinetics where the outcome can be altered by, for example, titrating the biotin-nanoparticles into streptavidin or vice versa. The first indication of this comes from that the saturation and capping of the particles takes place at

50 fold higher streptavidin concentrations than nanoparticles, which also coincidently corresponds to the number of proteins that would geometrically fit onto a particles surface. However, the number of bound proteins is limited due to mutual repulsion of the species,[143] and while increasing the salt concentration to 10 mM does little to change regions (I) and (II), it offsets region (III) to higher concentrations where it is significantly broadened, ending at 1000 nM for complete passivation.
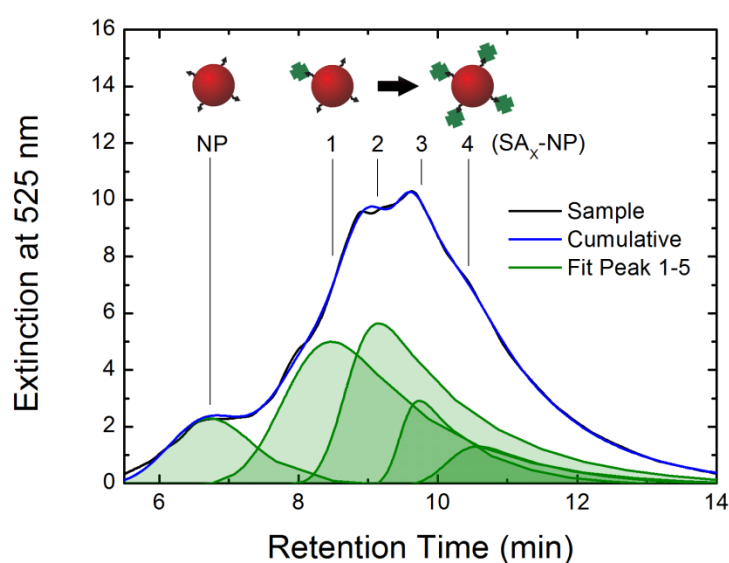

Figure 13 | Chromatogram of Streptavidin−Nanoparticle Conjugates | For the [nanoparticle]:[streptavidin] concentration ratio [1]:[0.25] (black line), the cumulative (blue line) from the different deconvoluted peaks 1 to 5 (green) that represent unbound, mono- to tetra-conjugates, respectively.

Furthermore, the anion exchange chromatogram from a solution with an intermediate salt concentration of 0.1mM NaCl is illustrated in **Figure 13**, and shows the deconvolution of three distinctive peaks and two shoulders corresponding to unbound and one to four bound streptavidin proteins. Since streptavidin is negatively charged at the pH used in this work, and there is no sign of additional peaks in the chromatogram, it is highly likely that region (III) consists of nanoparticles saturated with four bound streptavidin proteins due to mutual repulsion of the species. We note that a small number of additional proteins may bind in at high salt concentrations. This leads to that the overwhelmingly high concentrations of

streptavidin needed to enter region (III) is necessary to overpower the reaction kinetics and has little to do with stoichiometry.

Aggregation Kinetics

To get a better insight into the aggregation mechanism, we studied the kinetics of the process for the three regions at low salt concentrations. For this, extinction spectra were recorded over time and the first 60 min from streptavidin addition presented in **Figure 14**. We note that the linear drift together with the baseline-offset was subtracted and the data normalized to the value at 60 min. For regions (I) and (III) aggregation stops within the first minutes and the formed complexes stay stable over several weeks at room temperature. However, for region (II), especially for the boundaries between (I) and (II), the particle assembly occurs over longer periods of time between hours and days. But the majority of the created aggregates forms rapidly and precipitates completely within one hour leaving a colorless solution behind.
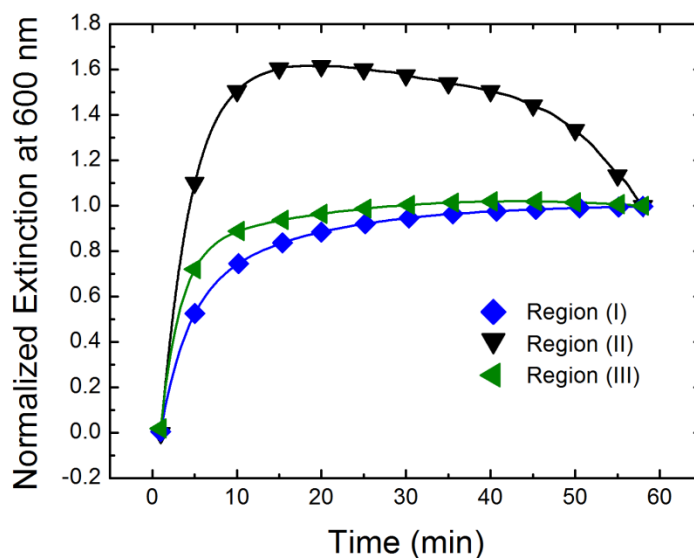

Figure 14 | Streptavidin Concentration Dependent Aggregation Kinetics | Typical aggregation kinetics of biotin-coated gold nanoparticles in region (I) − aggregation regime of unsaturated nanoparticles, (II) − precipitation and (III) − aggregation of saturated nanoparticles.

Thus, the presented results show an effective way to obtain small stable aggregates which are either saturated or unsaturated with streptavidin. Now, we need to characterize the product to isolate specific types of conjugates.

5.2 Characterization and Isolation of the Streptavidin-Linked Particles

To separate the different types of conjugates for dimer isolation, it was first necessary to balance the previously discussed protocol, through characterization of the stable aggregates, to gain the highest concentration of dimers and then purify this optimized product by size exclusion chromatography to isolate the dimers.

Characterization of the Aggregate Size Distribution by Dynamic Light Scattering

We analyzed the aggregate size distribution, by measuring the hydrodynamic diameters resulting from streptavidin-induced particle interlinking with dynamic light scattering for different streptavidin concentrations, to balance the protocol to obtain a high yield of dimers. **Figure 15** presents the size distributions weighed both by intensity (black) and number (blue), the unstable aggregation region (red background) and the region where dimers are most likely to be found (green box). Starting from the bottom, the stoichiometrically balanced protocol of 0.5 nM, which provides one streptavidin to two particles, is considered. The weighed by intensity data, which is more sensitive to larger aggregates, shows that larger aggregates are forming. However, since the peak position is not far from the nanoparticle core size of 20 nm, for the more realistic weighed by number of particles distribution, it shows that most species are present in the monomeric state and that the PEG coating does not increase the scattering by much. Increasing the streptavidin concentration the following is observed: 1 nM results in formation of 30 nm aggregates weighed by number, passing the unstable aggregation region (II), the 50 nM in region (III) gives a similar behavior to 1 nM as the hydrodynamic diameter distributions for intensity and by number goes to 40 nm and 27 nm, respectively. The larger hydrodynamic diameter is expected for region (III), due to that the S-PEG-biotin-streptavidin molecule will increase the particle radius by approximately 8 nm but does not scatter as effectively as the nanoparticle.[80]
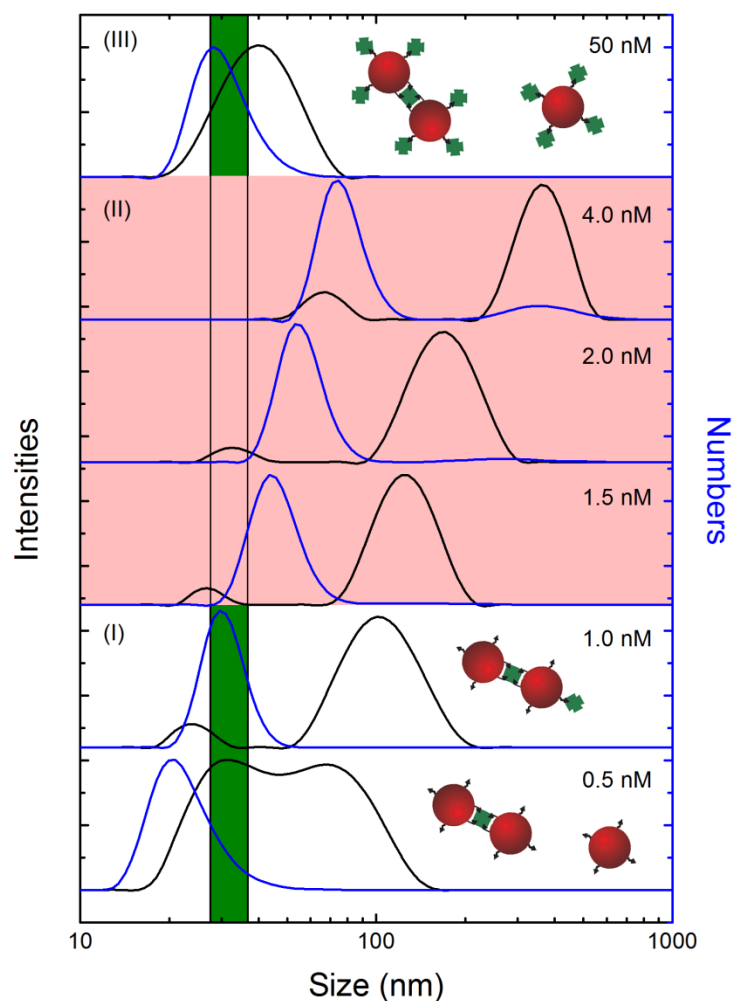
Figure 15 | Dependence of Hydrodynamic Diameter on Streptavidin Concentration | Measured by dynamic light scattering: distributions are weighed by intensity (black) and number (blue).

To find the size distribution that geometrically corresponds to two particles bound together with streptavidin, its effective hydrodynamic diameter needs to be known. For this, the dimensions of a cylinder can be used, by applying the Einstein-Stockes equation to the translational diffusion coefficient D_t of a prolate ellipsoid, to calculate its hydrodynamic diameter, d_H, in solution as follows:

$$d_H = \frac{k_B T}{3\pi\eta D_t} = L_C \cdot \left[ln\left(\frac{L_C}{d_C}\right) + 0.565 \cdot \left(\frac{d_C}{L_C}\right) - 0.100 \cdot \left(\frac{d_C{}^2}{L_C{}^2}\right) + 0.312 \right]^{-1} \qquad (2)$$

Here, η is the solvent viscosity, L_C and d_C are the length and diameter of the cylinder, respectively.[144] Thus, if we assume the dimer to be a cylinder, having the dimensions $L_C = 4/3 \cdot d_C$, where d_C is also considered as the nanoparticles diameter, the effective hydrodynamic diameter would be in the range of 28 to 37 nm for dimers with no streptavidin ($d_C = 20$ nm) to dimers fully covered ($d_C = 27$ nm), respectively. This target is depicted in **Figure 15** as a green box and shows that the protocol should yield samples with high dimer content for streptavidin concentrations of around 0.7 and 45 nM.

Characterization of the Aggregate Size Distribution by Transmission Electron Microscopy

To confirm the results from dynamic light scattering, we examined the streptavidin concentration series with transmission electron microscopy. Here, the histogram in **Figure 16b** shows the analysis of approximately one thousand species for 0.5, 1 and 2 nM streptavidin concentration. Starting from 0.5 nM streptavidin, about 15% of the particles form dimers, a majority are still monomers, but most end up forming larger agglomerates. Increasing the streptavidin concentration over 1 nM, results in a steady loss of monomers and dimers for larger aggregates and for still higher concentrations, for example 2 nM, large nanoparticle clusters of over 100 particles are exclusively found (not shown here). These data seem to be in agreement with the previously presented extinction and scattering results. We note that some aggregates are most likely formed during deposition of the sample on the electron microscopy grid, and reference sample showed an error of 9%.
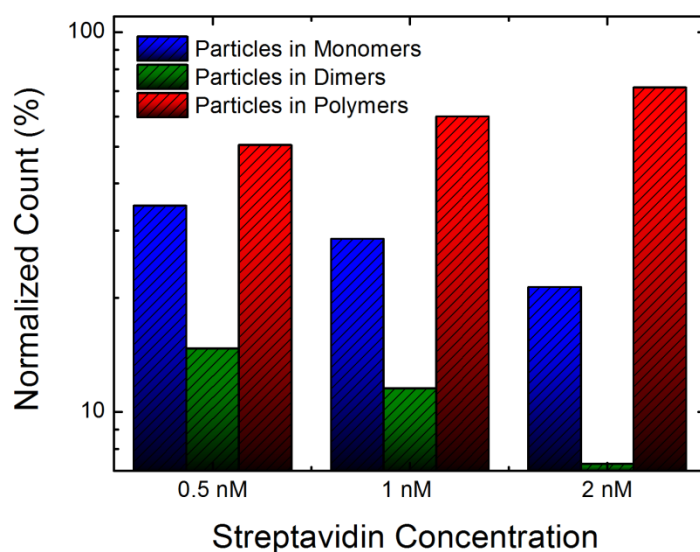
Figure 16 | TEM Aggregate Size Analysis | A histogram presenting the relative amount of dimers in solution for different streptavidin concentration, where the number of particles associated with monomers, dimers and multi-mers are shown normalized to the total amount of particles counted for one streptavidin concentration.

Isolation of Streptavidin-Linked Particles

Now that the protocol is balanced to yield the largest amount of dimers possible, high pressure liquid chromatography was employed, with a Tosoh TSK-GEL G5000PWxl size exclusion column, to isolate the protein-linked particles.[107] This technique separates in dependence on hydrodynamic diameter, by the means of a stationary phase with 10 µm hydroxylated polymethacrylate beads with 100 nm mean pore size, where the largest species elute first. Here, the samples were injected at 1 nM concentration and the results shown in **Figure 17a,** for extinction at 525 nm (black line), the deconvolution fits of two peaks (blue dash) corresponding to conjugated followed by unconjugated particles, their cumulative (green line) and the suggested retention time with the highest yield of dimers (gray box).
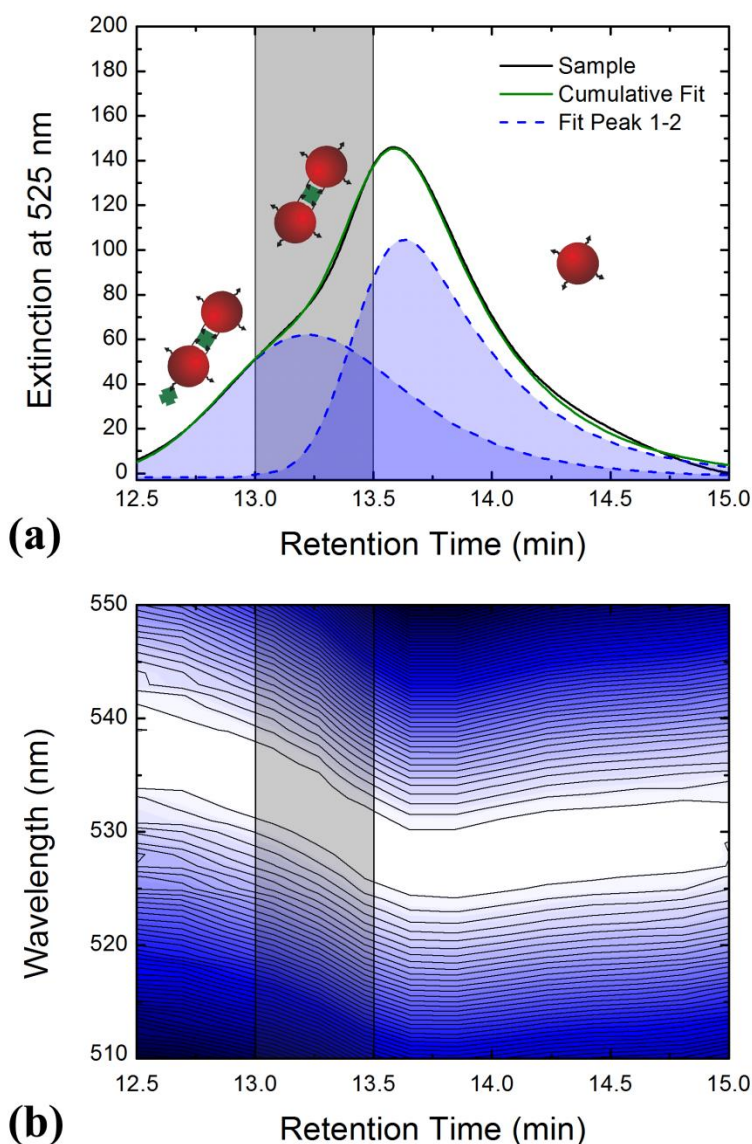
Figure 17 | SEC Purification of Dimers | (a) The size exclusion chromatogram for the obtained aggregates (black line) show two distinct peak fits (dashed blue) for conjugated and unconjugated particles and their cumulative (green line). (b) Normalized extinction spectra plotted for wavelength over retention time.

The peaks were fit by using exponentially modified Gaussian functions,[122] that accounts for the tailing asymmetry which was confirmed with and initial fitting values used from a chromatogram for single particles (not shown here), and significantly overlap due to the differences in mass, effective size and column interaction between the studied aggregates and single particles. The fit for the conjugate peak is much broader than for the

unconjugated, which is due to its contents of different types of multi-mers with varying amounts of streptavidin on the surface and supported by the dynamic light scattering and transmission electron microscopy data presented in **Figure 15** and **Figure 16**, respectively. Furthermore, the shift of the localized surface plasmon resonance peak position over retention time, seen for values normalized to peak maxima in **Figure 17b,** confirms the presence of larger species due to its movement from lower energies, which correspond to the plasmon coupling effects in aggregates, to higher energies leveling off at a wavelength consistent with single particles.

To find the optimum retention time for extraction, the samples were analyzed with dynamic light scattering. Here the results weighed by intensity and number from a sample with no streptavidin, before and after size exclusion, can be seen in **Figure 18a**. As expected, the monomers show a hydrodynamic size of just over 20 nm, and a sample before size exclusion run shows that the streptavidin concentration was close to optimum by its relation to the green box marking the region for dimers. To show the highest contrast, a sample was collected for the large aggregates during a retention time of 12.4 to 13.2 minutes and the scattering peak position represents the larger unwanted aggregate sizes seen previously but still crosses significantly with the dimer region. Thus the optimum retention time for collection ends up between 13.0 and 13.5 minutes. The results from an optimized fraction can be seen from a transmission electron microscopy micrograph in **Figure 18b**, where dimers can be seen with a small space in-between resulting from the dried streptavidin still keeping the particles apart. We note that, enrichment by sucrose gradient density centrifugation of the optimized protocol forces a high percentage of the large aggregates out of solution enabling easier isolation by size exclusion (not shown here).
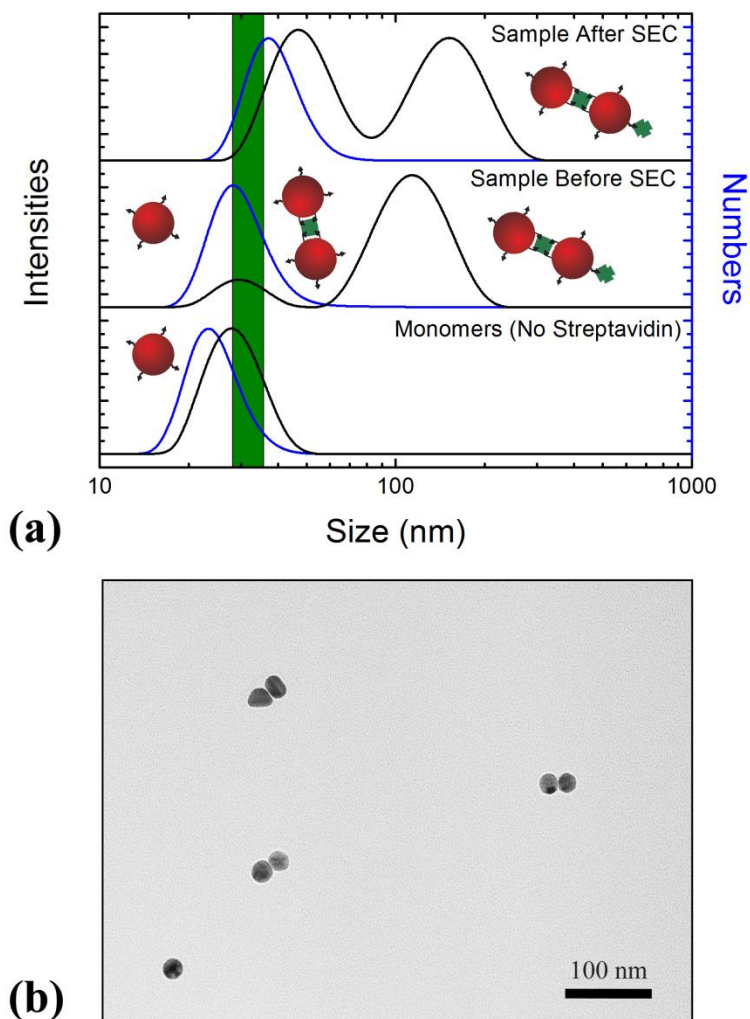
Figure 18 | Size Distribution of the SEC Purified Streptavidin-Linked Nanoparticles | (a) Comparison of the number- (blue line) and intensity- (black line) weighed size distributions of monomers from a sample with no streptavidin added, a sample before size exclusion, and a sample collected for the retention time of 12.4 to 13.2 minutes. (b) Transmission electron micrograph of an optimized sample fraction. All of the particles from the original picture have been moved together to enable viewing at high magnification.

5.3 DNA-Programmed Assembly of Gold Nanoparticle Dimers

To use DNA functionalized dimers to build larger structures, the previously discussed protocol needs to be modified. Streptavidin is a homotetrameric protein with dihedral D2 symmetry where the order in which each subunit specifically binds to one biotin will predict their spatial arrangement and therefore needs to be taken into consideration. There are various ways to depict the binding angles between biotin and streptavidin due to that the biotin group is at an angle on the functionalized molecule and two of the binding sites of streptavidin are more or less, but not precisely, pointing down in relation to the remaining two that are on the opposite side pointing upwards, making a wide variety of binding angles possible. Here, as long as the binding sites are not occupied, the second of two species to bind will almost always be arranged on the opposite side from the first,[75,90] and dimer formation will eventually occupy all four binding sites of an unoccupied protein. It would therefore not be possible to bind biotin-DNA in-between the dimers once they have bound, and so the dimer must be formed with streptavidin which already is occupied by biotin-DNA. Since, the results of Section 4.6 describe that particles will be functionalized with a combination of 1 to 4 streptavidin proteins each holding 0 to 2 DNA strands, but not more than three total strands to a particle, only the fractions containing streptavidin with one and two DNA strands need to be collected. Particles will form with 1 to 3 DNA_1-streptavidin conjugates and 0 to 1 DNA_1-streptavidin with one DNA_2-streptavidin, where the DNA strands are initially pointing outwards from the surface and able to rotate away from an incoming binding particle as it binds, forming a dimer with one or two DNA strands connected to the dimers symmetrical rotational axis. Here, the DTPA DNA_1-nanoparticles from Section 4.3 can be used as terminators to end the structures with a nanoparticle. Finally, due to the amount of different species created, the DNA functionalized monomers and dimers should be purified and the separated fractions collected from anion-exchange and size exclusion chromatography, as suggested in Sections 4.3 and 5.2, respectively, and can now be further assembled by mixing with similar structures, containing their DNA complement strands.

DNA-Functionalized Streptavidin-Induced Particle Interlinking

To create DNA functionalized dimers, two separate batches of DNA-streptavidin conjugates, each containing the complementary DNA-biotin strand to the other, needs to be separated with anion-exchange chromatography as shown in Section 4.4. It should be noted that significant cross contamination will occur due to the convolution of the chromatogram peaks and therefore the DNA$_1$-streptavidin fraction will contain some DNA$_2$-streptavidin as will the DNA$_2$-streptavidin fraction contain DNA$_1$-streptavidin, free DNA-biotin and DNA$_3$-streptavidin. In accordance with the protocol discussed in Section 4.4, an evenly distributed DNA-streptavidin conjugate solution was made by adding 74-mer biotin-modified DNA, at the found concentration ratio of [1]:[1-2], of 5 μM streptavidin to DNA-biotin at high salt concentrations. The fractions containing monomers and dimers were then obtained by anion-exchange chromatography. Biotin functionalization of citrate capped nanoparticles was performed, according to the protocol discussed in Section 4.5, with ligand exchange between citrate and S-PEG-biotin at a nano-molar concentration ratio of [1]:[300], the reaction terminated by adding mPEG-thiol to the solution, and purified by centrifugation. The obtained DNA-streptavidin dimer fraction was then mixed together with biotin-nanoparticles using a rebalanced protocol to overcome the higher repulsion due to the DNA bound to the streptavidin.

Increasing the salt concentration in the protocol for pure streptavidin to 10 mM, as seen in **Figure 19a**, results in an emphasized nanoparticles dimer formation region where crossing [1]:[0.75] concentration ratio causes precipitation of larger species before the main aggregation in region (II) starts. However, the effects of higher repulsion are obvious in **Figure 19b**, where the influence on dimer formation is shown for extinction at 600 nm for DNA$_{0-2}$-streptavidin for both 0 and 10 mM of NaCl. Here, the increased repulsion of the DNA-streptavidin complexes makes their behavior sink well below that of 0 mM NaCl pure streptavidin giving unacceptably low yields even at 10 mM. However, after rebalancing the protocol, to final NaCl concentrations of 45 mM for mono-conjugates, 55 mM for di-74-mer DNA and 46 mM for di-c74-mer DNA, the yield was adequate.
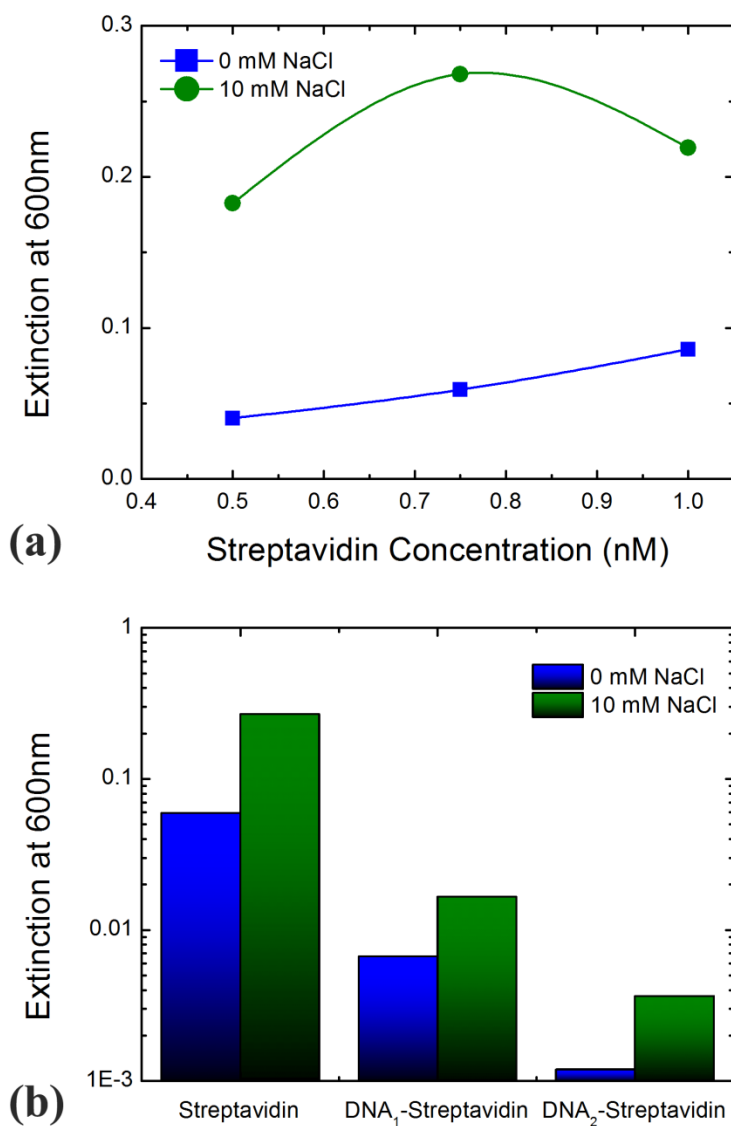
Figure 19 | Influence of Salt on DNA-Streptavidin-Nanoparticle Dimer Formation | (a) Comparison between 0 mM (blue line) and 10 mM (green line) NaCl for dimer formation with pure streptavidin. (b) The influence on dimer formation, shown for extinction at 600 nm, for 74mer DNA0-2–streptavidin for both 0 mM (blue) and 10 mM (green) of NaCl.

DNA-Programmed Assembly of Gold Nanoparticle Dimers

To assemble the dimers, the purified chromatographic fractions of formed DNA functionalized streptavidin linked nanoparticle dimers were mixed together with fractions containing complementary DNA strands according to a chosen assembly strategy.
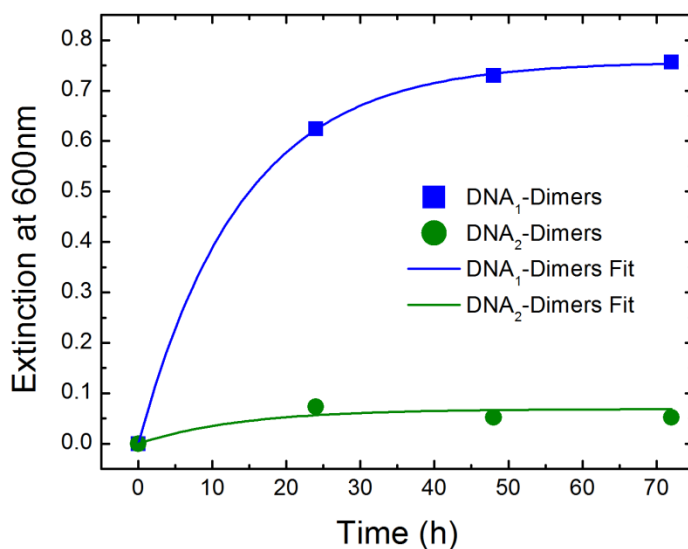
Figure 20 | DNA Functionalized Dimer Hybridization | Change in extinction at 600 nm for with respect to time after mixing 74mer DNA1-dimers (blue) and DNA2-dimers (green) with their complement strands.

Here, the fractions were mixed together at a one-to-one concentration ratio and the resulting increase of extinction at 600 nm can be seen in **Figure 20**, and a comparable change in scattering intensity is also observed (not shown here). These data both cofirms that hybridization is occurring in the sample, and that additional salt is required to hybradize species with larger repulsion, as seen for the much lower increase for DNA_2-dimers. The final results were confirmed by analyzing the samples with transmission electron microscopy and the micrograph from an assembly that should promote tetramers can be seen in **Figure 21a** and a less controlled sample promoting longer chains in **Figure 21b**. We note that all of the particles from the original pictures have been moved together to enable viewing at high magnification. These structures are potentially very interesting for, for example, the study of energy transfer processes by introduction of fluorophores through modification of the used DNA strands.
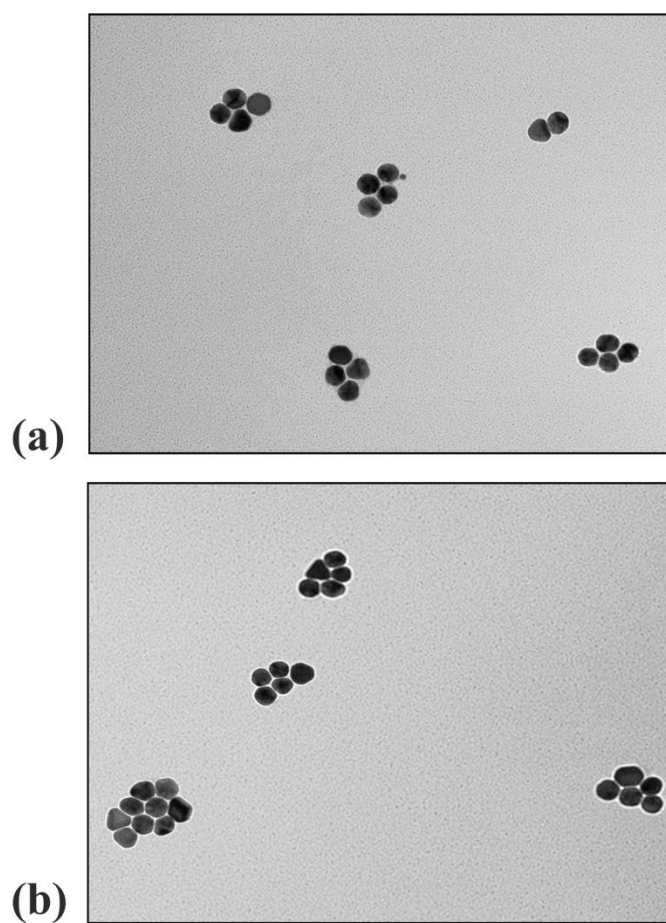
Figure 21 | TEM Micrographs of DNA-Programmed Nanoparticle Assembly | (a) Shows an assembly that should promote tetramers and (b) with a less controlled sample promoting longer chains. All of the particles from the original pictures have been moved together to enable viewing at high magnification.

6

In situ Photo-Induced DNA Capped Plasmonic Particles

In this last chapter, we develop a new protocol to synthesize silver nanoparticles in the presence of DNA under physiological conditions in a one-pot reaction by means of a photo-induced reaction where the DNA is left intact. Here, we study the nucleation of silver particles by photo-oxidation of excited Cy5 molecules attached to DNA strands, where the growth is supported by the presence of silver nitrate and tri-sodium citrate in the surrounding aqueous medium, and study the influence of the involved reacting agents on the resulting particles.

6.1 A New Protocol for Photo-Induced Nanoparticle Growth

In the present work we required an initial solution containing DNA, capping agents, and reactants, where growth of silver particles can be achieved without damaging individual components. We wanted a biologically friendly environment and therefore chose water as a solvent. Melting curves of DNA duplexes (Cy5-DNA48) of the 48-mer sequence and its complement, which were hybridized in 10 mM $NaNO_3$ solutions at room temperature under constant agitation for 2 hours, showed that they were stable from the freezing point up to ~45°C. These low temperatures made the well-known $AgNO_3$ / tri-sodium citrate system possible to use since $AgNO_3$ acts as a silver source and tri-sodium citrate will only act as a reducing agent at boiling temperatures but retains its function as a capping agent.[145,146] We note that the use of chloride salts was avoided to prevent the unwanted formation of silver chloride clusters, the low salinity was chosen to facilitate electrostatic repulsions between later-formed silver particles, thus enhancing the stability of the colloidal solution, and a constant concentration of 1 mM citrate was used to prevent flocculation processes, which were observed for free Cy5-A samples. To trigger the nucleation, we utilized the reactivity dyes exhibit, when exposed to light in their absorption wavelength. Cy5 was chosen as a sensitizer for the initial nucleation site upon excitation under laser irradiation,[58,61] due to that its absorption does not coincide with that of the other components. To make sure nucleation and growth of the silver particles were only induced in the presence of DNA strands, Cy5-labeled DNA was used.

Developing the Initial Protocol

Taking the previous statements into consideration and obtaining initial values from the literature, a crude protocol for the photo-induced formation of silver nanoparticles in solution was developed by evaluating the results from extinction spectroscopy, which can be seen in **Figure 22**.
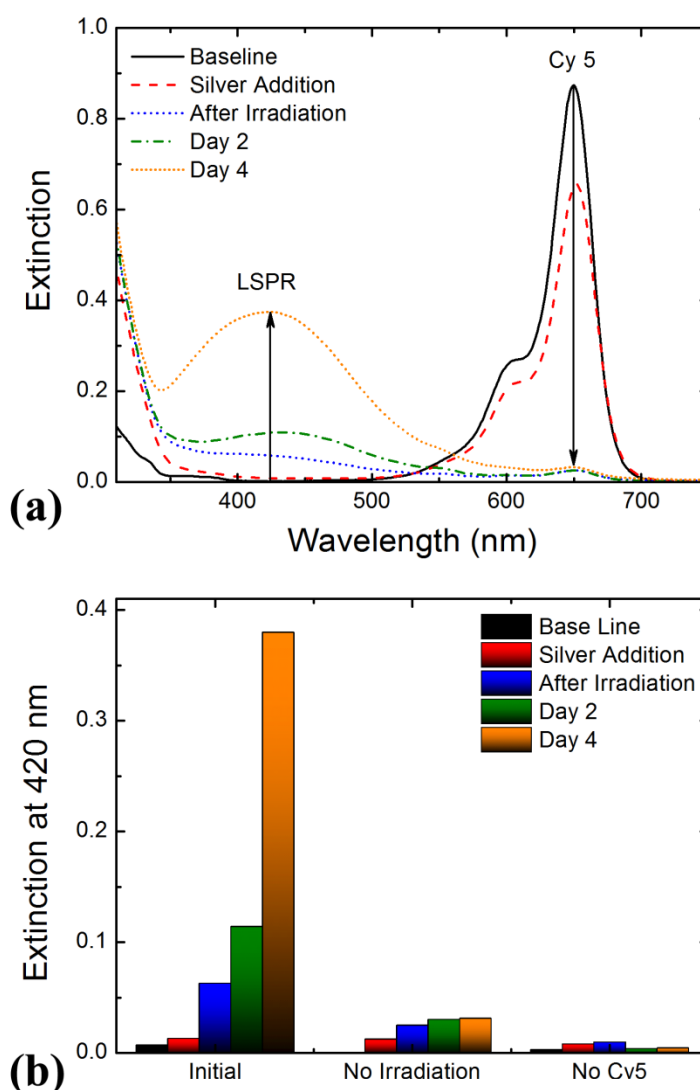
Figure 22 | Extinction Data: Photo-Bleaching of Cy5 and Development of LSPR Peak | (a) Extinction spectra show the photo-bleaching of Cy5 under laser irradiation and the localized surface plasmon resonance (LSPR) development over 4 days. Spectra were taken before irradiation (solid black), after addition of 1 mM AgNO$_3$ (dashed red), directly after irradiation for 1 hour with 647 nm light (short-dashed blue), 2 days after irradiation (dash-dotted green) and 4 days after irradiation (dotted orange). (b) The histogram shows the extinction at 420 nm (LSPR peak) for the initial data, shown in (a), a control sample in absence of irradiation and of another control sample without Cy5.

Here a solution, of 2 µM 48-mer hybridized DNA-Cy5 in 10 mM NaNO$_3$ was put into a UV-transparent 1 cm plastic cuvette (kept at 35°C) followed by 1 mM tri-sodium citrate and 1 mM AgNO$_3$ and was irradiated by intense 647 nm laser light (ca. 70 mW with a 650

± 10 nm band-pass filter). As a result the Cy5 absorption peak is photo-bleached, which can be seen as it decreases to <10% of its initial value. At the same time, we observe the occurrence of a signature localized surface plasmon resonance peak at ~420 nm, which continues to grow in magnitude over the following 4 days. Similarly, we observed the development of a localized surface plasmon resonance peak when irradiating solutions containing "free dye" (Cy5-A), single stranded DNA-Cy5, and shorter (24 nucleotides) single stranded DNA-Cy5.

Control experiments, performed in order to confirm photo-induced mechanism of silver nanoparticles nucleation gave proof that our system was working. In these measurements we kept all reaction conditions unchanged except for one. **Figure 22b** shows that a localized surface plasmon resonance peak, which indicates presence of metallic silver nanoparticles, does not develop without laser irradiation. The minor increase in absorption is most likely a result from the measurement procedure itself, as the sample was repeatedly exposed to red light in the UV-vis and dynamic light scattering instruments over the observation period of 4 days.[147] Furthermore, to confirm the role of Cy5 as the essential initiator for the photo-induced particle formation, we performed control experiments with samples that did not contain Cy5 by keeping all the other reaction conditions unchanged. Here, **Figure 22b** shows the evolution of extinction spectra and over a time period of 4 days, where there is no development of a characteristic localized surface plasmon resonance peak for silver nanoparticle.

The progression of particle growth can also be observed by measuring the change of intensity of scattered light through the sample, which is a useful complementary technique as its intensity related to the size and number of particles in solution. A direct comparison of the extinction spectra, from the localized surface plasmon resonance peak at 420 nm, and the intensity of scattered light over time can be seen in **Figure 23.** Here we compare a 'normal' sample, containing Cy5-DNA48, with one without Cy5. The first two data points represent extinction and scattering intensities before and after the addition of 1 mM AgNO₃. The signals are low, as expected for a colloid-free solution; the slight increase in the scattering intensity before irradiation results from a measurement artifact: during the light

scattering experiment the sample was illuminated with 632 nm light, which already resulted in the formation of some particles.[147] Upon irradiation with 647 nm light we observe a significant and rapid increase in both the extinction at 420 nm as well as the scattering intensity, which we attribute to the formation of silver nanoparticles, from the sample containing Cy5. Over a time period of two days, while the solutions were kept on a shaker protected from the ambient light, we observe a slow, yet steady increase of the extinction and scattering intensities. However, there was no significant increase in the recorded scattering intensities for the control, which confirms that particles did not form in the solution.
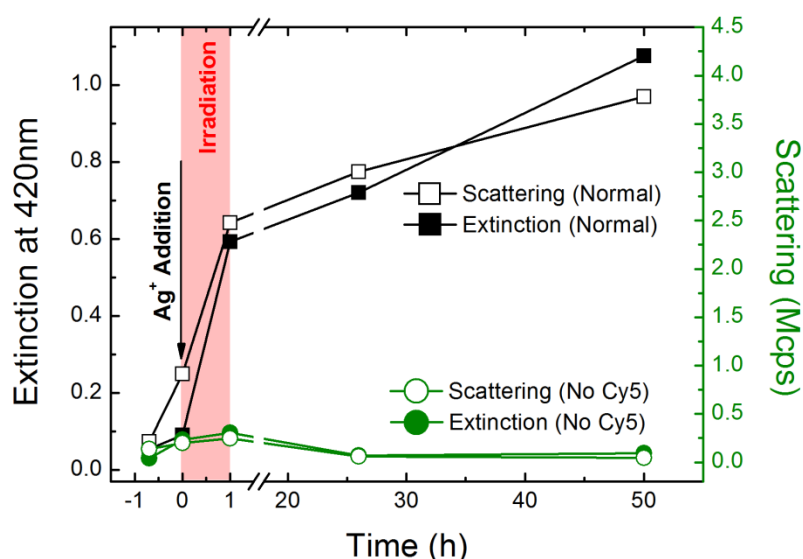

Figure 23 | Photo-Induced Nanoparticle Growth Kinetics | Development of the silver localized surface plasmon resonance peak (measured at 420 nm, open symbols) and the intensity of light scattered from the sample (full symbols) upon AgNO3 addition, irradiation and storage over two days. Note the axis break after the irradiation step. Normal corresponds to a sample prepared in accordance with the developed protocol while No Cy5 is a control sample without Cy5 dye.

From the collected data we presume that oxidation of Cy5 is responsible for the nucleation of small silver clusters and an irradiation induced plasmon-mediated mechanism gives rise to the remaining particle growth.[132–137,148] However, due to the small cross-section between the localized surface plasmon resonance, of the grown silver particles at about 420 nm, and

the irradiation wavelength at 647 nm the plasmon-mediated growth mechanism is slow.[137] Once the irradiation has ceased, the remaining particle growth is due to thermal-reduction of silver ions with citrate and DNA.[61,149] At these temperatures it is also a slow process, which is kept going because of the increased chemical reactivity at the surface due to the catalytic properties of the particles.[137]
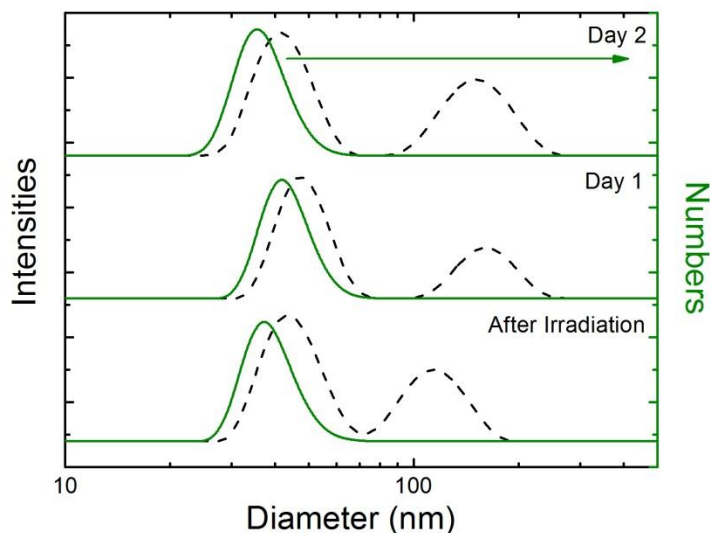

Figure 24 | Size Distributions of the Photo-Induced Grown Nanoparticles | Hydrodynamic diameters measured by dynamic light scattering: distributions are weighted by intensity (dashed black lines) and number (solid green lines).

As mentioned previously, particle sizes are inferred from dynamic light scattering data and shown in **Figure 24** for the Cy5-DNA48 sample. In the intensity weighted distributions (dashed black lines) two distinct ensembles of particles with diameters below and above 100 nm were identified. However, large particles contribute disproportionately high to scattering intensity $(I \sim d^6)$, which can be accounted for by a number-weighed distribution fit of the autocorrelation function. Accordingly, the number-weighed distribution shows only one ensemble of (small) particles with an average diameter of approximately 35 nm. It is remarkable that the size of the small particle ensemble does not vary significantly over time, merely the ensemble of larger particles increases in size. The

latter explains the steady increase in the plasmon peak and the total scattering intensity and most likely results from a coagulation of small particles to large agglomerates.

Dependence on Silver Concentration

The influence of the $AgNO_3$ concentration on extinction and scattering intensities at constant 1 mM tri-sodium citrate concentration, measured directly after the irradiation step, is shown in **Figure 25a**. We found an initial increase of the extinction and scattering intensities with $AgNO_3$ concentration, followed by a decrease for concentrations larger than 1 mM and 5 mM for extinction and scattering, respectively. The decrease indicates that large agglomerates are either breaking up or, most likely, the particles and/or agglomerates are precipitating out of the solution. The reactivity of $AgNO_3$ can be seen as a shift in peak positions. Here, the decrease of extinction intensity at 1 mM implies that precipitation has already started before the decrease in scattering intensity starts, allowing the average particle / aggregate size to still be increased by increasing the concentration of $AgNO_3$.

The effects of $AgNO_3$ concentration on particle size, inferred from dynamic light scattering, are plotted in **Figure 25b**. Here, it seems that there is a threshold concentration at around 0.1 mM, where there is insufficient silver to accommodate an adequately high speed of particle growth. However, in the concentration regime between 0.1 and 1 mM, stable colloidal solutions are formed, where number-weighed particle diameters of around 35 nm, and are found to be independent on silver concentration. The intensity-weighed distributions indicate the presence of an ensemble of larger particles, which, although vastly outnumbered by the 35 nm particles, becomes more abundant with increasing silver concentration. At concentrations above 5 mM the total intensity drops, while registering large amounts of agglomerates, supporting the statement that the particles are precipitating out of the solution.
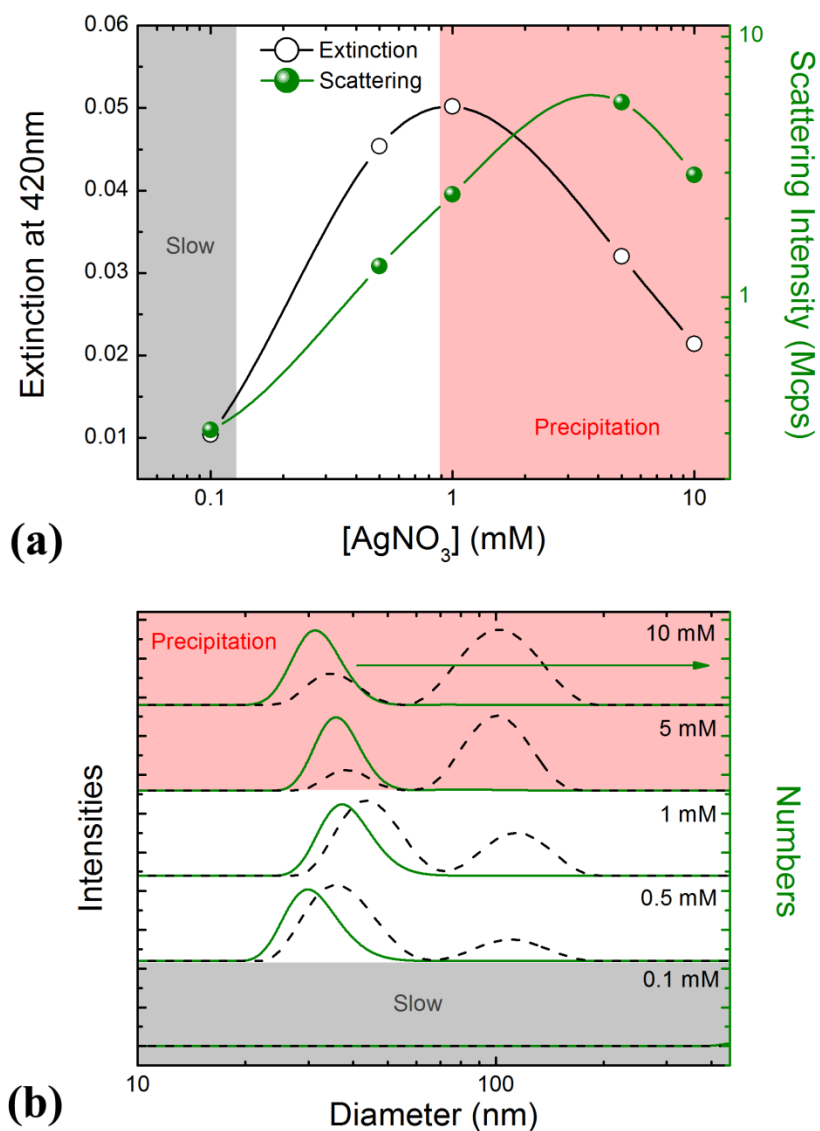
Figure 25 | Photo-Induced Particle Growth Dependence on Silver Concentration | (a) Dependence of the localized surface plasmon resonance extinction at 420 nm (open black symbols) and scattering intensity (full green symbols) on AgNO3 concentration immediately after irradiation. (b) Hydrodynamic diameter distributions by intensity (dashed black lines) and by number (solid green lines) for different AgNO3 concentrations recorded immediately after irradiation.

The AgNO3 concentration series was monitored over 4 days and the corresponding data for the extinction and scattering intensities as well as the size distribution information for the stable colloids follow the trends in **Figure 23** and **Figure 24**. Here the particle size

distributions weighed by number retain their diameter of approximately 35 nm. However, because the particles continue to slowly grow the boundary to precipitation moves to the left for longer storage times. Furthermore, particles do eventually 'appear' for concentrations around 0.1 mM, allowing the concentration window to remain as broad.

Dependence on Citrate Concentration

To study the function and influence of citrate ions has on the synthesis process we have performed similar measurements to those previously shown for $AgNO_3$, but now varying citrate concentration, while keeping amount of silver ions at a constant 1 mM concentration. The results for extinction and scattering intensities are depicted in **Figure 26a** and were collected immediately after irradiation. We found an initial increase of the extinction and scattering intensities with citrate concentration, followed by a decrease for concentrations larger than 3.5 mM. The decrease indicates that large agglomerates are either breaking up or, most likely, the particles and/or agglomerates are precipitating out of the solution. The role that citrate plays as a reducing agent is evident here, as an abundant concentration together with the volatility of $AgNO_3$ causes photo-induced growth speeds that are sufficient to create large enough particles and agglomerates to precipitate out of the solution.

The influence from citrate concentration on particle size, inferred from dynamic light scattering, is plotted in **Figure 26b**. Here, its influence as a capping / stabilization agent is evident for concentrations around 0.5 mM, where it no longer seems to be able to outweigh its role as a reducing agent and the particles precipitate from solution. However, in the concentration regime between 0.5 and 5 mM, stable colloidal solutions are formed, where number-weighted particle diameters of around 35 nm, and are found to be independent on citrate concentration. The intensity-weighed distributions indicate the presence of an ensemble of larger particles, which, although vastly outnumbered by the 35 nm particles, becomes more abundant with increasing citrate concentration. At concentrations above 5 mM the total intensity drops, while registering large amount of agglomerates, supporting the statement that the particles are precipitating out of the solution.
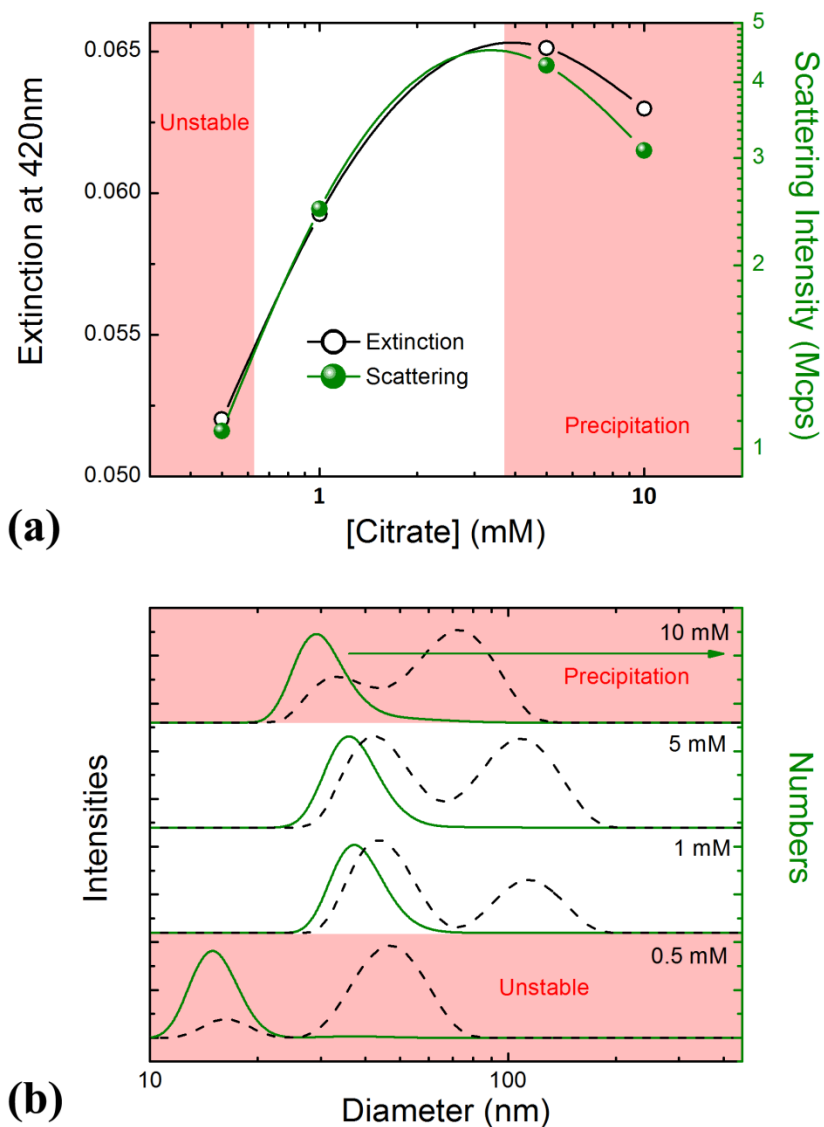
Figure 26 | Photo-Induced Particle Growth Dependence on Citrate Concentration | (a) Dependence of the localised surface plasmon resonance extinction at 420 nm (open black symbols) and scattering intensity (full green symbols) on tri-sodium citrate concentration immediately after irradiation. (b) Hydrodynamic diameter distributions by intensity (dashed black lines) and by number (solid green lines) for different tri-sodium citrate concentrations recorded immediately after irradiation.

The samples with different citrate concentrations have been monitored over 4 days and the corresponding data for the extinction and scattering intensities as well as the size distribution information for the stable colloids follow the trends marked out in **Figure 23**

and **Figure 24**. Here, the particle size distributions weighed by number retain their diameter of approximately 35 nm. However, because the particles continue to slowly grow, the boundary to precipitation moves to the left for longer storage times and, as expected, the system remains unstable for concentrations around 0.5 mM.

6.2 Mechanism for the Catalyzed Photo-Bleaching

In this section we present a more detailed analysis, of the extinction data presented in **Figure 22**, to find out if the photo-chemical reaction of Cy5-labeled DNA and $AgNO_3$ works as intended. Here, we make a kinetic study of the catalytic effect that silver ion concentration has on photo-bleaching rates of Cy5 fluorophores. In a biologically friendly environment the absorption and reemission of light from a fluorophore will exponentially decrease over time due to photo-chemical degradation. This photo-bleaching is associated with the transition from the fluorophores excited singlet state to the relatively long-lived and more chemically reactive excited triplet state. Therefore, it is possible to tell if the introduction of a reactive compound like $AgNO_3$ reacts with the dye by observing the bleaching rate as a function of its concentration.

The decrease of the absorption maximum of Cy5 at 650 nm was studied in dependence on the duration of laser irradiation and $AgNO_3$ concentration. The full spectra taken every 2 minutes for a Cy5-DNA48 sample containing 1 mM $AgNO_3$ is shown in **Figure 27a**. As expected, the spectral feature of the Cy5 extinction steadily decreases over irradiation time and the bleaching speed changes for different $AgNO_3$ concentrations as summarized in **Figure 27b**. Here, increasing concentration of Ag^+ ions leads to a higher photo-bleaching rate, suggesting that optically excited Cy5 molecules (Cy5*) undergo a chemical reaction with Ag^+ ions. Most likely, charge transfer results in the oxidation of Cy5* to $Cy5^{ox}$, while Ag^+ ions are reduced and form a metal silver seed which subsequently serves as a nucleation site for further particle growth and is similar to the reported silver nanowire formation mechanism.[61]
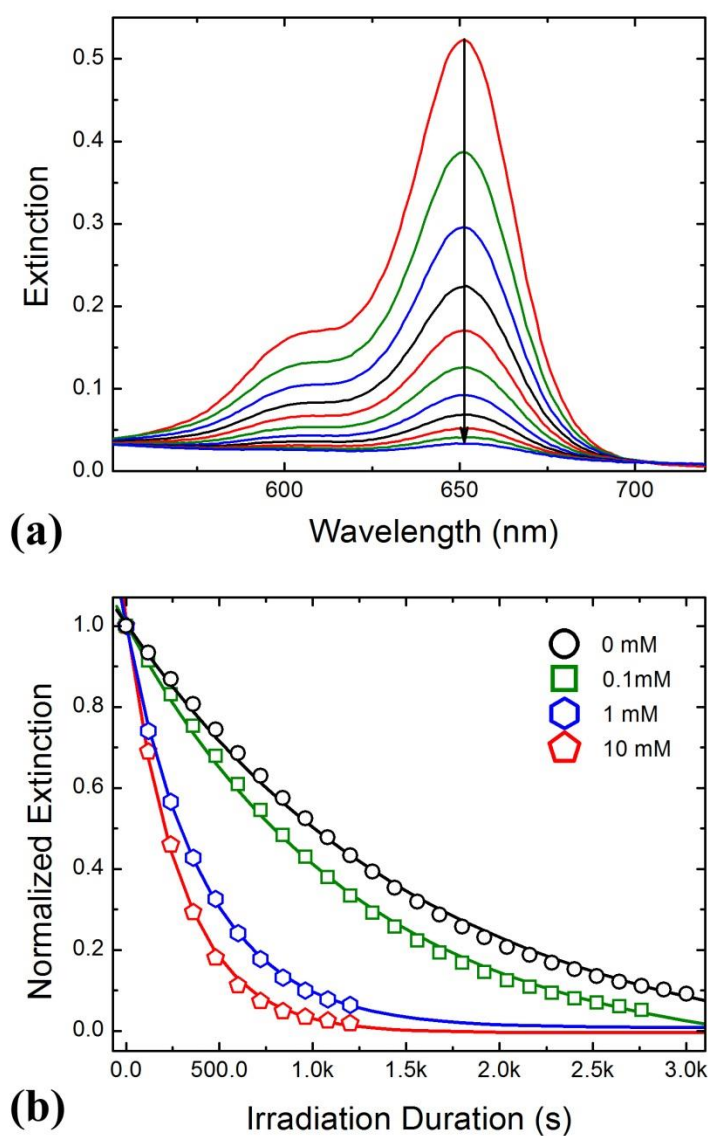
Figure 27 | Catalyzed Photo-Bleaching of the DNA-Cy5 Complex | (a) Time course of Cy5 photo-bleaching with irradiation time in a Cy5-DNA48 sample containing 1 mM AgNO₃. Spectra were recorded every 2 minutes. (b) Bleaching curves for different AgNO₃ concentrations as stated in the legend. Solid lines are single exponential fits in accordance with the developed model.

Moreover, formation of heterodimers between the dye and Ag^+, which can be detected from the red-shifted absorption spectrum of the Cy5 peak after addition of AgNO₃ (see **Figure 22a**), and their reduction potentials of 0.8 V for silver and –0.84 V for Cy5 support our

assumption about photo-induced electron transfer.[150] Therefore, we can approximate the process with a simplified chemical reaction as

$$Cy5^* + Ag^+ \rightarrow Cy5^{ox} + Ag^0. \qquad (3)$$
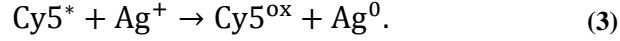
This mechanism has also recently been proposed for the photo-induced growth of silver nanowires in nano-tubular templates.[61] Additionally, after the initial formation of the complexes between Cy5 and silver ions (**Figure 22a**) further nucleation and growth of the silver particles continues due to prudent, under the given conditions, electron donor behavior of the surrounding medium, which in addition to the dye contains citrate ions, DNA[40] and water:

$$(Ag^0)_n + Ag^+ + \underbrace{e^-}_{Cy5\,/\,DNA\,/\,citrate\,/\,H_2O} \rightarrow (Ag^0)_{n+1} \qquad (4)$$
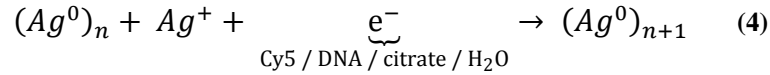
To get a better insight into the influence of the silver ions on the photo-degradation rate of Cy5 in this particular system we separated and then analyzed the response of silver from the remaining concomitant effects with the following kinetics equations:

$$\frac{\mathrm{d}N^*}{\mathrm{d}t} = k_{ph}IN - k_{Ag}c_{Ag}N^* - kN^*, \qquad (5)$$

$$\frac{\mathrm{d}N}{\mathrm{d}t} = -k_{ph}IN + k'N^*. \qquad (6)$$

Here N and N^* are concentrations of the dye molecules in the ground D and excited D^* states, c_{Ag} is concentration of Ag^+ in solution, I is the laser radiation intensity, and k_{ph} is a photo-excitation constant of the reaction $D \rightarrow D^*$. Constant $k = k' + k''$ characterizes lifetime of the dye in the excited (triplet) state in absence of a catalyst, where k' is a de-excitation constant of the reaction $D^* \rightarrow D$ and k'' is a dye intrinsic photo-degradation

constant, and k_{Ag} is a dye photo-degradation constant in presence of catalyst and describes the reaction (3) in the studied process. The presented considerations are based on an assumption that the photo-degradation of the dye (oxidation) occurs from the excited state.

By summing equations (5) and (6) up we obtain the following formula to describe the studied system

$$\frac{\mathrm{d}}{\mathrm{d}t}(N + N^*) = -\left(k'' + k_{Ag}c_{Ag}\right)N^*. \qquad \textbf{(7)}$$

From this equation we can see that concentration of the non-oxidized Cy5 molecules linearly depends on the concentration of silver ions in solution and therefore bleaching rate of the Cy5-labelled molecules in our reaction in presence of catalyzing silver ions can be approximated by the relation

$$N(t) \sim \exp\left[-\left(k_0 + k_{Ag}c_{Ag}\right)t\right], \qquad \textbf{(8)}$$

where we have put $k'' \equiv k_0$.

Throughout the derivation we consider N to be proportional to the concentration of Cy5 molecules in the solution. From Eq. (8) we can conclude that number of intact Cy5 molecules N, decreases due to an intrinsic photo-bleaching process represented by the rate constant k_0, and a photo-catalyzed reaction with silver, which depends on the concentration of Ag$^+$ ions c_{Ag}, and the reaction rate k_{Ag}. From the measurement without silver we obtain the intrinsic photo-bleaching rate constant for the used illumination conditions to be $k_0 = 6.25 \cdot 10^{-4}$ s^{-1}. Analysis of the measurements with added silver nitrate yields the molar rate constant $k_{Ag} = 1.7$ M^{-1} s^{-1}. The calculated constants have been used to fit the experimentally obtained curves in **Figure 27b**. We should note that linear dependence on the silver concentration was found to hold for $c_{Ag} < 10$ mM and for Cy5-labelled DNA concentrations in the micro-molar range. Additionally, silver-catalyzed photo-bleaching

exceeds the intrinsic photo-bleaching process only when the silver concentrations are greater than approximately 0.1 mM. It should be noted that obtained photo-bleaching constants have been derived from the experimental data where DNA-Cy5 has been used. Therefore, exploited silver concentrations that interact with the dye are effectively smaller, since oligonucleotides are known to act as ion scavengers for strong metals as for example silver,[151] and experimental data for free dye should result in higher rate constants.

6.3 Characterization of the DNA Capped Plasmonic Particles

Given that DNA is present on the nanoparticle surface, the question arises how this association occurs during the nanoparticle growth. Two processes appear possible: (i) after photo-oxidation of Cy5 and creation of a Ag_4^+ cluster,[152] the seed remains linked to the original Cy5 location at one end of the DNA strand. In this case, the DNA strand is (partly) incorporated into the growing nanoparticle and, possibly, serves as a template for the directed growth of the silver crystal along the strand; (ii) alternatively, the silver clusters diffuse away from the site of reduction. In this case, nanoparticles grow autonomously in solution at first, until at a later stage DNA adsorbs onto the nanoparticle, terminating the nanoparticles growth.[153]

Extinction Characterization of the Grown Particles after Centrifugation

To shed light on the role of DNA during the nanoparticle growth, we conducted extinction measurements, where we included into examination the signature DNA absorption band at 260 nm with a complementary comparison of the hydrodynamic particle diameter from dynamic light scattering with the core diameter from transmission electron microscopy examination. For this we compared three samples:

   I.   Photo-induced sample from Cy5-DNA48

  II.   Commercially obtained 20 nm silver particles with unlabeled 48-mer DNA

 III.   Photo-induced sample from free Cy5-A and unlabeled 48-mer DNA

Firstly, we evaluated the extinction spectra of all three samples. In order to exclude contributions from leftover DNA freely dissolved in solution, comparative measurements were made between the samples before and after centrifugation purification.
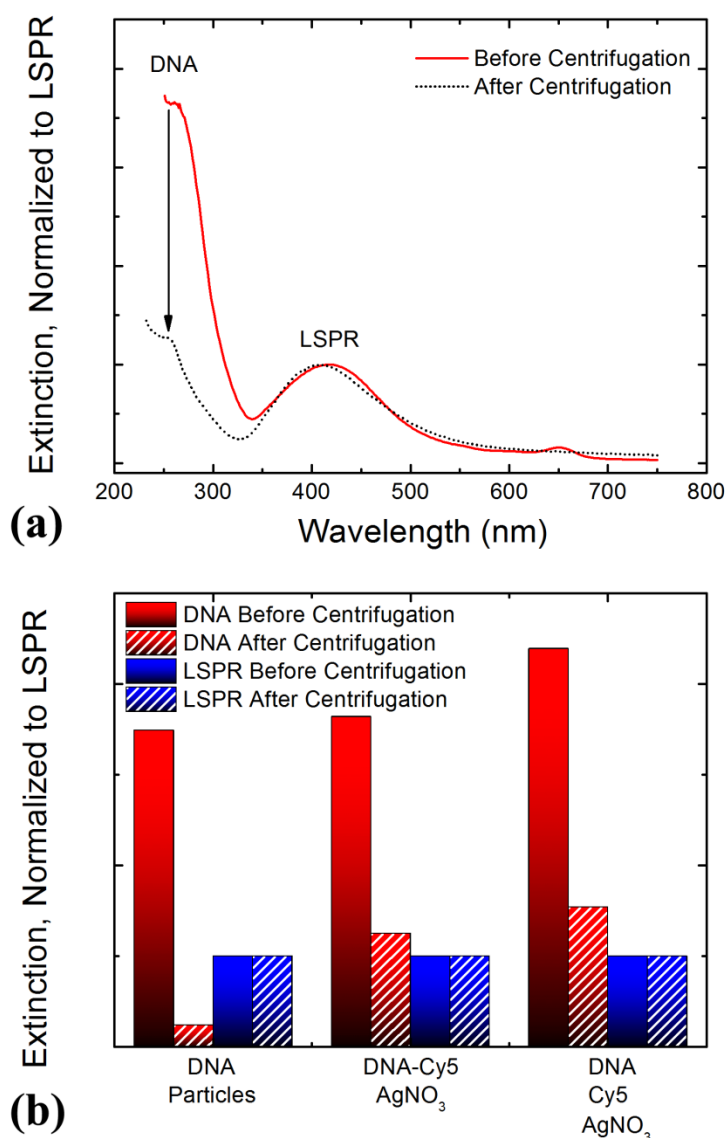
Figure 28 | Centrifugation Measurements | (a) Extinction spectra, normalized to the localized surface plasmon resonance (LSPR) maxima, of the solution that contains photo-induced metallized 2 μM Cy5-DNA48 before centrifugation (solid red curves) and re-dispersed precipitates after centrifugation (dotted black curves). (b) Relative peak magnitudes of a reference sample, which is a mixture of 1 nM commercially obtained 20 nm silver particles and unlabelled 2 μM 48-mer DNA, photo-induced metallized 2 μM 48-mer DNA-Cy5, and photo-induced metallized 2 μM Cy5-A in the presence of unlabelled 2 μM 48-mer DNA.

The results for the photo-induced sample from Cy5-DNA48 can be seen in **Figure 28a**. Prior to centrifugation, the presence of DNA and nanoparticles in the mixture can clearly be identified and quantified from extinction spectrum (solid red curves). After

centrifugation (20 minutes at 14.5 krpm), the supernatant was removed and the extinction of the re-dissolved precipitate containing the pulled-down nanoparticles was measured again (dotted black curve). Such cleaning procedures are not lossless, and the centrifuged products suspension in 1 mM sodium citrate showed a loss in scattering intensity and a shift of size distribution weighed by number towards smaller average particle sizes (not shown here). These results can also be seen in the extinction spectra. In **Figure 28a** the loss in extinction for the localized surface plasmon resonance was compensated for by normalization, but the peak shift towards shorter wavelengths for the centrifuged product is representative of the smaller particle sizes. We note that there will also be a shift, where the localized surface plasmon resonance peak will be especially sensitive, which results from changes in the dielectric constant of the solution when what is left of the 1 mM $AgNO_3$, 10 mM $NaNO_3$, 1 mM tri-sodium citrate and 2 µM Cy5-DNA48 solution is exchanged for 1 mM citrate. However, it will be small in comparison to the shift due to the change in particle ensemble size distribution. Furthermore, the DNA absorption peak blue shifts from 280 nm to 260 nm after the removal of freely dissolved DNA. The pre-centrifuged peak position at 280 nm can be attributed to the binding of Ag^+ ions to DNA bases, which has been reported to shift the peak towards lower energies in the absorption spectra.[154] The fact that after centrifugation the 'normal' 260 nm peak position is retained indicates that the nanoparticle bound DNA molecules do not contain Ag^+ ions.

Reference measurements can be seen on either side of the data from the Cy5-DNA48 sample in **Figure 28b**. The left columns represents the commercially obtained 20 nm silver particles with unlabeled 48-mer DNA. This sample was prepared by mixing 1 nM commercially obtained 20 nm silver nanoparticles (characterized by transmission electron microscopy) with 2 µM unlabeled 48-mer DNA. As the colloids are capped by a citrate shell, a significant interaction of the DNA with the particles is not expected for short incubation times. Before centrifugation, the presence of DNA (red whole columns) and nanoparticles (blue whole columns) in the mixture can clearly be identified and quantified. After centrifugation (20 minutes at 14000 *g*), the supernatant was removed and the extinction of the re-dissolved precipitate containing the pulled-down colloids was measured again (partial columns). Here it was shown that, the post centrifugation spectrum exactly

matches that of the sample containing silver nanoparticles before addition of the unlabeled 48-mer DNA. So the remaining extinction below 300 nm stems from nanoparticle inter-band transitions and not from residual DNA. In contrast, the Cy5-DNA48 and the free Cy5-A with unlabeled 48-mer DNA samples retain a strong indication that DNA is still present after centrifugation, which would mean that some of the DNA is inseparably associated with the colloids.

The extinction spectra also reveal an extremely high DNA absorption intensity. As expected, the magnitude of the localized surface plasmon resonance corresponds to a nanoparticle concentration in the nano-molar range, while the post-centrifuged DNA concentration appears to be in the micro-molar concentration range. This would imply the geometrically unlikely scenario of a single nanoparticle being covered with a thousand 48-mer DNA strands. A plausible explanation for this is that since the extinction peak created by the inter-band transitions of the metallic silver nanoparticles, which overlap with the extinction peak of DNA, changes with size and shape of the particles, its correlation with the commercial particles introduces an error. The impact of which will be minimized from the enhancement effect DNA has when absorbed on the particles surface, caused by the resonance of the DNA absorption band with inter-band transitions of the metallic silver nanoparticle.[155] Here, the high impact DNA has on particle growth prohibits a valid reference. So, to confirm our findings a comparison between the hydrodynamic particle diameters from dynamic light scattering with the core diameters from transmission electron microscopy is needed.

Transmission Electron Microscopy Characterization of the Grown Particles

To investigate the size and structure of the nanoparticles grown on Cy5-modified DNA templates further, we imaged the particles using transmission electron microscopy. The primary goal here was to find out more about how DNA is capping the particles by comparing the transmission electron microscopy determined nanoparticle core sizes to that of the hydrodynamic particle sizes inferred by dynamic light scattering.
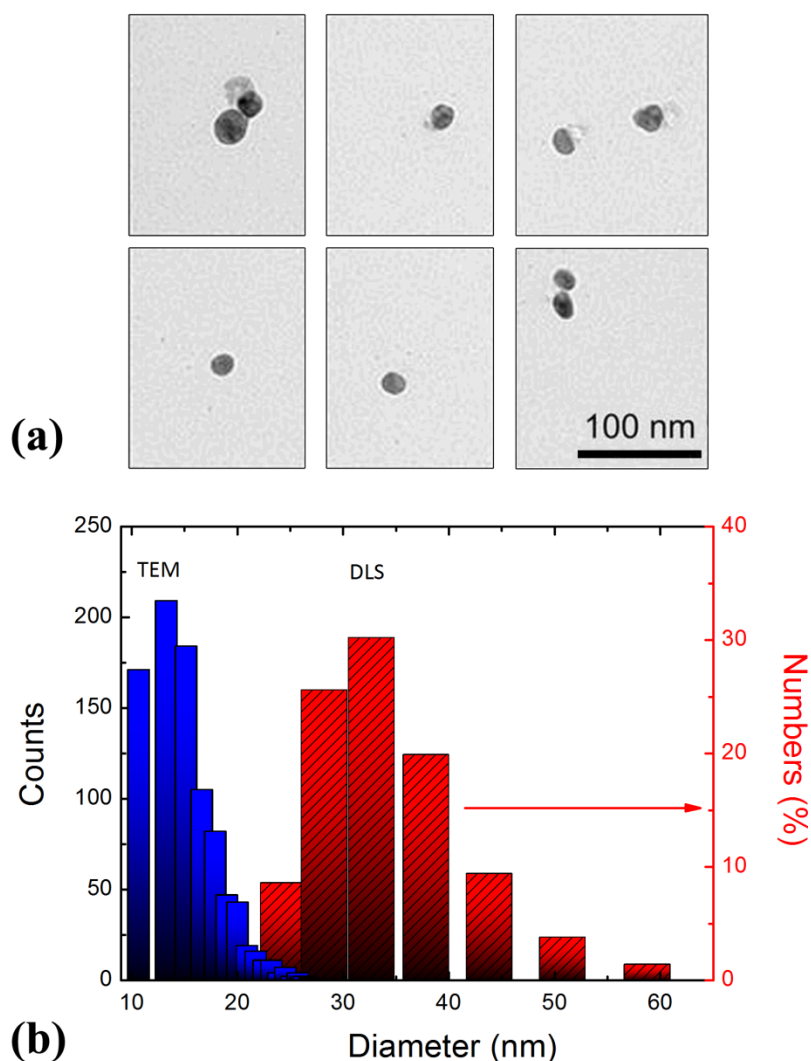
Figure 29 | Nanoparticles Metal Core Size Characterization by TEM | (a) Exemplary transmission electron microscopy images of nanoparticles grown by the photo-induced method. (b) Size distribution of particles grown in a 1 mM AgNO$_3$ solution analyzed by transmission electron microscopy (TEM) (solid blue bars) and dynamic light scattering (DLS) (dashed red bars).

Particles prepared from the 48-mer DNA-Cy5 sample are shown in **Figure 29a** and are mostly spherical in shape with a proportion of the population exhibiting a triangular distortion commonly found for silver nanoparticles grown at low pH.[156] We note that while the silver nanoparticles appear as darker shapes, smudges with a light contrast stem from salt formed during the drying process. Here, the particles shape makes it highly unlikely

that DNA strands are (partly) incorporated inside, as the DNA template would have directed growth of the silver crystal along the strand forming more elongated particles. These results favor the second process described in the beginning of this section where DNA adsorbs onto the nanoparticle acting as a capping agent.

To show this, statistical data of approximately 900 particles per sample were analyzed with respect to their diameter (using the software ImageJ). The results for one sample are plotted in **Figure 29b** together with the particle size distribution, from the same sample, derived from dynamic light scattering. Here, transmission electron microscopy data predicts a highest frequency diameter of approximately 15 nm in comparison to a significantly larger average diameter of 35 nm from dynamic light scattering. In comparison, the 16 nm length of a 48-mer DNA strand together with the transmission electron microscopy core diameter gives a particle size of 47 nm. This implies that the stands could be free-standing on the surface, since the organic system will not scatter light very efficiently leading scattering data to predict smaller particle sizes. Furthermore, transmission electron microscopy and dynamic light scattering measurements of the commercial citrate capped silver nanoparticles gave a unanimous size of 20 nm, in accordance with the manufacturer's information. This, together with that free DNA in the Cy5-A with unlabeled 48-mer DNA sample will also act as a capping agent (**Figure 28b**) confirms the suggested growth mode takes place. That is, DNA takes the role of capping agent which adsorbs onto the nanoparticle surface during growth. The proposed capping action of DNA is also consistent with the observation, that the nanoparticle solutions were stable in the presence of DNA, while nanoparticles grown from free dye (without DNA) required the addition of citrate to prevent the precipitation of colloids.

7

Conclusions and Outlook

In this chapter, I provide a summary and outlook of the results that have been presented in this thesis, covering our investigations into creating predetermined metallic nanostructures for future studies of plasmonic interactions between single-particles. Here, the original questions that this work is based on will be restated, followed by a summary of our findings, conclusions and short outlook.

Would a higher number of thiol-groups in a linker molecule be advantageous when functionalizing nanoparticles with DNA?

In conclusion, we have investigated the use of DNA modified with di-thiol-phosphoramidite (DTPA), a linker bearing four sulfhydryl-groups, to functionalize gold nanoparticles. It is well established that using citrate as a capping agent, like the commercial nanoparticles used for this work were delivered with, does not provide them with sufficient negative charge for good colloidal electrostatic stability. For many applications ligand exchange to BSPP is necessary to increase the negative surface charge for successful results. In our work, this involved ligand exchange with the goal of replacing the smallest possible amounts of BSPP with DNA-DTPA followed by and additional ligand exchange, to allow for good separation by the charge exhibited from the bound DNA, where BSPP was changed for mPEG-thiol since it is more neutral and will not remove the DNA-DTPA. However, using BSPP resulted in many unwanted effects during purification. Here, the chromatogram showed that the ligand exchange of BSPP for mPEG-thiol is unfavorable because elution showed that BSPP and even DNA-DTPA peaks were present and most importantly very bad separation occurred between different numbers of DNA strands bound to the particles due to the varying amount of BSPP still associated with the particles which distributes the charge. While it was possible to remove any measurable sign of BSPP, this can only be achieved by adding numerous ligand exchanges and cleaning steps, making it less cumbersome to deal with a lower colloidal electrostatic stability by bypassing the use of BSPP entirely. In our new protocol, ligand exchange was performed with the goal of replacing the smallest possible amounts of citrate with DNA–DTPA, followed by and additional ligand exchange, to allow for good separation by the charge exhibited from the bound DNA, where the remaining citrate was changed for mPEG-thiol since it is more neutral and will not remove the DNA-DTPA. This direction showed successful results with large separation for very few steps which simplified this method extensively. In the optimized protocol a much lower DNA to nanoparticle concentration ratio of 4:1 in comparison to 130:1 for thiol-DNA was needed, showing that DTPA-modified DNA can be successfully used for gold nanoparticle functionalization due to the higher chemisorption efficiency of the linker's four sulfhydryl-groups to the gold surface of the nanoparticles. In

addition, the mPEG-thiol molecules proved to be a reliable capping agent to complement the DNA-DTPA molecules as the obtained conjugates have shown to be stable under long storage and during purification.

In outlook, the isolated conjugates can be used for a variety of interesting experiments. For instance, by preparing mono-conjugates with complementary strands, the formation of dimers with tunable inter-particle spacing would be possible, and di-conjugates could be used for longer chain structures. Such assemblies would be very interesting for, for example, energy transfer studies.

Can anion-exchange high pressure liquid chromatography become a viable alternative and improvement for existing techniques to reproducibly obtain high yields of nanoparticles with a predefined number of short DNA strands attached?

In conclusion, anion-exchange high pressure liquid chromatography was evaluated as a separation technique, where the development of compatible synthesis protocols is an integrate part. Separation of conjugates formed from the DNA-DTPA protocol described above, make this point abundantly clear. Here, a Dionex DNAPac Pa-100 anion-exchange column, which separates species by passing them around 13 μm, nonporous, polymeric resin with bound 100 nm positively charged quaternary amine-functionalized latex particles on their surface, was only able to elute 1 % of the particles when BSPP was present. Furthermore, the particles would not fully elute when trying to recover the column, which means it was being irriversibly damaged, but did perform stably when the protocol without BSPP was used, albeit with bad separation without damaging the column. However, an investigation into the interactions of nanoparticles with packaging materials of anion-exchange columns showed that replacing it with an YMC-BioPro QA anion-exchange column, which is packed with 5 μm, hydrophilic polymer beads with 100 nm pores containing $CH_2N^+(CH_3)_3$, would give successful results. Indeed, the elution efficiencies for the protocol without BSPP changed from 1% to over 90% with no immediate sign of column damage during recovery. The high yield and reproducibility shows that anion-exchange high pressure liquid chromatography can be used as a standard method to obtain

DNA-nanoparticle conjugates that promotes not only strong electrostatic interaction to separate the species but also high elution rate for the mechanically rigid gold nanoparticles.

In outlook, this method was previously only a proof of concept, which caused irreparable damage to the column making it undesirable. However, our work provides the proof that it can be used on a much larger scale, even as an essential tool for nanoparticle separation by charge.

Can nanoparticles be functionalized with thiol-biotin-streptavidin bound to specific numbers biotin-functionalized DNA strands?

In conclusion, we have developed a new way to functionalize gold nanoparticles with DNA molecules by utilizing the streptavidin-biotin binding properties. Here, we functionalized gold nanoparticles with disulfide-PEG-biotin and mix them with an even distribution of all four DNA-biotin-streptavidin conjugates. This solution, which contains a diverse population of DNA-nanoparticle conjugates, was then separated with anion-exchange high pressure liquid chromatography and the fractions collected. The chromatogram showed successful separation of the different conjugates.

In outlook, the isolated conjugates can be used for a variety of interesting experiments. For instance, by separating mono-conjugates with complementary strands, the formation of dimers with tunable inter-particle spacing would be possible, and di-conjugates could be used for longer chain structures. Such assemblies would be very interesting to study plasmon-transport and plasmon-enhanced phenomena in solution ensembles and at a single particle level.[109]

What does the conformation that bound streptavidin with and without DNA have to a nanoparticle?

In conclusion, the previously mentioned chromatogram showed the number of attached streptavidin proteins or DNA-streptavidin conjugates to the nanoparticles surface by means of anion exchange chromatography. Here, the usage of the free streptavidin was evidenced through four convoluted peaks corresponding to streptavidin-nanoparticle conjugates. That

these peaks correspond to streptavidin-nanoparticles was nicely demonstrated by their equidistance and a larger gap from the unconjugated particle peak. Interestingly, this separation implies that the protocol allows for a maximum of four streptavidin to one nanoparticle and the similar deconvoluted peak areas suggests that charge repulsion plays a large role. This would increase the binding symmetry of streptavidin around the particle and considering that the protein has a diameter of 5 nm, in comparison to the nanoparticles 20 nm diameter, and also supports four fold binding symmetry, this is a very nice result. The data corresponding to the elution of the different DNA-streptavidin conjugates show that only small amounts of free streptavidin holding one and two DNA stands in solution remain. The similar peak height of streptavidin holding four DNA stands, which cannot react, to that of streptavidin holding three DNA strands, implies that they are also unreacted. This, together with the two, possible three peaks, corresponding to the DNA-nanoparticle conjugates indicated that the charge repulsion is too high to allow more than three DNA strands to a particle with a maximum of two DNA strands to one streptavidin.

In outlook, these newly found symmetries can be very useful for future assembly of complex nanoparticle structures.

Is it is possible to gain a high enough control over the interlinking process of biotin-functionalized particles and streptavidin, to obtain high yields of small particle complexes and additionally enrich them under physiological conditions through size exclusion chromatography?

In conclusion, we have studied streptavidin-induced interlinking process of biotin-functionalized 20 nm gold nanoparticles. Here, we performed an analysis to find the optimum concentration ratio between nanoparticle and streptavidin concentration and the data show aggregation regions that allow for controllably obtaining small particle complexes. Unsaturated complexes that are stable in solution at low salt concentrations formed within minutes and occurred for [nanoparticle]:[streptavidin] concentration ratios smaller than [1]:[2] with an optimum formation concentration for dimers at [1]:[0.7], just over the stoichiometric ratio due to dilution. Size analysis evidenced that the majority, up

to 20%, of the small stable aggregates at [1]:[0.7] were dimers and the fraction of small particle complexes of interest can be enriched by means of size exclusion chromatography and gradient centrifugation under physiological conditions.

In outlook, in contrast to previous reports where this kind of process was used for uncontrolled agglomeration, this protocol can be very useful for controlled assembly of complex nanoparticle structures.

Can high concentrations of streptavidin hinder aggregation through saturation of the binding sites?

In conclusion, we have studied streptavidin-induced interlinking process of biotin-functionalized 20 nm gold nanoparticles. Here, we performed an analysis to find the optimum concentration ratio between nanoparticle and streptavidin concentration and the data show aggregation regions that allow for controllably obtaining small particle complexes. Streptavidin-saturated complexes that are stable in solution at low salt concentrations were formed between 11 to 50 fold higher streptavidin to nanoparticle concentrations. The high streptavidin concentration was capable of blocking the formation of unstably large aggregates due to the limited amount of remaining unoccupied binding sites, and the aggregation size therefore decrease for increasing concentrations until only completely pacified individual particles remained. We found that this region is also difficult to quantify, since it is most likely very dependent on reaction and diffusion limited kinetics where the outcome can be altered by, for example, titrating the biotin-nanoparticles into streptavidin or vice versa. The first indication of this comes from that the saturation and capping of the particles takes place at 50 fold higher streptavidin concentrations than nanoparticles, which also coincidently corresponds to the number of proteins that would geometrically fit onto a particles surface. However, the number of bound proteins is limited due to mutual repulsion of the species,[143] and while increasing the salt concentration to 10 mM does little to change the unsaturated region, it offsets the saturated region to higher concentrations where it is significantly broadened, ending at 1000 fold higher streptavidin concentrations than nanoparticles for complete passivation.

In outlook, in contrast to previous reports where this kind of process was used for uncontrolled agglomeration, the method of obtaining saturated, together with the previous unsaturated, small stable nanoparticle complexes adds an extra degree of control and therefore can be very useful for assembly of complex nanoparticle structures.

Is there a way to organize particles on the nano-scale by combining DNA functionalized streptavidin-induced nanoparticle-dimers into complex structures?

In conclusion, we investigated combining the previously described topics in a new way to obtain high order structures. Since it is not possible to bind biotin-DNA in-between two streptavidin bound particles, the dimer must be formed with streptavidin which is already occupied by biotin-DNA. According to our previous results, the nanoparticles will be functionalized with a combination of 1 to 4 streptavidin proteins each holding 0 to 2 DNA strands, but not more than three total strands to a particle, only the fractions containing streptavidin with one and two DNA strands were collected. Here, we balanced the reaction to produce an even distribution of all four conjugates and then separated them by the number of DNA strands associated with one streptavidin using anion-exchange high pressure liquid chromatography. From these fractions either particles with 1 to 3 DNA_1-streptavidin conjugates and 0 to 1 DNA_1-streptavidin with one DNA_2-streptavidin, where the DNA strands are initially pointing outwards from the surface were formed. Increasing the salt concentration allowed dimers to form with one or two DNA strands connected to the dimers symmetrical rotational axis. Due to the amount of different species created, the DNA functionalized nanoparticle monomers and dimers were purified and the separated fractions collected from anion-exchange and size exclusion chromatography. At this point, by exploiting Watson-Crick base pairing of DNA, tetramers can be created by introducing either the DTPA DNA_1-nanoparticles or the separated DNA_1-streptavidin nanoparticle monomers with the complementary strand terminating the structures, or alternatively, longer chains could be formed by introducing DNA functionalized dimers with the complement strand.

In outlook, these built structures can potentially become useful well-defined substrates for surface-enhanced techniques and energy transfer studies. Furthermore, introducing dimers with different DNA strands could be used to create longer controlled chain structures.

Can silver nanoparticles be grown in the presence of DNA under physiological conditions in a one-pot reaction by means of a photo-induced reaction where the DNA is left intact?

In conclusion, based on the gained experience during work with the colloidal systems, we have developed a one-pot photo-induced nanoparticle synthesis procedure in the presence of DNA oligonucleotides in aqueous solution. Photo-excited Cy5 dyes act as nucleation sites for silver clusters upon irradiation with 647 nm light. The colloids, formed during the irradiation process, are mostly spherical in shape, exhibit a typical localized surface plasmon peak, and size-independent on the precursor silver ions concentration for the studied below 10 mM range. The nanoparticles feature a metallic core of 15 nm diameter, yet a significantly larger hydrodynamic diameter of approximately 35 nm, which is attributed to the presence of DNA on the nanoparticle surface in free-standing confirmation allowing their potential further organization. Growth and separation experiments under different conditions indicate that DNA irreversibly adsorbs onto the nanoparticles during their growth and presumably acts as a capping agent. Interestingly, the nucleotides exhibit an extraordinarily strong optical absorption, which is ascribed to the surface enhancement effects.[115–117] These DNA-capped silver nanoparticles exhibit robust association of the DNA to their surface that could not be removed by ligand exchange reactions.

In outlook, this work is of particular advantage since there is a shortage of methods to obtain silver nanoparticle conjugates with DNA. The obtained species are therefore of high interest for nano-scale plasmonic studies due to the remarkable properties of the metal and potential provided by the DNA molecules for further modification and organization.

8

List of Figures

9

References

1. Kumar, C. S. S. R. *Metallic Nanomaterials*. (Wiley: Weinheim, 2009).

2. Sperling, R. A., Rivera Gil, P., Zhang, F., Zanella, M. & Parak, W. J. "Biological Applications of Gold Nanoparticles". *Chem. Soc. Rev.* **37**, 1896–1908 (2008).

3. Boisselier, E. & Astruc, D. "Gold Nanoparticles in Nanomedicine: Preparations, Imaging, Diagnostics, Therapies and Toxicity". *Chem. Soc. Rev.* **38**, 1759–1782 (2009).

4. Hutter, E. & Fendler, J. H. "Exploitation of Localized Surface Plasmon Resonance". *Adv. Mater.* **16**, 1685–1706 (2004).

5. Kreibig, U. & Vollmer, M. *Optical Properties of Metal Clusters*. (Springer-Verlag: Berlin Heidelberg, 1995).

6. Bohren, C. F. & Huffman, D. R. *Absorption and Scattering of Light by Small Particles*. 539 (Wiley: New York, 1983).

7.   Murray, C. B., Kagan, C. R. & Bawendi, M. G. "Synthesis and Characterization of Monodisperse Nanocrystals and Close-Packed Nanocrystal Assemblies". *Annu. Rev. Mater Sci.* **30**, 545–610 (2000).

8.   Haynes, C. L. & Van Duyne, R. P. "Nanosphere Lithography: A Versatile Nanofabrication Tool for Studies of Size-Dependent Nanoparticle Optics". *J. Phys. Chem. B* **105**, 5599–5611 (2001).

9.   Halas, N. J., Lal, S., Chang, W.-S., Link, S. & Nordlander, P. "Plasmons in Strongly Coupled Metallic Nanostructures". *Chem. Rev.* **111**, 3913–3961 (2011).

10.   Jensen, T. & Malinsky, M. "Nanosphere Lithography: Tunable Localized Surface Plasmon Resonance Spectra of Silver Nanoparticles". *J. Phys. Chem. B* **104**, 10549–10556 (2000).

11.   Ghosh, S. K. & Pal, T. "Interparticle Coupling Effect on the Surface Plasmon Resonance of Gold Nanoparticles: From Theory to Applications". *Chem. Rev.* **107**, 4797–4862 (2007).

12.   Stewart, M. E. *et al.* "Nanostructured Plasmonic Sensors". *Chem. Rev.* **108**, 494–521 (2008).

13.   Park, S. Y. *et al.* "DNA-Programmable Nanoparticle Crystallization". *Nature* **451**, 553–556 (2008).

14.   Nykypanchuk, D., Maye, M. M., Van der Lelie, D. & Gang, O. "DNA-Guided Crystallization of Colloidal Nanoparticles". *Nature* **451**, 549–552 (2008).

15.   Loweth, C. J., Caldwell, W. B., Peng, X. G., Alivisatos, A. P. & Schultz, P. G. "DNA-Based Assembly of Gold Nanocrystals". *Angew. Chem. Int. Ed.* **38**, 1808–1812 (1999).

16. Bidault, S., García de Abajo, F. J. & Polman, A. "Plasmon-Based Nanolenses Assembled on a Well-Defined DNA Template". *J. Am. Chem. Soc.* **130**, 2750–2751 (2008).

17. Tan, S. J., Campolongo, M. J., Luo, D. & Cheng, W. "Building Plasmonic Nanostructures with DNA". *Nat. Nanotech.* **6**, 268–276 (2011).

18. Shenhar, R. & Rotello, V. M. "Nanoparticles: Scaffolds and Building Blocks". *Acc. Chem. Res.* **36**, 549–561 (2003).

19. Katz, E. & Willner, I. "Integrated Nanoparticle-Biomolecule Hybrid Systems: Synthesis, Properties, and Applications". *Angew. Chem. Int. Ed.* **43**, 6042–6108 (2004).

20. Tikhomirov, G. *et al.* "DNA-Based Programming of Quantum Dot Valency, Self-Assembly and Luminescence". *Nat. Nanotech.* **6**, 485–490 (2011).

21. Aldaye, F. A., Palmer, A. L. & Sleiman, H. F. "Assembling Materials with DNA as the Guide". *Science* **321**, 1795–1799 (2008).

22. Kaur, P. *et al.* "Three-Dimensional Directed Self-Assembly of Peptide Nanowires into Micrometer-Sized Crystalline Cubes with Nanoparticle Joints". *Angew. Chem. Int. Ed.* **49**, 8375–8378 (2010).

23. Niemeyer, C. M. "Nanoparticles, Proteins, and Nucleic Acids: Biotechnology Meets Materials Science". *Angew. Chem. Int. Ed.* **40**, 4128–4158 (2001).

24. Mirkin, C. A., Letsinger, R. L., Mucic, R. C. & Storhoff, J. J. "A DNA-Based Method for Rationally Assembling Nanoparticles into Macroscopic Materials". *Nature* **382**, 607–609 (1996).

25. Alivisatos, A. P. *et al.* "Organization of `Nanocrystal Molecules' Using DNA". *Nature* **382**, 609–611 (1996).

26. Iacopino, D., Ongaro, A., Nagle, L., Eritja, R. & Fitzmaurice, D. "Imaging the DNA and Nanoparticle Components of a Self-Assembled Nanoscale Architecture". *Nanotechnology* **14**, 447–452 (2003).

27. Jones, M. R., Osberg, K. D., Macfarlane, R. J., Langille, M. R. & Mirkin, C. A. "Templated Techniques for the Synthesis and Assembly of Plasmonic Nanostructures". *Chem. Rev.* **111**, 3736–827 (2011).

28. Brown, S. "Protein-Mediated Particle Assembly". *Nano Lett.* **1**, 391–394 (2001).

29. Shipway, A. N., Katz, E. & Willner, I. "Nanoparticle Arrays on Surfaces for Electronic, Optical, and Sensor Applications". *Chem. Phys. Chem.* **1**, 18–52 (2000).

30. Berti, L. & Burley, G. A. "Nucleic aAid and Nucleotide-Mediated Synthesis of Inorganic Nanoparticles". *Nat. Nanotech.* **3**, 81–87 (2008).

31. Ma, N., Sargent, E. H. & Kelley, S. O. "Biotemplated Nanostructures: Directed Assembly of Electronic and Optical Materials Using Nanoscale Complementarity". *J. Mater. Chem.* **18**, 954–964 (2008).

32. Kumar, A., Ramakrishnan, V., Gonnade, R., Ganesh, K. N. & Sastry, M. "Electrostatically Entrapped DNA Molecules in Lipid Thin Films as Templates for the in situ Growth of Silver Nanoparticles". *Thin Films* **13**, 597–600 (2002).

33. Braun, E., Eichen, Y., Sivan, U. & Ben-Yoseph, G. "DNA-Templated Assembly and Electrode Attachment of a Conducting Silver Wire". *Nature* **391**, 775–778 (1998).

34. Burley, G. A. *et al.* "Directed DNA Metallization". *J. Am. Chem. Soc.* **128**, 1398–1399 (2006).

35. Fischler, M. *et al.* "Chain-Like Assembly of Gold Nanoparticles on Artificial DNA Templates via `Click Chemistry`". *Chem. Comm.* 169–171 (2008).

36. Cui, S., Liu, Y., Yang, Z. & Wei, X. "Construction of Silver Nanowires on DNA Template by an Electrochemical Technique". *Materials & Design* **28**, 722–725 (2007).

37. Kundu, S., Maheshwar, V. & Saraf, R. F. "Photolytic Metallization of Au Nanoclusters and Electrically Conducting Micrometer Long Nanostructures on a DNA Scaffold". *Langmuir* **24**, 551–555 (2008).

38. Richter, J. "Metallization of DNA". *Physica E* **16**, 157–173 (2003).

39. Niemeyer, C. M. "Nanotechnology. Tools for the Biomolecular Engineer". *Science* **297**, 62–63 (2002).

40. Mertig, M., Ciacchi, L., Seidel, R. & Pompe, W. "DNA as a Selective Metallization Template". *Nano Lett.* **2**, 847–844 (2002).

41. Deng, Z. & Mao, C. "DNA-Templated Fabrication of 1D Parallel and 2D Crossed Metallic Nanowire Arrays". *Nano Lett.* **3**, 1545–1548 (2003).

42. Gu, Q. *et al.* "DNA Nanowire Fabrication". *Nanotechnology* **17**, R14–R25 (2006).

43. Monson, C. F. & Woolley, A. T. "DNA-Templated Construction of Copper Nanowires". *Nano Lett.* **3**, 359–363 (2003).

44. Seidel, R., Mertig, M. & Pompe, W. "Scanning Force Microscopy of DNA Metallization". *Surf. Interface Anal.* **33**, 151–154 (2002).

45. Aubry, A. *et al.* "Plasmonic Light-Harvesting Devices Over the Whole Visible Spectrum". *Nano Lett.* **10**, 2574–2579 (2010).

46. Yan, H., Park, S. H., Finkelstein, G., Reif, J. H. & LaBean, T. H. "DNA-Templated Self-Assembly of Protein Arrays and Highly Conductive Nanowires". *Science* **301**, 1882–1884 (2003).

47. Richter, J., Mertig, M., Pompe, W., Mönch, I. & Schackert, H. K. "Construction ofHighly Conductive Nanowires on a DNA Template". *Appl. Phys. Lett.* **78**, 536–538 (2001).

48. Keren, K. *et al.* "Sequence-Specific Molecular Lithography on Single DNA Molecules". *Science* **297**, 72–75 (2002).

49. Chhabra, R. *et al.* "Distance-Dependent Interactions between Gold Nanoparticles and Fluorescent Molecules with DNA as Tunable Spacers". *Nanotechnology* **20**, 485201–485210 (2009).

50. Love, J. C., Estroff, L. A., Kriebel, J. K., Nuzzo, R. G. & Whitesides, G. M. "Self-Assembled Monolayers of Thiolates on Metals as a Form of Nanotechnology". *Chem. Rev.* **105**, 1103 – 1169 (2005).

51. Wirges, C. T. *et al.* "Controlled Nucleation of DNA Metallization". *Angew. Chem. Int. Ed.* **48**, 219–223 (2009).

52. Berti, L., Alessandrini, A. & Facci, P. "DNA-Templated Photoinduced Silver Deposition". *J. Am. Chem. Soc.* **127**, 11216–11217 (2005).

53. Yonezawa, Y., Sato, T., Ohno, M. & Hada, H. "Photochemical Formation of Colloidal Metals". *J. Chem. Soc. Faraday Trans. I.* **83**, 1559–1567 (1987).

54. Sato, T., Kuroda, S., Takami, A. & Yonezawa, Y. "Photochemical Formation of Silver-Gold (Ag-Au) Composite Colloids in Solutions Containing Sodium Alginate". *Appl. Organomet. Chem.* **5**, 261–268 (1991).

55. Pal, A. & Pal, T. "Silver Nanoparticle Aggregate Formation by a Photochemical Method and Its Application to SERS Analysis". *J. Raman Spectrosc.* **30**, 199–204 (1999).

56. Eustis, S. *et al.* "Growth and Fragmentation of Silver Nanoparticles in Their Synthesis with a fs Laser and CW Light by Photo-Sensitization with Benzophenone". *Photochem. Photobiol. Sci.* **4**, 154–159 (2005).

57. Abid, J. P., Wark, A. W., Brevetb, P. F. & Giraulta, H. H. "Preparation of Silver Nanoparticles in Solution from a Silver Salt by Laser Irradiation". *Chem. Comm.* **7**, 792–793 (2002).

58. Sudeep, P. K. & Kamat, P. V "Photosensitized Growth of Silver Nanoparticles under Visible Light Irradiation: a Mechanistic Investigation". *Chem. Mater.* **22**, 5404–5410 (2005).

59. Hammond, D. M. *et al.* "DNA Photography: An Ultrasensitive DNA-Detection Method Based on Photographic Techniques". *Angew. Chem. Int. Ed.* **46**, 4184–4187 (2007).

60. Tani, T. *Photographic sensitivity: theory and mechanisms*. (Oxford University Press: New York: 1995).

61. Eisele, D. M. *et al.* "Photoinitiated Growth of Sub-7 nm Silver Nanowires within a Chemically Active Organic Nanotubular Template". *J. Am. Chem. Soc.* **132**, 2104–2105 (2010).

62. Singh, Y., Murat, P. & Defrancq, E. "Recent Developments in Oligonucleotide Conjugation". *Chem. Soc. Rev.* **39**, 2054–2070 (2010).

63. Sharma, J. *et al.* "Toward Reliable Gold Nanoparticle Patterning on Self-Assembled DNA Nanoscaffold". *J. Am. Chem. Soc.* **130**, 7820–7821 (2008).

64. Lee, J.-S., Lytton-Jean, A. K. R., Hurst, S. J. & Mirkin, C. A. "Silver Nanoparticle-Oligonucleotide Conjugates Based on DNA with Triple Cyclic Disulfide Moieties". *Nano Lett.* **7**, 2112–2115 (2007).

65. Day, B. S. *et al.* "Thiolated Dendrimers as Multi-Point Binding Headgroups for DNA Immobilization on Gold". *Langmuir* **27**, 12434–12442 (2011).

66. Claridge, S. A. *et al.* "Directed Assembly of Discrete Gold Nanoparticle Groupings Using Branched DNA Scaffolds". *Chem. Mater.* **17**, 1628–1635 (2005).

67. Sönnichsen, C., Reinhard, B. M., Liphardt, J. & Alivisatos, A. P. "A Molecular Ruler Based on Plasmon Coupling of Single Gold and Silver Nanoparticles". *Nat. Biotechnol.* **23**, 741–745 (2005).

68. Dubois, L. & Nuzzo, R. G. "Synthesis, Structure, and Properties of Model Organic Surfaces". *Annu. Rev. Phys. Chem.* **43**, 437–463 (1992).

69. Zanchet, D., Micheel, C. M., Parak, W. J., Gerion, D. & Alivisatos, A. P. "Electrophoretic Isolation of Discrete Au Nanocrystal/DNA Conjugates". *Nano Lett.* **1**, 32–35 (2001).

70. Jhaveri, S., Foos, E. & Lowy, D. "Isolation and Characterization of Trioxyethylene-Encapsulated Gold Nanoclusters Functionalized with a Single DNA Strand". *Nano Lett.* **4**, 737–740 (2004).

71. Zanchet, D. *et al.* "Electrophoretic and Structural Studies of DNA-Directed Au Nanoparticle Groupings". *J. Phys. Chem. B* **106**, 11758–11763 (2002).

72. Claridge, S. A., Liang, H. W., Basu, S. R., Frechet, J. M. J. & Alivisatos, A. P. "Isolation of Discrete Nanoparticle - DNA Conjugates for Plasmonic Applications". *Nano Lett.* **8**, 1202–1206 (2008).

73. Sharma, J. *et al.* "Control of Self-Assembly of DNA Tubules through Integration of Gold Nanoparticles". *Science* **323**, 112–116 (2009).

74. Park, S.-J., Lazarides, A. A., Mirkin, C. A. & Letsinger, R. L. "Directed Assembly of Periodic Materials from Protein and Oligonucleotide-Modified Nanoparticle Building Blocks". *Angew. Chem. Int. Ed.* **40**, 2909–2912 (2001).

75. Cobbe, S. *et al.* "DNA-Controlled Assembly of Protein-Modified Gold Nanocrystals". *J. Phys. Chem. B* **107**, 470–477 (2003).

76. Lapiene, V., Kukolka, F., Kiko, K., Arndt, A. & Niemeyer, C. M. "Conjugation of Fluorescent Proteins with DNA Oligonucleotides". *Bioconjugate Chem.* **21**, 921–927 (2010).

77. Niemeyer, C. M., Ceyhan, B. & Hazarika, P. "Oligofunctional DNA-Gold Nanoparticle Conjugates". *Angew. Chem. Int. Ed.* **42**, 5766–5770 (2003).

78. Li, H., Park, S. H., Reif, J. H., LaBean, T. H. & Yan, H. "DNA-Templated Self-Assembly of Protein and Nanoparticle Linear Arrays". *J. Am. Chem. Soc.* **126**, 418–419 (2004).

79. Weber, P. C., Ohlendorf, D. H., Wendoloski, J. J. & Salemme, F. R. "Structural Origins of High-Affinity Biotin Binding to Streptavidin". *Science* **243**, 85–88 (1989).

80. Hendrickson, W. A. *et al.* "Crystal Structure of Core Streptavidin Determined from Multiwavelength Anomalous Diffraction of Synchrotron Radiation". *Proc. Nat. Soc. Am.* **86**, 2190–2194 (1989).

81. Hendrickson, W. A. "Determination of Macromolecular Structures from Anomalous Diffraction of Synchrotron Radiation". *Science* **254**, 51–58 (1991).

82. Florin, E.-L., Moy, V. T. & Gaub, H. E. "Adhesion Forces Between Individual Ligand-Receptor Pairs". **264**, 415–417 (1994).

83. Grubmüller, H., Heymann, B. & Tavan, P. "Ligand Binding: Molecular Mechanics Calculation of the Streptavidin-Biotin Rupture Force". *Science* **271**, 997–999 (1996).

84. Wong, J., Chilkoti, A. & Moy, V. T. "Direct Force Measurements of the Streptavidin-Biotin Interaction". *Biomolecular Engineering* **16**, 45–55 (1999).

85.   Ando, T. "High-Speed Atomic Force Microscopy Coming of Age". *Nanotechnology* **23**, 062001 (2012).

86.   Niemeyer, C. M., Adler, M., Gao, S. & Chi, L. "Nanostructured DNA-Protein Aggregates Consisting of Covalent Oligonucleotide-Streptavidin Conjugates". *Bioconjugate Chem.* **12**, 364–371 (2001).

87.   Stanca, S. E., Eritja, R. & Fitzmaurice, D. "DNA-Templated Assembly of Nanoscale Architectures for Next-Generation Electronic Devices". *Faraday Discus.* **131**, 155–165 (2006).

88.   Stanca, S. E., Ongaro, A., Eritja, R. & Fitzmaurice, D. "DNA-Templated Assembly of Nanoscale Architectures". *Nanotechnology* **16**, 1905–1911 (2005).

89.   Connolly, S. & Fitzmaurice, D. "Programmed Assembly of Gold Nanocrystals in Aqueous Solution". *Adv. Mater.* **11**, 1202–1205 (1999).

90.   Aslan, K., Luhrs, C. C. & Perez-Luna, V. H. "Controlled and Reversible Aggregation of Biotinylated Gold Nanoparticles with Streptavidin". *J. Phys. Chem. B* **108**, 15631–15639 (2004).

91.   Li, M., Wong, K. K. W. & Mann, S. "Organization of Inorganic Nanoparticles Using Biotin-Streptavidin Connectors". *Chem. Mater.* **11**, 23–26 (1999).

92.   Gole, A. & Murphy, C. J. "Biotin-Streptavidin-Induced Aggregation of Gold Nanorods: Tuning Rod-Rod Orientation". *Langmuir* **21**, 10756–10762 (2005).

93.   Caswell, K. K., Wilson, J. N., Bunz, U. H. F. & Murphy, C. J. "Preferential End-to-End Assembly of Gold Nanorods by Biotin-Streptavidin Connectors". *J. Am. Chem. Soc.* **125**, 13914–13915 (2003).

94.   Ishii, T., Otsuka, H., Kataoka, K. & Nagasaki, Y. "Preparation of Functionally Pegylated Gold Nanoparticles with Narrow Distribution through Autoreduction of

Auric Cation by alpha-biotinyl-PEG-block-[poly(2- (N,N-dimethylamino)ethyl methacrylate)]". *Langmuir* **20**, 561–564 (2004).

95. Li, M. & Mann, S. "DNA-Directed Assembly of Multifunctional Nanoparticle Networks Using Metallic and Bioinorganic Building Blocks". *J. Mater. Chem.* **14**, 2260–2263 (2004).

96. Mann, S., Shenton, W., Li, M., Connolly, S. & Fitzmaurice, D. "Biologically Programmed Nanoparticle Assembly". *Adv. Mater.* **12**, 147–150 (2000).

97. Kohut, A., Voronov, A. & Peukert, W. "Organization of Functionalized Gold Nanoparticles by Controlled Protein Interactions". *Part. Part. Syst. Charact.* **22**, 329–335 (2005).

98. Costanzo, P. J., Patten, T. E. & Seery, T. A. P. "Protein-Ligand Mediated Aggregation of Nanoparticles: A Study of Synthesis and Assembly Mechanism". *Chem. Mater.* **16**, 1775–1785 (2004).

99. Sastry, M., Lala, N., Patil, V., Chavan, S. P. & Chittiboyina, A. G. "Optical Absorption Study of the Biotin-Avidin Interaction on Colloidal Silver and Gold Particles". *Langmuir* **14**, 4138–4142 (1998).

100. Lala, N., Chittiboyina, A. G., Chavan, S. P. & Sastry, M. "Biotinylation of Colloidal Gold Particles Using Interdigitated Bilayers: a UV–visible Spectroscopy and TEM Study of the Biotin-Avidin Molecular Recognition Process". *Colloids and Surfaces A* **205**, 15–20 (2002).

101. Saleh, S. M., Ali, R., Hirsch, T. & Wolfbeis, O. S. "Detection of Biotin–Avidin Affinity Binding by Exploiting a Self-Referenced System Composed of Upconverting Luminescent Nanoparticles and Gold Nanoparticles". *J. Nanopart. Res.* **13**, 4603–4611 (2011).

102. Oh, E. *et al.* "Inhibition Assay of Biomolecules Based on Fluorescence Resonance Energy Transfer (FRET) between Quantum Dots and Gold Nanoparticles". *J. Am. Chem. Soc.* **127**, 3270–3271 (2005).

103. Connolly, S., Cobbe, S. & Fitzmaurice, D. "Effects of Ligand−Receptor Geometry and Stoichiometry on Protein-Induced Aggregation of Biotin-Modified Colloidal Gold". *J. Phys. Chem. B* **105**, 2222–2226 (2001).

104. Connolly, S., Rao, S. N. & Fitzmaurice, D. "Characterization of Protein Aggregated Gold Nanocrystals: *J. Phys. Chem. B* **104**, 4765–4776 (2000).

105. Chen, G. *et al.* "High-Purity Separation of Gold Nanoparticle Dimers and Trimers". *J. Am. Chem. Soc.* **131**, 4218–4219 (2009).

106. Sun, X. *et al.* "Separation of Nanoparticles in a Density Gradient: FeCo@C and Gold Nanocrystals". *Angew. Chem. Int. Ed.* **48**, 939–942 (2009).

107. Novak, J. P., Nickerson, C., Franzen, S. & Feldheim, D. L. "Purification of Molecularly Bridged Metal Nanoparticle Arrays by Centrifugation and Size Exclusion Chromatography". *Anal. Chem.* **73**, 5758–5761 (2001).

108. Wilcoxon, J. P., Martin, J. E., Parsapour, F., Wiedenman, B. & Kelley, D. F. "Photoluminescence from Nanosize Gold Clusters". *J. Chem. Phys.* **108**, 9137–9143 (1998).

109. Zon, V. B., Sachsenhasuer, M. & Rant, U. "Conjugation and Separation of Gold Nanoparticles with DTPA-Modified DNA". *in Preparation* (2013).

110. Zon, V. B., Sachsenhasuer, M. & Rant, U. "Preparation of Nanoparticle-Dimers via Streptavidin-Induced Interlinking". *in Preparation* (2013).

111. Sachsenhasuer, M., Zon, V. B. & Rant, U. "Preparation of Nanoparticle Conjugates with DNA and Protein Linkers". *International Symposium on DNA / Based MicroNano / Integration* (2010).

112. Zon, V. B., Sachsenhasuer, M. & Rant, U. "Formation of Nanoparticle Structures with a Combination of Protein and DNA Linkers". *International Symposium on Advances in Nanoscience* (2010).

113. Zon, V. B., Sachsenhasuer, M. & Rant, U. "Formation of Nanoparticle Structures with a Combination of Protein and DNA Linkers". *Second International Conference on Multifunctional, Hybrid and Nanomaterials* (2011).

114. Zon, V. B., Sachsenhasuer, M. & Rant, U. "Optical Properties of Nanoparticle Structures with a Combination of Protein and DNA Linkers". *Summer School "Plasmonics, Functionalization and Biosensing"* (2011).

115. Zon, V. B., Burley, G. A. & Rant, U. "Photo-Induced Growth of DNA-Capped Silver Nanoparticles". *Nanotechnology* **23**, 115607 (2012).

116. Zon, V. B., Böttner, C. & Rant, U. "Directed Growth of Metallic Nanoparticles on DNA Templates". *International Symposium "Molecular Plasmonics"* (2009).

117. Zon, V. B., Abstreiter, G. & Rant, U. "Directed Growth of Metallic Nanoparticles on DNA Templates". *NIM / CeNS / SFB 486 Winter School 2009 on Nanosystems and Sensors* (2009).

118. Dahneke, B. E. *Measurement of Suspended Particles by Quasielastic Light Scattering*. 584 (John Wiley & Sons Inc.: New York, 1983).

119. Williams, D. B. & Carter, C. B. *Transmission Electron Microscopy: A Textbook for Materials Science, Part 1*. 760 (Springer Science + Business Media LLC: New York, 2009).

120. Snyder, L. R., Kirkland, J. J. & Dolan, J. W. *Introduction to Modern Liquid Chromatography*. 960 (John Wiley & Sons, Inc.: Hoboken, New Jersey, 2011).

121. Harris, D. C. *Quantitative Chemical Analysis*. 750 (W. H. Freeman and Company: New York, 2007).

122. Felinger, A. *Data Analysis and Signal Processing in Chromatography*. 414 (Elsevier: Amsterdam, 1998).

123. *Electromagnetic Surface Modes*. 776 (John Wiley & Sons Ltd.: Belfast, 1982).

124. Zayats, A. V., Smolyaninov, I. I. & Maradudin, A. A. "Nano-Optics of Surface Plasmon Polaritons". *Physics Reports* **408**, 131–314 (2005).

125. Mie, G. "Beiträge zur Optik trüber Medien, speziell kolloidaler Metallösungen". *Ann. d. Physik* **25**, 377–445 (1908).

126. Gérardy, J. & Ausloos, M. "Absorption Spectrum of Clusters of Spheres from the General Solution of Maxwell's Equations. II. Optical Properties of Aggregated Metal Spheres". *Phys. Rev. B* **25**, 4204–4229 (1982).

127. Quinten, M. Analyse der optischen Eigenschaften inhomogener Materie am Beispiel aggregierter, kolloidaler Edelmetall-Systeme. (1989).

128. Quinten, M. *Optical Properties of Nanoparticle Systems*. 488 (Wiley-VCH Verlag & Co. KGaA: Weinheim, 2011).

129. Prodan, E., Radloff, C., Halas, N. J. & Nordlander, P. "A Hybridization Model for the Plasmon Response of Complex Nanostructures". *Science* **302**, 419–422 (2003).

130. Prodan, E. & Nordlander, P. "Plasmon Hybridization in Spherical Nanoparticles". *J. Chem. Phys.* **120**, 5444–5454 (2004).

131. Shaw, D. J. *Introduction to Colloid and Surface Chemistry*. 306 (Butterworth-Heinemann: Oxford, 1992).

132. Jin, R. *et al.* "Controlling Anisotropic Nanoparticle Growth Through Plasmon Excitation". *Nature* **425**, 487–490 (2003).

133. Jin, R. *et al.* "Photoinduced Conversion of Silver Nanospheres to Nanoprisms". *Science* **294**, 1901–1903 (2001).

134. Zhang, J., Langille, M. R. & Mirkin, C. A. "Photomediated Synthesis of Silver Triangular Bipyramids and Prisms: the Effect of pH and BSPP". *J. Am. Chem. Soc.* **132**, 12502–12510 (2010).

135. Xue, C., Métraux, G. S., Millstone, J. E. & Mirkin, C. A. "Mechanistic Study of Photomediated Triangular Silver Nanoprism Growth". *J. Am. Chem. Soc.* **130**, 8337–8344 (2008).

136. Zhang, J., Langille, M. R. & Mirkin, C. A. "Synthesis of Silver Nanorods by Low Energy Excitation of Spherical Plasmonic Seeds". *Nano Lett.* **11**, 2495–2498 (2011).

137. Maillard, M., Huang, P. & Brus, L. "Silver Nanodisk Growth by Surface Plasmon Enhanced Photoreduction of Adsorbed [Ag+]". *Nano Lett.* **3**, 1611–1615 (2003).

138. Efremova, N. V, Sheth, S. R. & Leckband, D. E. "Protein-Induced Changes in Poly(ethylene glycol) Brushes: Molecular Weight and Temperature Dependence". *Langmuir* **17**, 7628–7636 (2001).

139. Callegari, A., Tonti, D. & Chergui, M. "Photochemically Grown Silver Nanoparticles with Wavelength-Controlled Size and Shape". *Nano Lett.* **3**, 1565–1568 (2003).

140. Hiemenz, P. C. & Rjagopalan, R. *Principles of Colloid and Surface Chemistry*. 650 (Taylor & Francis Group: New York, 1997).

141. Neish, C. S., Martin, I. L., Henderson, R. M. & Edwardson, J. M. "Direct Visualization of Ligand-Protein Interactions Using Atomic Force Microscopy". *Br. J. Pharmacol.* **135**, 1943–1950 (2002).

142. Chapman, R. G. *et al.* "Surveying for Surfaces that Resist the Adsorption of Proteins". *J. Am. Chem. Soc.* **122**, 8303–8304 (2000).

143. Han, X. *et al.* "Manipulation and Charge Determination of Proteins in Photopatterned Solid Supported Bilayers". *Integr. Biol.* **1**, 205–211 (2009).

144.   García de la Torre, J., Lopez Martinez, M. C. & Mercedes Tirado, M. "Dimensions of Short, Rodlike Macromolecules from Translational and Rotational Diffusion Coefficients. Study of the Gramicidin Dimer". *Biopolymers* **23**, 611–615 (1984).

145.   Lee, P. C. & Meisel, D. "Adsorption and Surface-Enhanced Raman of Dyes on Silver and Gold Sols". *J. Phys. Chem.* **86**, 3391–3395 (1982).

146.   Henglein, A. & Giersig, M. "Formation of Colloidal Silver Nanoparticles: Capping Action of Citrate". *J. Phys. Chem. B* **103**, 9533–9539 (1999).

147.   Ahern, A. A. & Garrell, R. L. "In Situ Photoreduced Silver Nitrate as a Substrate for Surface-Enhanced Raman Spectroscopy". *Anal. Chem.* **59**, 2813–2816 (1987).

148.   Wu, X. *et al.* "Photovoltage Mechanism for Room Light Conversion of Citrate Stabilized Silver Nanocrystal Seeds to Large Nanoprisms". *J. Am. Chem. Soc.* **130**, 9500–9506 (2008).

149.   Métraux, G. S. & Mirkin, C. A. "Rapid Thermal Synthesis of Silver Nanoprisms with Chemically Tailorable Thickness". *Adv. Mater.* **17**, 412–415 (2005).

150.   Sauer, M., Hofkens, J. & Enderlein, J. *Handbook of Fluorescence Spectroscopy and Imaging: From Single Molecules to Ensembles*. 281 (Wiley: Weinheim, 2011).

151.   Sigel, A. & Sigel, H. *Interactions of Metal Ions with Nucleotides, Nucleic Acids, and Their Constituents*. 814 (Marcel Dekker: New York, 1996).

152.   Fayet, P. *et al.* "Latent-Image Generation by Deposition of Monodisperse Silver Clusters". *Phys. Rev. Lett.* **55**, 3002–3004 (1985).

153.   Shemer, G. *et al.* "Chirality of Silver Nanoparticles Synthesized on DNA". *J. Am. Chem. Soc.* **128**, 11006–11007 (2006).

154. Jensen, R. H. & Davidson, N. "Spectrophotometric, Potentiometric, and Density Gradient Ultracentrifugation Studies of the Binding of Silver Ion by DNA". *Biopolymers* **4**, 17–32 (1966).

155. Chang, R. K. & Furtak, T. E. *Surface Enhanced Raman Scattering*. (Plenum Press: New York, 1982).

156. Dong, X. *et al.* "Shape Control of Silver Nanoparticles by Stepwise Citrate Reduction". *J. Phys. Chem. C* **113**, 6573–6576 (2009).

10

List of My Publications

10.1 Peer-Reviewed Journal Publications

1. Zon, V. B., Sachsenhasuer, M. & Rant, U. "Conjugation and Separation of Gold Nanoparticles with DTPA-Modified DNA". *In Preparation* (2013).

2. Zon, V. B., Sachsenhasuer, M. & Rant, U. "Preparation of Gold Nanoparticle Dimers via Streptavidin-Induced Interlinking". *Submitted to the Journal of Nanoparticles Research* (2013).

3. Zon, V. B., Burley, G. A. & Rant, U. "Photo-Induced Growth of DNA Capped Silver Nanoparticles" *Nanotechnology* **23** 115607 (2012)

4. Zon, V. B. & Zon, B. A. "Relative Magnitude of Cross-Sections for Elastic and Inelastic Scattering of a Fast Particle on a Many-Particle Target" *Phys. Scr.* **86** 065303 (2012)

5. Zon, V. B., Zon, B. A., Klyuev, V. G., Latyshev, A. N., Minakov, D. A. & Ovchinnikov O. V. "Conversion of Surface Plasmon Polaritons into Photons: Visual Observation" *Phys. Usp*., **54** 291 (2011)

6. Zon, V. B. & Zon, B. A. "THz Surface Plasmon Polaritons on a Conductive Right Circular Cone: Analytical Description and Experimental Verification" *Phys. Rev. A*, **84** 013816 (2011)

7. Zon, V. B., Zon, B. A., Klyuev, V. G., Latyshev, A. N., Minakov, D. A. & Ovchinnikov, O. V. "New Method for Measuring the IR Surface Impedance of Metals" *Opt. Spectrosc*. **108** 637 (2010)

8. Latyshev, A. N., Minakov, D. A., Ovchinnikov, O. V., Buslov, V. A., Vikin, O. G., Zon, V. B. & Zon B. A. "Thermal Radiation of Two-Dimensional Bose-Einstein Gas of Surface Plasmons" *J. Opt. Soc, Am. B* **26** 397 (2009)

9. Zon, B. A. & Zon, V. B. "Logarithmically Accurate Total Integrated Cross Sections for Fast Electron Scattering on Atoms" *Tech. Phys.* **52** 35 (2007)

10. Zon, V. B. "Reflection, Refraction and Transformation into Photons of Surface Plasmons on a Metal Wedge" *J. Opt. Soc. Am. B* **24** 1960 (2007)

11. Zon, V. B. "Surface Plasmons on a Right Angle Metal Wedge" *J. Opt. A: Pure Appl. Opt.* **9** S476 (2007)

12. Minakov, D. A., Selivanov, V. N., Zon, V. B., Latyshev, A. N. & Ovchinnikov, O. V. "Thermal Radiation of Surface Waves in the Vicinity of a Copper Plate's Edge" *Condensed Media and Interphase Boundaries* **8** 131 (2006)

10.2 Conference Proceeding

1. Zon, V. B., Sachsenhasuer, M. & Rant, U. "Optical Properties of Nanoparticle Structures with a Combination of Protein and DNA Linkers". *Summer School "Plasmonics, Functionalization and Biosensing"*. Heidelberg, Germany (2011)

2. Zon, V. B., Sachsenhasuer, M. & Rant, U. "Formation of Nanoparticle Structures with a Combination of Protein and DNA Linkers". *Second International Conference on Multifunctional, Hybrid and Nanomaterials.* Strasbourg, France (2011)

3. Zon, V. B. & Zon, B.A. "Surface Plasmon Polaritons on a Cone". *NanoMeta 2011, Third European Meeting on Nanophotonics and Metamaterials.* Seefeld, Tirol, Austria (2011)

4. Zon V. B. (invited talk) "Plasmonics for Sensing Applications". *1st NRF CREATE Symposium on Nanomaterials for Energy and Water Management.* Singapore (2011)

5. Sachsenhasuer, M., Zon, V. B. & Rant, U. "Preparation of Nanoparticle Conjugates with DNA and Protein Linkers*". International Symposium on DNA / Based MicroNano / Integration.* Jena, Germany (2010)

6. Zon, V. B., Sachsenhasuer, M. & Rant, U. "Formation of Nanoparticle Structures with a Combination of Protein and DNA Linkers". *International Symposium on Advances in Nanoscience.* Garching b. Munich, Germany (2010)

7. Zon, V. B., Böttner, C. & Rant, U. "Directed Growth of Metallic Nanoparticles on DNA Templates". *International Symposium "Molecular Plasmonics"* Jena, Germany (2009)

8. Zon, V. B., Abstreiter, G. & Rant, U. "Directed Growth of Metallic Nanoparticles on DNA Templates". *NIM / CeNS / SFB 486 Winter School 2009 on Nanosystems and Sensors.* St. Christoph, Austria (2009)

9. Zon, V. B. "Reflection, Refraction and Transformation into Photons of Surface Plasmons on Metal Wedge". *Days on Diffraction-2007*, St. Petersburg, Russia (2007)

10. Zon, V. B. "Reflection, Refraction and Transformation into Photons of Surface Plasmons on Metal Wedge". *NanoMeta 2007. First European Meeting on Nanophotonics and Metamaterials.* Seefeld, Tirol, Austria (2007)

11. Latyshev, A. N., Minakov, D. A., Vikin, O. G., Ovchinnikov, O. V., Buslov V. A. & Zon, V. B. "Thermal Radiation of Surface Plasmons". *Third International Conference on Surface Plasmon Photonics.* Dijon, France (2007)

12. Zon, V. B. "Surface Plasmon Refraction, Reflection and Radiation at a Right-Angled Boundary". *Coherent Control of the Fundamental Processes in Optics and X-ray-Optics.* Nizhny Novgorod – Kazan – Nizhny Novgorod, Russia (2006)

13. Zon, V. B. "Reflection, Refraction and Transformation into Photons of Surface Plasmons on Metal Wedge". *13th International Conference on Solid Films and Surfaces.* San Carlos de Bariloche, Argentina (2006)

14. Zon, V. B. "Surface Plasmon Refraction, Reflection and Radiation at a Right Angled Boundary". *Photonics North 2006. International Conference on Application of Photonic technology.* Quebec, Canada (2006)

15. Zon B. A. & Zon V. B. "Logarithmically Accurate Total Integrated Cross Sections for Fast Electron Scattering on Atoms". *2nd International Conference on Current Development in Atomic, Molecular & Optical Physics with Applications.* Delhi, India (2006)

16. Zon B. A. & Zon V. B. "Logarithmically Accurate Total Integrated Cross Sections for Fast Electron Scattering on Atoms". *XXIV International Conference on Photonic, Electronic and Atomic Collisions.* Rosario, Argentina (2005)

11

Acknowledgements